Generation and Characterisation of PDX-derived Head and Neck Squamous Cell Carcinoma Tumour Organoids

---

Nicholas James Bodenstein

Auckland Cancer Society Research Centre

Faculty of Medical and Health Sciences, The University of Auckland

Auckland, New Zealand

Supervisors:

Associate Professor Stephen Jamieson

Dr. Wouter van Leeuwen

Dr. Tet-Woo Lee

A thesis submitted in partial fulfilment of the requirements for the degree of Master of Science (Pharmacology), The University of Auckland, 2022

Abstract

Purpose

Head and Neck Squamous Cell Carcinomas (HNSCC) are a class of malignant tumours that affect the squamous epithelial cells in the head and neck, and represent the 7th most-commonly occurring cancer type globally. As such, a need has arisen for the development of novel *in vitro* and *in vivo* models to determine the suitability of new potential therapies for treating HNSCC. This project aims to develop and characterise one such model: organoid models derived from patient-derived xenograft (PDX) tumours.

Experimental Design

Fourteen different PDX tumours for HNSCC were dissociated and seeded onto tissue culture plates to grow PDX-derived organoid models, with growth being monitored over a period of 1-2 months for each organoid line. The models that grew most successfully were harvested after short-term growth for histological analysis using haematoxylin and eosin (H+E), as well as characterisation for hypoxia using pimonidazole. The organoids were subjected to drug treatment, using a therapy that has been studied in the source PDX models: the hypoxia-activated prodrug evofosfamide, in order to assess the utility of the organoids for evaluating drug therapies In addition, RNA was extracted from these models in anticipation of downstream sequencing.

Results

Four organoid models were successfully established following short-term culture after two passages, allowing additional downstream characterisation experiments to be carried out. Histological analysis identified that the organoids recapitulate the squamous epithelial cell morphology present in the HNSCC PDX models, while pimonidazole staining did not show any presence of hypoxia in the organoids. When treated with evofosfamide, the organoids appear to reflect the variability in observed sensitivities that was reported in the matched PDX tumours. However, the extracted RNA was not of sufficient quality for RNA sequencing.

Conclusion

This thesis is the first published record of PDX-derived organoids being developed for HNSCC. These organoids appeared to recapitulate the histology and evofosfamide drug sensitivity of the source PDX tumours following short-term organoid cultures. However, further optimisation is required to ensure that these organoid models can be perpetuated over the longer term, as well as confirm that they recapitulate the genomic status of HNSCC tumours and therefore possess sufficient clinical utility for the testing of novel HNSCC therapies.

Acknowledgements

I would like to express my special thanks to Associate Professor Stephen Jamieson for the opportunity to undertake this research project, as well for the opportunity to contribute to and help further the aims of the wider Tumour Microenvironment Research Group. I would also like to thank him for the wraparound support he provided in the planning, development, and implementation of this project, as well as for the amazing amounts of help, feedback and suggestions that were crucial in being able to put this thesis together.

Special thanks also to Dr. Wouter van Leeuwen for the support and guidance he provided me in the lab. I appreciate the time he took to teach me the fundamentals of aseptic technique, organoid culture and cellular assays. As this was my first time carrying out a laboratory-based research project, all of these processes were a very steep learning curve for me. I will always remember Wouter’s mantra of ‘if you can grow organoids, you can grow anything!’ I wish him the very best for his endeavours back home in the Netherlands.

Thank you also to Dr. Tet-Woo Lee and Dr. Man Lu for your guidance regarding RNA extraction and cDNA library prep in preparation for RNA sequencing.

Many thanks to Dr. Satya Amirapu for working with me to develop and optimise the organoid staining protocols for this project. Your suggestions and feedback for sample processing were crucial in being able to obtain high-quality organoid images. Thank you also to Jacqueline Ross for teaching me about brightfield and fluorescent microscope imaging.

Finally, a massive thank you to everybody in the Auckland Cancer Society Research Centre for the welcoming atmosphere you have all created for people branching out into lab-based research for the first time. I will always be grateful for your patience in answering my seemingly endless questions, as well as for taking the time out of your busy schedules to show me how things work in the lab. I feel that I have learnt a lot in my time here, which was thanks in no small part to you all.

Table of Contents

List of Figures

List of Tables

1 Introduction

1.1 Head and Neck Squamous Cell Carcinoma

Head and Neck Squamous Cell Carcinoma (HNSCC) refers to a class of malignant tumours that originate in squamous epithelial cells of the head and neck. These squamous cells comprise part of the mucosal membranes that line the larynx, oropharynx, hypopharynx and oral cavity, and are relatively small and flat in shape (Klein & Grandis, 2010).

Broadly, HNSCC can be classified as one of two types, called HPV (Human Papillomavirus) positive – where the origin of the cancer can be traced to the patient being infected with HPV – and HPV-negative, which refers to cases which cannot be linked to HPV infection (Argiris et al., 2008). Each type has its own molecular and genomic causative pathways, along with different prognoses for treatment following diagnosis (Klein & Grandis, 2010). Almost half of all HNSCC patients are deemed to have an advanced stage of the disease at the time of diagnosis, with the expected 5-year survival rates below 50% (Guo et al., 2017). Most notably, patients with HPV-positive HNSCC appear to have better survival rates and responses to therapy compared to HPV-negative cases (Thomas & Shnayder, 2010). This literature review will explore the genetic mutational landscape of both types of HNSCC, their epidemiology, current therapies and the potential of hypoxia activated prodrugs (HAPs) as a possible treatment for these carcinomas. The use of patient-derived xenograft (PDX) and organoids derived from PDXs as preclinical models to test the efficacy of novel HAPs will also be discussed.

1.1.1 Epidemiology

HNSCC is diagnosed in over 550,000 people worldwide every year with more than 380,000 deaths from it annually (Fitzmaurice et al., 2017). Males have a greater likelihood of HNSCC diagnosis, with a ratio of 2:1 to 4:1 compared to females (McDermott & Bowles, 2019). In contrast to HPV-positive HNSCC, where the key risk factor is HPV infection, HPV-negative HNSCC has a greater variety of risk factors associated with it. These include alcohol consumption and cigarette smoking. Indeed, the frequency and length of time of cigarette use increases an individual's risk of HNSCC diagnosis (Blot et al., 1988; Hashibe et al., 2007), while alcohol consumption has been shown to almost double the risk of HNSCC independently of any other risk factors (Voltzke et al., 2018). Additional risk factors for HPV-negative disease include betel nut chewing, which is common in South Asia, and poor oral health (Voltzke et al., 2018). In the New Zealand context, it was observed that from the period of 1994-2018, age-standardised incidence rates remained low at below 1 per 100,000 people every year (Minhinnick et al., 2022). However, Pacific peoples, Asians and Maori all have a higher incidence of HNSCC relative to New Zealand Europeans, at 21, 17 and 4-fold higher respectively (Minhinnick et al., 2022).

1.1.2 Current Therapies and Patient Prognosis of HNSCC

Current therapies for HNSCC vary based on the stage of disease and ability to remove the tumour through surgery (Leemans et al., 2018). For example, tumour presentations that have been graded as Stage I or II on the TNM scale are usually treated with radiotherapy or surgery without additional chemotherapy (Marur & Forastiere, 2016). For tumours at a more severe TNM stage (III and IV) that have not metastasised, patients receive both radiotherapy treatment and a combination chemotherapy protocol typically comprising of 5-fluorouracil, cisplatin and carboplatin (Marur & Forastiere, 2016). This protocol is referred to as combined chemoradiotherapy (CCRT) and is sometimes followed up with adjuvant chemotherapy (Colevas et al., 2018; Karabajakian et al., 2019). Surgical removal of the tumour is carried out before CCRT where possible (Marur & Forastiere, 2016). An alternative option for tumours that can be surgically removed is the first-line use of 5-fluorouracil, cisplatin and docetaxel (induction chemotherapy), followed by treatment with CCRT (Colevas et al., 2018; Karabajakian et al., 2019). For tumours that cannot be surgically removed, the treatment options are more limited. CCRT remains the established therapy, although the utility of combining it with induction or adjuvant chemotherapy is still in doubt, as this combination does not appear to result in any significant increase in patient survival compared to using CCRT alone (Karabajakian et al., 2019). Interestingly, these therapies for HNSCC appear to be more efficacious in HPV-positive patients compared to HPV-negative patients, regardless of whether the tumours were surgically removed from the patients (Kimple & Harari, 2015; Ang et al., 2010).

More recently, molecularly targeted therapies have appeared as a possible alternative therapy, replacing platinum-based drugs in CCRT protocols (Mehra et al., 2018, Beckham et al., 2020). Cetuximab, a monoclonal antibody drug that binds irreversibly to EGFR, can replace platinum-based drugs in CCRT, and in some cases has been more efficacious (Tang et al., 2015). In addition, a combination chemotherapy protocol which involves the concomitant use of both cisplatin and cetuximab called 'EXTREME' has been developed and approved as an alternative first-line therapy (Goel et al., 2022; Lynggaard et al., 2014). Since then, two new immune checkpoint inhibitors, pembrolizumab and nivolumab, have been approved by the United States Food and Drug Administration (FDA) for the treatment of HNSCC. These immunotherapy agents act by binding to and inhibiting PD-1 receptors present on CD8$^+$ T-lymphocytes to prevent these cells from binding to PD-L1 receptors on the tumour cells, thereby reversing the ability of the tumour cells to evade immune processes (Goel et al., 2022; Saleh et al., 2018). Compared to the EXTREME protocol, immune checkpoint inhibitors have been found to increase progression-free survival in HNSCC patients (Harrington et al., 2020).

1.1.3 Genomic Landscape of HNSCC

A number of gene mutations have been identified as being potential drivers of HPV-negative HNSCC. Loss of function mutations in the tumour suppressor gene, *TP53,* have been found in over 80% of patients in genomic analyses of large numbers of HPV-negative HNSCC patients (Seiwert et al., 2015; The Cancer Genome Atlas Network, 2015). *TP53* codes for the p53 protein, which acts to prevent tumour formation through multiple different mechanisms, including the induction of apoptosis or suspension of the cell cycle at the G1/S restriction point in order to enable DNA repair. The loss of these regulatory mechanisms leads to excessive cell proliferation, which can serve to further drive tumour growth (Levine, 2019). In addition to *TP53, CDKN2A* is also a potential driver gene which is mutated in 21-25% of HPV-negative tumours (Seiwert et al., 2015; The Cancer Genome Atlas Network, 2015). In contrast to *TP53,* the most common type of *CDKN2A* mutation in HPV-negative tumours were nonsense mutations, with corresponding losses in *CDKN2A* gene function (Seiwert et al., 2015). Copy number loss of *CDKN2A* is also observed (The Cancer Genome Atlas Network, 2015). This gene codes for the protein p16, which acts as an inhibitor for the cyclin-dependent kinase 4 and 6 proteins (CDK4 and CDK6) (Hara et al., 1996). Without this inhibition, CDK4 and CDK6 bind to and phosphorylate retinoblastoma protein (RB), which in turn releases the E2F transcription factor that can then upregulate the transcription of genes which are needed to transition between the G1 and S phases of the cell cycle (Hara et al., 1996). If the transition between the G1 and S phase becomes dysregulated, tumour formation can occur (Lahin et al., 2019). Another common genomic abnormality in HNSCC tumours is that of *EGFR* amplification. This can lead to increased levels of EGFR protein synthesis, and therefore

EGFR-mediated downstream cell signalling via the PI3K-AKT cell signalling pathway (Davidson & Shanks, 2017). The resulting effect is the excessive phosphorylation of AKT, in turn resulting in excessive cell survival and proliferation, thereby driving tumour growth and survival (Davidson & Shanks, 2017; Jung et al., 2018). This abnormality in *EGFR* has not been associated with HPV-positive HNSCC (The Cancer Genome Atlas Network, 2015).

Interestingly, mutations of three oxidative stress genes (*NFE2L2*, *CUL3* and *KEAP1*) were identified in 22% of patients with HPV-negative HNSCC analysed by the Cancer Genome Atlas Network (2015), with mutations of these genes being identified in only 3% of HPV-positive patients. *NFE2L2* codes for a transcription factor protein called NRF2 (Nuclear factor erythroid 2-related factor 2), which binds to the gene promoter regions and upregulates the transcription of multiple antioxidant proteins when a cell is in oxidative stress (Itoh et al., 1999). When a cell is under normal physiological conditions, NRF2 is held in a ubiquitinated state by the CUL3 and KEAP1 proteins, in preparation for degradation in the proteasome (Itoh et al., 1999). In times of oxidative stress, CUL3 and KEAP1 dissociate from NRF2, allowing it to travel to the nucleus and upregulate antioxidant protein transcription (Kobayashi et al., 2004). These antioxidant proteins have a role in reducing the propagation of oxygen free radicals, which themselves are involved in the rapid increase in formation of reactive oxygen species (ROS) found in cells undergoing oxidative stress, which has been associated with both tumour growth and metastasis (Kobayashi et al., 2004). Other common genes for which mutations were identified in HPV-negative HNSCC include *MLL2*, *CCND1*, *MYC*, *NSD1*, *PIK3CA* and *NOTCH1* (Seiwert et al., 2015; The Cancer Genome Atlas Network, 2015).

HPV-positive HNSCC patients appear to possess a genetic mutational landscape which is distinct from that of HPV-negative HNSCC patients. The most commonly mutated gene in these patients is *PIK3CA*, which is mutated in 56% of HPV-positive HNSCC patients compared to just 34 % of HPV-negative patients (The Cancer Genome Atlas Network, 2015). This gene codes for the p110α catalytic subunit of phosphinositide-3-kinase (PI3K), whose physiological function is to convert PIP2 to PIP3 by phosphorylation as part of the aforementioned PI3K-AKT cell signalling pathway (Davidson & Shanks, 2017). Another common mutation in HPV-positive tumours is that of the *FGFR3* gene, (14% of HPV-positive HNSCC patients) (The Cancer Genome Atlas Network, 2015). *FGFR3* codes for the fibroblast growth factor receptor 3, which has important roles in cell proliferation, differentiation, angiogenesis, wound healing as well a regulatory effect on the ossification of cartilage to bone (Brands et al., 2017). Thus, when this protein becomes dysregulated, it can drive tumour angiogenesis and metastasis

(Brands et al., 2017). In contrast to HPV-negative tumours, mutations in *TP53* and *CDKN2A* are infrequent in HIV-positive tumours (The Cancer Genome Atlas Network, 2015).

1.1.4 Tumour Subtypes Associated with HPV-negative HNSCC

When specific gene mutations and copy number variations are taken together, it becomes possible to identify different subcategories of HPV-negative HNSCC. Two such subcategories have been identified; High-CNV (copy number variation) HPV-negative HNSCC and Low-CNV HPV-negative HNSCC (Leemans, et al., 2018; The Cancer Genome Atlas Network, 2015). High-CNV HPV-negative disease is characterised by frequent copy number variations (141 on average in The Cancer Genome Atlas Network, TCGA dataset), and mutations in *TP53* and *CDKN2A*, with cigarette smoking and alcohol consumption as the primary risk factors (Leemans et al., 2018; The Cancer Genome Atlas Network, 2015). Among patients with high-CNV HPV-negative HNSCC, three further tumour subtypes have been identified; basal, classical and mesenchymal (Job et al., 2019; Leemans et al., 2018; The Cancer Genome Atlas Network, 2015). These subtype classifications are based on what mutations a patient presents with alongside the CNVs they possess. Basal tumours have been defined as those with gene alterations driving dysregulation of the EGFR cell signalling pathway (Job et al., 2019). In contrast, classical tumours have a tendency towards mutations of the oxidative stress genes *NFE2L2*, *CUL3* and *KEAP1*, while mesenchymal tumours typically possess mutations in genes regulating epithelial-to-mesenchymal transition (The Cancer Genome Atlas Network, 2015).

Unlike high-CNV tumours, low-CNV tumours have not yet been identified as having multiple subtypes. These tumours can also be characterised by the presence of a wild-type *TP53* gene, with mutations in *HRAS* and *CASP8* as likely driver events (The Cancer Genome Atlas Network, 2015). The leading risk factors for this type of tumour are less clear, although it is thought that age may play a role in increasing patient risk (Leemans et al., 2018).

1.2 Tumour Hypoxia in HNSCC

Tumour hypoxia can be defined as a state of low oxygen partial pressure (pO_2) within tumour cells which in severe cases can be below 2.5 mmHg (Hoeckel & Vaupel, 2001; Muz et al., 2015). In contrast, oxygen partial pressure levels in healthy tissues commonly exceed 20 mmHg (McKeown, 2014). Tumour hypoxia first occurs when tumours grow to a large enough size (approximately 2 mm in diameter) that the normal vasculature alone is unable to supply the necessary oxygen and nutrients for tumour growth and cell survival (McDougall et al., 2006). In response to this, tumour cells can release tumour angiogenic factors (TAF) – such as Vascular Endothelial Growth Factor A (VEGF-A) – which interact with endothelial cells in blood vessels, driving their migration towards to the tumour site (Abhinand et al., 2016; Fu et al., 2011). Subsequently, these endothelial cells then sprout from the original blood vessel, forming new blood vessels. However, the blood vessels formed from the TAF activity are irregular in structure and are known to be leaky (Abhinand et al., 2016; Fu et al., 2011). Therefore, these new blood vessels are not sufficient for complete restoration of oxygen and nutrient supply to the rapidly proliferating tumour cells, and some of the tumour cells remain hypoxic, leading to further TAF release and angiogenesis (McDougall et al., 2006).

Tumour hypoxia can be classified as either acute, chronic or anaemic depending on aetiology. Acute hypoxia can be defined as hypoxia that has arisen due to failure of the dysfunctional blood vessels within the tumour to deliver sufficient oxygen to the tumour cells lying adjacent to them, with the state of hypoxia within the affected cells appearing to be more transient (O’Connor et al., 2016a). In contrast, chronic hypoxia is sustained over time, occurs in tumour cells located some distance from dysfunctional blood vessels (more than 70 μm), and arises due to insufficient diffusion of oxygen into these cells (Seddon et al., 2002; Stratford et al., 1988). Anaemic hypoxia occurs due to insufficient haemoglobin in the blood, reducing oxygen perfusion in tissues (Hoeckel & Vaupel, 2001). Hypoxia in tumour cells can lead to oxidative stress and subsequent necrosis within the tumour cells, with a common tumour morphology containing a necrotic and non-viable core (Williams et al., 2007). Surrounding the necrotic cells is a rim of viable hypoxic cells, with the outside of the tumour comprising well-oxygenated cells (O’Connor et al., 2012). As the tumour grows the necrotic core becomes larger, as the cells that were previously hypoxic are now further away from oxygen and so become necrotic, and some cells that were previously well oxygenated now become hypoxic (O’Connor et al., 2016a).

HNSCC patients with low observed pO_2 have poorer tumour-free and progression-free survival rates compared to those presenting with normoxic tumours, with HNSCC being the disease condition with the most evidence that hypoxia promotes a worse prognosis (Adam et al., 1999; Bhandari et al., 2019; Brizel et al., 1997; Nordsmark et al., 2005; Overgaard, 2011, Toustrup et al, 2012). A key mechanism of this is the induction of HIF-1α (Hypoxia inducible factor) during incidences of tumour hypoxia and oxidative stress (Carreau et al., 2015). Upregulation of HIF-α activity has been implicated in increased angiogenesis, cell survival and metabolism in HNSCC tumours (Muz et al., 2015; Zhang et al., 2013). Furthermore, angiogenesis plays a key role in cancer metastasis, as the provision of new blood vessels within the tumour allows tumours cells which have undergone epithelial-to-mesenchymal transition (EMT) to break off and spread to other parts of the body (Muz et al., 2015). Indeed, it has been reported in multiple studies that tumours with mild hypoxia are more likely to metastasise due to increased angiogenesis, driven by HIF-1α mediated activation of VEGF (vascular endothelial growth factor) (Bredell et al., 2016; Carmeliet et al., 1998, Kim et al., 2016).

1.2.1 The Role of Tumour Hypoxia in Driving HNSCC Therapeutic Resistance

Tumour hypoxia can also serve to undermine the existing CCRT treatment protocols. Radiotherapy acts through driving the formation of DNA free radicals that can then react with intracellular oxygen, thereby inducing permanent DNA strand breaks that are lethal for the affected cancer cell (Wang et al., 2019). Due to the lack of intracellular oxygen within hypoxic HNSCC tumour cells, the DNA radicals are instead reduced to their original form, thereby averting the generation of DNA strand breaks (Gray et al., 1953; Hoeckel & Vaupel, 2001, Muz et al., 2015). In addition, tumour hypoxia has been associated with elevated expression of heat shock proteins (HSP) in HNSCC tumours (Choi et al., 2015; van de Schootbrugge et al., 2014). Among other key functions, these HSPs have been identified as important for preventing DNA strand breaks, meaning their elevated expression in hypoxic cells hinders the ability of radiotherapy to elicit an anti-tumour effect (Guttman et al., 2013).

Hypoxia has also been shown to adversely impact the efficacy of chemotherapeutic agents to tumour cells. This could be due in part to the failure of these therapies to reach the intended HNSCC tumour cells, either through a lack of diffusion or through efflux proteins. Tumour hypoxia has been implicated in the upregulation of P-glycoprotein (P-gp), an efflux protein that can remove platinum-based therapies from the targeted HNSCC cells prior to eliciting an effect (Abraham et al., 2015; Muz et al., 2017; Song et al., 2016). Indeed, the use of P-gp inhibitors in addition alongside existing chemotherapeutic regimens can be used to overcome this resistance (Song et al., 2016). More specifically to platinum-based chemotherapies, a decrease in apoptotic potential in hypoxic cells, alongside cellular quiescence and acidosis have also been identified as driver of therapeutic resistance (Bedford & Mitchell, 1974; Das et al., 2008, Durand, 1994; Wike-Hooley et al., 1984).

Outside of CCRT protocols, hypoxia has also been implicated in the suppression of immune therapies. For example, in a syngeneic HNSCC tumour models with confirmed hypoxic regions, the binding of anti PD-1 monoclonal antibodies was suppressed (Zandberg et al., 2021). In addition, endogenous immune responses have also been found to be suppressed in hypoxic regions of HNSCC tumours, further undermining immune therapies (Bosco et al., 2006; Graham & Unger, 2018). Histological stains aimed to determine the extent of hypoxia and T-lymphocyte co-localisation has shown that these T-lymphocytes demonstrated reduced perfusion into the hypoxic region of HNSCC tumours (Brooks et al., 2019; Singleton et al., 2021). As a result, these T-lymphocytes are less able to mediate cytotoxic effects in hypoxic tumour regions (Brooks et al., 2019). Conversely, tumour hypoxia has also been associated with elevated perfusion of other immune cell types, such as macrophages and T-regulatory lymphocytes (T_{reg}) (Jayaprakash et al., 2018; Mahiddine et al., 2020; Noman et al., 2015, 2011). Indeed, macrophage recruitment has been associated with upregulation of tumour angiogenesis and cell proliferation, with these macrophages also adopting an M2 phenotype that further downregulates T-lymphocyte activity (Gomez et al., 2020). Additionally, T_{reg} cells also mediate an immunosuppressive effect, with the lactic acid present in hypoxic tumour cells undergoing acidosis being used as a metabolic fuel to drive this process (Watson et al., 2021). Finally, activation of HIF has been associated with increased expression of PD-L1, further contributing to hypoxia-mediated immune evasion within tumour cells (Watson et al., 2021).

1.2.2 Methods of Detection of Tumour Hypoxia in HNSCC Patients

Because tumour hypoxia has been shown to drive both HNSCC progression and therapeutic resistance, altering patient therapies based on tumour hypoxia status has the potential to pave the way for future personalised HNSCC therapeutic regimens through patient stratification (Spiegelberg et al., 2019). In order to implement patient stratification, however, hypoxia-specific biomarkers are needed to determine tumour hypoxia status. The ideal characteristics of a hypoxia biomarker would be that it is minimally invasive, elicit reproducible results when investigated frequently, can be used to specifically quantify the extent of hypoxia in tumour cells and is affordable (Dewhirst & Birer, 2016; McKeown, 2014). Several biomarker-based methods have been explored experimentally to evaluate tumour hypoxia in patients, with each possessing a unique combination of benefits and drawbacks.

An early approach to biomarker-based detection of tumour hypoxia was to use microsensor-based techniques. Such techniques include luminescence-based or polarographic oxygen sensors (Collingridge et al., 1997; Griffiths & Robinson., 1999; Hoeckel et al., 1991). However, this approach does possesses two key limitations. The first limitation is that these biosensors may not adequately elucidate which cells and cell types are hypoxic within the tumour, nor which cells are viable or necrotic (Harris et al., 2015; Hoeckel & Vaupel; 2001). The other limitation is that these techniques are highly invasive (Mirabello et al., 2018).

Nitroimidazoles have been used as a method to chemically identify regions of tumour hypoxia. Members of this class of compounds include nimorazole, misonidazole, etonidazole and pimonidazole (Chapman et al., 1981; Henk et al., 2003; Hodgkiss et al., 1997). These compounds readily diffuse into hypoxic tumour cells due to their low rates of metabolic degradation and high solubility (Stone et al., 1993). After this, they can act as an electrophile, driving the formation of a hydroxylamine intermediate which then facilitates the irreversible addition of the nitroimidazole to nucleophilic groups in DNA and proteins, forming adducts (Azuma et al., 1997; Henk et al., 2003; Jin et al., 2007; Kaanders et al., 2002; Kennedy et al., 1997; Nunn et al., 1995). In order to detect hypoxia, the adduct formation reaction can then be coupled with a detection method to identify regions of hypoxia within tumours. One example of such a detection method is positron emission tomography (PET). This has been rendered possible through the use of a subset of nitroimidazole compounds with an ^{18}F isotope in their chemical structures (^{18}F-fluoronitroimidazoles), which act as radiosensitisers upon adduct formation (Chitneni et al., 2011; Peerlings et al., 2017). With respect to HNSCC, ^{18}F-3-fluoro-2-(4-((2-nitro-1H-imidazol-1-yl)methyl)-1H-1,2,3-triazol-1-yl)propan-1-ol (HX4) has been used extensively to image tumour hypoxia, including successfully in clinical trials (Zegers et al., 2015a, 2015b, 2016), while other compounds such as, ^{18}F-fluoroazomycin arabinoside (FAZA) and ^{18}F-fluoromisoimidazole (FMISO) has been used to image tumour hypoxia with a view to predict the efficacy of CCRT protocols (Melsens et al., 2018; Peeters et al., 2015; Sanduleanu et al., 2020; Souvatzoglou et al., 2007). An alternative detection method for identifying regions of hypoxia in tumour samples is immunohistochemistry. Indeed, tumour models pre-treated with pimonidazole can subsequently be treated with an anti-pimonidazole antibody conjugated to a fluorophore and imaged under fluorescence microscopy, with the fluorescent regions correlating to regions of hypoxia within the tumour (Chitneni et al., 2011; Peerlings et al., 2017). This approach has been widely utilised with HNSCC tumour models to detect regions of hypoxia (Harms et al., 2019; Jamieson et al., 2018; Simoes-Sousa et al., 2016).

Magnetic resonance imaging (MRI) has been successfully utilised to non-invasively identify regions of tumour hypoxia through cross-sectional imaging (Mason et al., 1994, 2006; McCoy et al., 1996; Robinson et al., 1999). However, MRI can only be considered semi-quantitative, as the measurement parameters used in the cross-sectional imaging are not completely linked to tumour hypoxia (Favaro et al., 2011). One improvement on this technique that is currently being explored is oxygen-enhanced MRI, which can provide quantitation of tumour hypoxia through the imaging of oxygen concentrations in blood plasma and interstitial fluids surrounding the tumour (O'Connor et al., 2016b, 2019; Salem et al., 2019).

Finally, a novel approach of identifying a set of genes that are differentially expressed in hypoxic tumours has been developed and implemented for a range of different cancer types, including HNSCC. The first attempt to do this was carried out by Koong et al (2000), who identified 10 genes that could potentially act as biomarkers for tumour hypoxia. Subsequent developments on this research led to the identification of groups of genes, known as 'signatures' whose differential level of expression could be linked to hypoxia in tumour cells, as well as cells of the immune system and vasculature (Bosco et al., 2006; Jogi et al., 2004; Peters et al 2006). In order for these signatures to have any clinical relevance, the genes comprising each signature needed to be individually validated as being differentially expressed in hypoxic tumour cells. This was first achieved by Buffa et al (2010), who identified 15 genes that were differentially expressed in hypoxic tumours from a meta-analysis of multiple different cancer types. More specifically to HNSCC, two tumour hypoxia gene libraries have been developed and validated for HNSCC patients; a 15-gene library known as Toustrup HNSCC hypoxia gene library and a 26-gene library developed by Eustace et al. (Eustace et al., 2013; Toustrup et al., 2012, 2016). While there is variability in the genes included in the different hypoxia signatures, a meta-analysis of tumour hypoxia gene libraries carried out by Harris et al (2015) identified that several genes whose transcription is upregulated by HIF, such as *PGK1*, *BNIP3L*, *P4HA1*, *NDRG1* and *ADM*, are featured in multiple tumour hypoxia signatures. Finally, hypoxic gene signatures can be used to compare the extent of hypoxia between different tumour types. When hypoxia was quantitated across 27 different tumour types using a combination of three different gene signatures comprising over 50 genes (Buffa et al., 2010; Ragnum et al., 2015; Winter et al., 2007), HNSCC was found to be the second-most hypoxic tumour type surveyed, with only lung tumours appearing to be more hypoxic (Bhandari et al., 2019). However, as of present this method is largely limited to the research setting, with MRI-based techniques and nitroimidazole-based PET scans continuing to be the most widely-used hypoxia detection methods for HNSCC in the clinic (Hammond et al., 2014; Hill et al., 2022).

1.3 Hypoxia-activated Prodrugs in HNSCC Treatment

One group of therapies designed to selectively target hypoxic tumours are hypoxia-activated prodrugs (HAP) (Wilson & Hay, 2011). These can be defined as drugs which are administered as an inert prodrug, but which are converted to an active metabolite by one-electron reductases (O’Connor et al., 2016b). Under normoxic conditions, the drug can then be backconverted to its inert form, while under hypoxic conditions, this backconversion doesn’t take place, allowing the drug to subsequently cause a cytotoxic effect (O’Connor et al., 2016b). Theoretically, such drugs confer two key advantages over the present chemotherapy treatments and radiation. Firstly, the fact that these drugs are designed to elicit an effect only on hypoxic cells means that tumour cells could be targeted with a greater degree of specificity than with existing therapies, thereby leading to fewer off-target effects and superior patient tolerance (Mistry et al., 2017; O’Connor et al., 2016b). Secondly, the use of hypoxia-activated prodrugs could be combined with radiation to elicit synergistic anti-tumour effects, as the HAP could target tumour cells which are resistant to radiation therapy (Mistry et al., 2017). As such, numerous attempts have been made to develop HAPs. Earlier attempts, such as those using PR-104 and failed to result in approval due to not being sufficiently selective for hypoxic cells, with the involvement of an oxic two-electron reductase thought to cause dose-limiting toxicities in the case of PR-104 (Guise et al., 2010; Konopleva et al., 2015; Patterson et al., 2007). Evofosfamide, in contrast, while showing high levels of patient safety and tolerability (Borad et al., 2015; Chawla et al., 2014; Ganjoo et al., 2011; Jamieson et al., 2018; Weiss et al., 2011), failed at phase III in sarcoma and pancreatic cancer (Tap et al., 2017; Van Cutsem et al., 2016). However, it has been suggested that these earlier failures may have been due to a lack of patient stratification based on tumour hypoxia status (Jackson et al., 2019; Spiegelberg et al., 2019). Other HAPs that have also been investigated include tirapazamine, apaziquone and SN30000 (Li et al., 2021a; Spiegelberg et al., 2019)

1.4 Preclinical Models of Cancer

Preclinical models of cancer are defined as a range of non-human preparations that are designed to mimic some of the key aspects of primary human tumours. These can involve the use of *in vitro* cell lines or *in vivo* animal models, and are needed to evaluate the activity of novel anti-cancer therapies prior to these therapies progressing into clinical trials. Each of the models described in this section has key advantages and limitations, and as such, none should be used in isolation to characterise a novel therapy. This section will review the utility of each of these models for cancer research in general, as well as evaluate the current uses of PDX and organoid models in HNSCC research.

1.4.1 Immortalised Cell Lines

Immortalised cell lines are cell cultures original derived from a primary tumour, but due to the presence of mutations are able to avoid regular cell senescence processes, with these cells typically grown as 2D monolayer cell cultures (Kopf-Maier et al., 1992; Tinhofer et al., 2020). The key advantage of this model is that the cells can typically be easily grown and perpetuated, thereby facilitating their use in the investigatation of the potential anti-cancer efficacy of novel drug compounds (Bodnar et al., 2021). However, when these cell models are grown in 2D, they fail to recapitulate key characteristics of the primary tumours they intend to model, including histology, 3D arrangements and the tumour microenvironment (Kopf-Maier et al., 1992; Tinhofer et al., 2020). An alternative technique that can overcome these limitations is known as spheroids, which involves growing immortalised cell lines in a 3D cluster, thereby allowing the immortalised cell lines to more closely mimic *in vivo* tumour growth, as well as the tumour microenvironment (Fey & Wrzesinski., 2012). Indeed, this has resulted in differential observed sensitivities to the same drug when immortalised cell lines were grown as 2D monolayers compared to 3D spheroids, as well as upregulation of genes pertaining to epithelial-to-mesenchymal transition and DNA repair (Ayuso et al., 2019; Close & Johnston, 2022; Melissaridou et al., 2019). However, one key limitation affects 2D monolayer and 3D spheroid cultures of immortalised cell lines alike; clonal selection in culture can lead to genomic instability, which adversely affects the reproducibility of drug treatment experimental results. For example, when different clonal populations of A549 lung cancer and MCF7 breast cancer cell lines were screened against a panel of 321 potential therapeutic compounds, more than 75% of all compounds tested showed strong anti-cancer activity in some of the clones, while showing no effect in other clones (Ben-David et al., 2017). Thus, additional tumour models are needed that overcome the limitations present in immortalised cancer cell lines.

1.4.2 Syngeneic Mouse Models

Syngeneic tumour models can be defined as the implantation of murine cancer cells grown as immortalised cell lines into an immune-competent mouse (Smith & Thomas, 2006). Because these mice are immune-competent, this approach can be utilised to characterise the interactions between the engrafted tumour and the immune system in order to determine how these interactions can impact tumour growth (Mosely et al., 2017). Additionally, this approach provides an *in vivo* platform for the assessment of combination immunotherapies (Mosely et al., 2017; Nagaya et al., 2017). Furthermore, syngeneic mouse models have also been successfully utilised to model tumour hypoxia in a wide range of different cancer types, including HNSCC (Betof et al., 2015; Duarte et al., 2012; De Jaeger et al., 2001; Jenkins et al., 2000; Sonveaux et al., 2008; Zhang et al., 2002). However, one key limitation of syngeneic tumour models is that the cells engrafted into the mice are murine cancer cells, which do not reflect human biology and as such are not ideal to evaluate the potential utility of molecular targeted therapies for human cancers.

1.4.3 Genetically Engineered Mouse Models (GEMMs)

GEMMs refer to mice that have been genetically altered to induce overexpression or suppression of a target gene or group of genes, thereby leading to tumour formation in the mouse (Kersten et al., 2017). This approach has been utilised and validated to mimic tumorigenesis and growth in an immune-competent model system, in addition to mimicking the tumour microenvironment across multiple cancer types (Kersten et al., 2017; Prahallad et al., 2012; Platt et al., 2014; Premsrirut et al., 2011). Indeed, this approach has even been utilised in a co-clinical trial approach to predict potential therapeutic responses based on a patient's mutational profile in prostate and lung cancers (Chen et al., 2012; Clohessy & Pandolfi, 2015; Lunardi et al., 2013), as well as to rapidly generate on-site tumour models for HNSCC (Bornstein et al., 2009; Schreiber et al., 2004). However, this approach does possess two key limitations. Firstly, growth rates of tumours between individual mice can vary widely, with a potentially long latency time before tumours begin to emerge (Li & Shen., 2021; Mueller et al., 1997; Weidner et al., 2016). Additionally, these mouse models do not recapitulate the full genomic landscape present in humans as not all human genes have orthologs in mice, meaning that these models may not be suitable for all cancer types (Kersten et al., 2017).

1.4.4 Cell Line Xenografts (CLX)

Cell-line xenograft models are defined as the implantation of a previously-cultured immortalised cell line into an immune-compromised mouse (Okada et al., 2019; Zhao et al., 2011). A large number of such models have been developed for a wide range of different tumour types, including HNSCC (Bhadury et al., 2016; Okada et al., 2019; Zhao et al., 2011). This implantation can be either orthotopic (into the same place where the tissue of interest would reside in the body) or subcutaneous. CLX models can be utilised to characterise tumour responses to novel cancer therapies using an *in vivo* approach that potentially recapitulates the tumour microenvironment, including tumour hypoxia (Barati et al., 2018; Yu et al., 2018; Zhang et al., 2018). However, the extent to which these models recapitulate tumour hypoxia remains controversial. For example, Bhadury et al (2016) reported that the CLX models they generated for melanoma showed differential levels of expression of hypoxia response factors compared to other cell models such as patient-derived xenograft models. This may be due to one key limitation present in CLX models; due to the fact they are derived from immortalised cell lines, clonal selection is likely to have occurred in the immortalised cell lines they were derived from (Choi et al., 2014; Morgan, 2012; Sano & Myers, 2009). This has been shown to potentially undermine the utility of these models in predicting responses to chemotherapeutic agents, as contradictory results have been observed between primary tumour and the CLX models across multiple cancer types (Choi et al., 2014; Daniel et al., 2009; Sano & Myers, 2009; Supsavhad et al., 2016). Indeed, large numbers of antitumour therapies that were demonstrated to have anti-tumour efficacy using CLX models have failed to reproduce these effects in clinical trials (Johnson et al., 2001; Volpe et al., 1996; Voskoglou-Nomikos et al., 2003). Another limitation of this tumour model is that unlike GEMMs and syngeneic tumour models, interactions between the immune system and the tumour cannot be studied, as these tumours are implanted on immune compromised mice (Girotti et al., 2016; Izumchenko et al., 2017).

1.4.5 Patient-derived Xenografts (PDX)

Patient derived xenograft (PDX) models are defined as the direct implantation of a human tumour (collected during surgery) into an immune-deficient mouse without an intermediate culturing step (Harms et al., 2019; Ruicci et al., 2019). Like with CLX models, this implantation can be orthotopic or subcutaneous. As such, PDX models more closely preserve the cellular heterogeneity and tumour microenvironment of the primary tumour compared to CLX models and immortalised cell lines due to the lack of clonal selection in culture (Aparicio et al., 2015; Cassidy et al., 2015; Hidalgo et al., 2014). Furthermore, PDX models have been demonstrated to recapitulate the genomic profile of their source tumours, including mutations, single nucleotide polymorphisms and epigenetics (Ben-David et al., 2017; DeRose et al., 2011; Lin et al., 2014; Risbridger et al., 2015) As a result, PDX models are able to more successfully mimic genomic aberrations driving therapeutic resistance compared to immortalised cell lines and CLX models, and thus can more accurately model responses to novel compounds during drug development (Choi et al., 2014; Kreso et al., 2013). This faithful recapitulation of genomic aberration has also enabled PDX model to successfully be utilised to predict both positive and negative responses to clinical patients (Ben-David et al., 2017; Izumchenko et al., 2017). However, PDX models share one key limitation with CLX models; as they involve the engraftment of tumours onto immunocompromised mice, interactions between the immune system and the tumour cannot be studied (Forster & Devlin, 2018). However, this can be ameliorated in part by engrafting human bone marrow stem cells alongside the primary tumour (Eswaraka & Giddabasappa, 2017; Rongvaux et al., 2014).

1.4.5.1 PDX Models in HNSCC

PDX models of HNSCC appear to strongly recapitulate clinical HNSCC tumours (Harms et al., 2019; Kang et al., 2020; Karamboulas et al., 2018). Comparisons of histological slides have repeatedly shown strong similarities between HNSCC tumour samples resected from patients and PDX models (Kang et al., 2020; Karamboulas et al., 2018; Peng et al., 2013). Additionally, common genetic abnormalities in HNSCC patients, have been observed at similar rates in HNSCC PDX models (Folaron et al., 2019; Peng et al., 2013; Ruicci et al., 2019). Furthermore, while not all human HNSCC tumours undergo engraftment to the mouse host following implantation, those tumours that do engraft have been associated with worse clinical outcomes, including tumour re-emergence and reduced 5-year overall survival rates (Joshua et al., 2012; Karamboulas et al., 2018).

However, the ability of PDXs to consistently mimic the hypoxia observed in human HNSCC tumours is less clear. One method to measure the extent of hypoxia in tumour cells is to calculate what is known as a ‘hypoxic fraction,’ which can be defined as the proportion of the tumour that is hypoxic (Hammond et al., 2014). Indeed, there have been studies where hypoxic fractions observed in HNSCC PDX models were within the range commonly observed in patient tumours (Harms et al., 2019; Jamieson et al., 2018) while other research has shown an elevated hypoxic fraction in HNSCC PDX models compared to the primary tumours (Facompre et al., 2020; Stegeman et al., 2013). Further complicating matters is that a major determinant of tumour hypoxia is the ability of the vasculature within the tumour to provide sufficient oxygen to the tumour cells (Brown & Wilson, 2004). Thus, tumour hypoxia within the PDX is more likely to be mediated by the mouse host within which the PDX is contained, instead of being mediated by the PDX tumour itself (Lee et al., 2020). Nevertheless, there seems to be a high level of agreement between observed levels of hypoxia in primary tumours and PDX tumours in other cancers (Chaudhary et al., 2012; Ljungkvist et al., 2002; Lohse et al., 2016). Taken together, these findings suggest that it may be possible to consistently and reliably model tumour hypoxia using PDX models, however more research is required to ascertain this.

In previous work in our laboratory, evofosfamide has been shown to be active in reducing tumour size in PDX models of HNSCC (Harms et al., 2019; Jamieson et al., 2018). The extent of tumour size reduction varied wildly between the ten HNSCC PDX models studied, with one model showing complete regression following evofosfamide treatment (Harms et al., 2019; Jamieson et al., 2018). However, it was observed that evofosfamide sensitivity across these models was only weakly correlated with tumour hypoxia when quantified by pimonidazole staining (Harms et al., 2019). This suggests that tumour hypoxia may only play a small role in determining evofosfamide sensitivity, and that other as-yet-unidentified factors may influence evofosfamide sensitivity more directly (Harms et al., 2019; Hong et al., 2018 Jamieson et al., 2018).

1.4.6 Organoid Models in Cancer

Organoids can be defined as a simplified version of an organ, grown using 3D cell culture methods and whose cells contain similar microanatomy to the human organ of interest (Driehuis et al., 2019; Lee et al., 2020). This organoid tissue can be derived from primary tissue from a human patient, as well as induced pluripotent stem (iPS) cell, embryonic stems cells, as well as PDX models (Broutier et al., 2017; Cai et al., 2021; Raikwar et al., 2015; Varzideh et al., 2019). Organoid models present distinct advantages over other cell types when used to model disease. Firstly, there is substantial evidence that organoids can accurately recapitulate primary tumour morphology when histopathological comparisons are made between organoids and the primary tissue they were derived from, with these observations remaining true across multiple cancer types (Driehuis et al., 2019; Gao et al., 2014; Xie & Wu., 2016). Secondly, organoids have been shown to recapitulate gene expression profiles found in the primary tumours, with high levels of similarity in somatic mutations, copy number variations and the diversity of genes expressed (Sachs et al., 2018; Sachs & Clevers, 2014; Weeber et al., 2015). Finally, these tumour models have been successful in predicting patient responses to drug therapies, regardless of whether the response was positive or negative. For example, in a study carried out for ovarian cancer, organoid models showed tumour regression in 88% of cases where tumour regression also occurred in the patients (Vlachogiannis et al., 2018). In the same study, the organoid models also successfully predicted all cases where drug therapies showed a lack of efficacy (Vlachogiannis et al., 2018). Similar trends have also been observed in patient-derived organoid studies for other cancer types, including colorectal cancers, gastrointestinal metastases and glioblastoma (Jacob et al., 2020; Matsuzawa-Ishimoto et al., 2020; Ooft et al., 2019).

1.4.6.1 Organoid Models in HNSCC

Although patient-derived organoid models have only been recently established for HNSCC, these organoid models have been shown to recapitulate most aspects of primary HNSCC tumours in vitro (Driehuis et al., 2019; Tanaka et al., 2018; Wang et al., 2022).

The first available published record of an organoid model being developed and characterised for HNSCC was that carried out by Tanaka et al (2018). This approach utilised surgically resected patient-derived primary tumours as the source tissue, which were minced and trypsinised to form spheroid-like cell clusters approximately 40-100 µm in diameter. These clusters were initially seeded directly in their culture medium and monitored for growth and preservation of viability, prior to being transferred to an extracellular matrix medium (Matrigel) to stimulate 3D growth. Although only 16 of the 43 primary tumours (37.2%) seeded this way successfully established organoids, 13 of these organoids subsequently survived their first passage and were utilised in characterisation experiments, while only 3 survived beyond their second passage. Nevertheless, the organoids generated in this study did successfully recapitulate key aspects of the primary tumours they were derived from. For instance, histological stains carried out using haematoxylin and eosin (H+E) showed that these organoids successfully demonstrated the shape and arrangement of the epithelial cells present within the primary tumour. Additionally, the organoids also recreated the mutational profile of the TP53 gene present in their source tumours when this single gene was sequenced using a targeted single-gene RNA sequencing approach. Finally, when these organoids were treated with cisplatin and docetaxel as a monotherapy and subjected to viability assays, it was observed that the IC_{50} values for drug-mediated reductions in overall cell viability correlated strongly to the observed sensitivities of these drugs in the corresponding HNSCC patients. Thus, the organoid models appeared to recapitulate the inter-individual variability in tumour responses, thereby enhancing the potential utility of these models as a tool for predicting patient treatment responses.

Driehuis et al (2019) established HNSCC organoids using different methodology, where the organoids were minced and trypsinised to form a single cell suspension, before being immersed in extracellular matrix solution (Basement Membrane Extract) and seeded directly onto a culture plate. This approach appeared to improve the rate of successful organoid establishment compared to that reported by Tanaka et al (2018), with 26 out of 40 primary tumours successfully establishing organoids (65%). Furthermore, these organoid cultures were successfully perpetuated across 15 passages. Histological staining yielded similar results to those reported by Tanaka et al (2018), with the organoids successfully replicating the shape and arrangement of the epithelial tissues present in the primary tumours. Similar trends were also reported with respect to drug sensitivity; although direct correlations to patient tumour responses were not investigated directly in this study, the organoids showed differential responses to three different anticancer drugs; cisplatin, carboplatin, and cetuximab. Taken together with the earlier findings identified by Tanaka et al (2018), this provides preliminary evidence that patient-derived HNSCC organoids can predict patient responses to a wide range of therapies. Furthermore, Driehuis et al (2019) demonstrated that organoids treated with radiotherapy were shown to effectively mimic patient responses, including those where patients continued to develop progressive disease post-treatment. Finally, a combination of targeted and whole-exome sequencing across 16 HNSCC patient-derived organoids revealed that these HNSCC organoids also successfully capture the mutations and copy number variations in important tumorigenic genes such as *TP53, CDKN2A*, *EGFR* and *PIK3CA* that are observed in HNSCC primary tumours.

In addition to recapitulating tumour morphology, gene expression profiles and drug sensitivity of primary tumours, more recent resesrch has shown that HNSCC organoids can mimic systems to avoid immune surveillance. Wang et al (2022) have demonstrated in their patient-derived HNSCC organoid model by using a single-cell RNA sequencing technique that cancer stem cells within the HNSCC organoid show elevated levels of expression of the gene CD276. This gene codes for a transmembrane protein (CD276) that acts as an inhibitor of CD8+ T-lymphocytes, thereby enabling these cancer stems cells to evade CD8+ T-lymphocyte immune responses and proliferate (Lemke et al., 2012; Wang et al., 2022). Additionally, it was also demonstrated that monoclonal anti-CD276 antibodies that bind to and specifically inhibit CD276 can facilitate the infiltration of CD8+ T-lymphocytes into the organoid to induce apoptosis of the cancer stem cells by the release of granzyme B (Wang et al., 2022). These findings suggest that HNSCC organoids have the potential to also be used as predictive tools to modelling the efficacy of immunotherapies in treating HNSCC if co-cultured with immune cells.

1.4.6.2 PDX-Derived Organoids

More recently, PDX models have been utilised as a source tissue for the development of cancer organoid models. These models can be used to develop organoids as they have been derived from primary human tissue and those human tumour cells are retained in the PDX models (Driehuis et al., 2019). PDX-derived organoid models are thought to have one key advantage over organoids derived from primary tumours in that they have a faster growth rate in culture compared to organoid models derived from primary tumours. This is thought to be due to these models having previously undergone tumour initiation as a PDX, and enables the development of short-term culturing protocols (Cai et al., 2021; Huang et al., 2020; Takada et al., 2021). At the same time, PDX-derived organoids have also demonstrated that like their primary-tumour derived counterparts, they too successfully recapitulate both the tumour morphology, gene expression activity and responses to drug therapies (Cai et al., 2021; Huang et al., 2020; Takada et al., 2021). Taken together, these attributes mean that PDX-derived organoids have the potential to be utilised in the rapid development of personalised cancer therapies (Boj et al., 2015; Broutier et al., 2017; Gao et al., 2014; Takada et al., 2021). However, despite these advantages, there are few studies that have directly reported their rates of successful organoid establishment, although one study (Guillen et al., 2022) reported a success rate of 85%, which is generally higher than standard organoid protocols. Additionally, no published record exists of PDX-derived organoids being established for HNSCC.

1.4.7 Comparison of Organoid and PDX Models for HNSCC

Although both PDX models and organoids can faithfully recapitulate their source tumours, compared to PDX models, organoids appear to have some key advantages and disadvantages. Firstly, there are fewer ethical concerns with using organoid models as opposed to PDX models, meaning there is a greater flexibility on the types of experiments that can be carried out on these cells (Lee et al., 2020). Like PDX models, the potential exists for organoid models to be used as a means to predict the prognosis of HNSCC patients (Driehuis et al., 2019; Tanaka et al., 2018). The utility of organoid models for this purpose may be superior than PDX, due to the reduced time taken for organoids to develop compared to PDX models (Sachs et al., 2018; Lee et al., 2018). Additionally, organoids can be established from a smaller number of cells compared to PDX models (Yoshida, 2020). However, one key disadvantage of tumour organoids is that they lack the connective tissue, immune cells and blood vessels that are found in the primary tumours (Burtness et al., 2019; Driehuis et al., 2019). In comparison, PDX models in general do possess the blood vessels and connective tissue found in primary tumours, but do not possess the immune cells (Burtness et al., 2019).

1.5 HNSCC Organoid Culturing Protocols

There are significant overlaps between published culturing protocols for cancer tumour organoids, both within HNSCC and other cancer types. In general, these protocols utilise an advanced Dulbecco's Modified Eagle Medium (DMEM)-based culture medium (adDMEM/F12), supplemented with Wnt, epidermal growth factor (EGF), R-spondin and Noggin, (Driehuis et al., 2020; Huang et al., 2019; Shi et al., 2020; Tanaka et al., 2021). Wnt is utilised in these cultures to promote EMT within the organoid cells, while R-spondin is a growth factor that is utilised to further upregulate Wnt signalling (Urbischek et al., 2019). Noggin, in contrast, is used to inhibit bone morphogenic protein, thereby serving to inhibit the differentiation of stem cells contained within the organoids, while EGF promotes cell proliferation (Urbischek et al., 2019). Additional reagents specific to HNSCC organoids are also added, including B27 supplement, Glutamax, fibroblast growth factors (FGF) 2 and 10, forskolin, prostaglandin E2 (PGE_2), and Y-26732 (Driehuis et al., 2019; Farnebo et al., 2015; Tanaka et al., 2018). B27 supplement contains a variety of hormones and other molecules designed to promote cell proliferation without differentiation, while FGF2 and 10 induce differentiation of the organoid stem cells into epithelial cells (Karakasheva et al., 2020). Glutamax is a glutamine substitute that provides an alternative energy source for organoid cells when they are undergoing mitosis, while also providing a nitrogen source for protein and nucleic acid synthesis (Wilson et al., 2021). Forskolin is used to promote cell profileration by increasing intracellular levels of the mitogen cyclic AMP (cAMP), while PGE_2 has been identified as improving the viability of eptithelial cells within the organoid (Driehuis et al., 2020; Yoon et al., 2020) Y-26732 is a Rho-associated protein kinase (ROCK) inhibitor that prevents cell dissociation-mediated apoptosis, thereby allowing source tissue cells for organoid growth to be seeded as single cells (Driehuis et al., 2019). Passaging of these organoid lines typically occurs between 8-14 days, with either Trypsin, TrypLE or Liberase being used to split the organoid cells into single cell suspensions (Driehuis et al., 2019; Karakasheva et al., 2020; Tanaka et al., 2018). However, all HNSCC organoid culturing protocols that have been published to date have used patient tumours directly as their source material, instead of PDX tumours. As a result, the suitability of these protocols for PDX-derived HNSCC organoids is not currently known. Nevertheless, these protocols serve as a useful starting point for the development of a specific protocol for PDX-derived HNSCC organoids.

1.6 Aims

1. To establish an organoid model for Human Papillomavirus (HPV)-negative Head and Neck Squamous Cell Carcinoma (HNSCC) derived from patient-derived xenograft (PDX) tumours.
2. To evaluate the ability of PDX-derived organoid models of HPV-negative HNSCC to successfully recapitulate morphology and gene expression of human tumours.
3. To assess the utility of PDX-derived HNSCC organoids for evaluating drug therapies, using the hypoxia-activated prodrug evofosfamide.

2 Methods

2.1 Table of Suppliers

Table 2.1: Table of Reagents used in this project with their suppliers.

Reagent	Supplier	Location
A-83-01	Tocris (Cat No. 2939)	Bristol, UK
Advanced DMEM/F12 Culture Medium	Thermo-Fisher Scientific (Cat No. 12634028)	Waltham, MA, USA
Agarose (2%)	ACSRC (prepared onsite)	Auckland, New Zealand
AlphaMEM Culture Medium	Thermo-Fisher Scientific (Cat No. 12561056)	Waltham, MA, USA
B27 Supplement	Thermo-Fisher Scientific (Cat No. 17504001)	Waltham, MA, USA
CAT Haematoxylin	BioCare Medical (Cat No. CATHE)	Pacheco, CA, USA
CellTiterGlo 3D Cell Viability Assay	ProMega (Cat No. G9681)	Madison, WI, USA
CHIR-99021	Sigma Aldrich (Cat No. SML-1046-5MG)	St. Louis, MO, USA
Chloroform	Emsure (Cat No. 1024451000)	Kenilworth, NJ, USA
Citrate Buffer (10 mM)	ACSRC (prepared onsite)	Auckland, New Zealand
CitiFluor AF1 Mountant	Electron Microscopy Sciences (Cat No. E17970-25)	Hatfield, PA, USA
Cultrex Reduced Growth Factor Basement Membrane Extract Type 2	R&D Systems (Cat No. 3533-010-02)	Minneapolis, MN, USA
Dispase II	Gibco (Cat No. 17105-141)	Grand Island, NY, USA
Dimethyl Sulfoxide (DMSO)	Sigma-Aldrich (Cat No. D8418)	St. Louis, MO, USA
DPX Mountant	Sigma Aldrich (Cat No. 44581)	St. Louis, MO, USA
Evofosfamide	MedKoo Biosciences (Cat No. 202901)	Morrisville, NC, USA
Eosin y Solution (1%)	Sigma-Aldrich (Cat No. HT110132	Auckland, New Zealand
Foetal Calf Serum	Moregate Biotech (Cat No. FBSF)	Hamilton, New Zealand
Forskolin	Tocris (Cat No. 1099)	Bristol, UK
GlutaMAX	Gibco (Cat No. 35050-061)	Waltham, MA, USA
Goat Serum	Life Technologies (Cat No. 50062Z)	Carlsbad, CA, USA
HEPES	ACSRC (prepared onsite)	Auckland, New Zealand

Hoechst 33342	Thermo-Fisher Scientific (Cat No. H3570)	Waltham, MA, USA
Human Epidermal Growth Factor (h-EGF)	PeproTech (Cat No. AF-100-15-500)	Waltham, MA, USA
Human Fibroblast Growth Factor 10 (h-FGF10)	PeproTech (Cat No. 100-26-50)	Waltham, MA, USA
Human Fibroblast Growth Factor 2 (h-FGF2)	PeproTech (Cat No. 100-18B-50)	Waltham, MA, USA
L-WRN Conditioned Medium	ACSRC (prepared onsite)	Auckland, New Zealand
N-Acetyl-L-Cysteine	Sigma Aldrich (Cat No. A9165-5G)	St. Louis, MO, USA
Nicotinamide	Sigma Aldrich (Cat No. N0636-100G)	St. Louis, MO, USA
Penicillin-Streptomycin	Invitrogen (Cat No. 10378-016)	Waltham, MA, USA
Pimonidazole-fluorescein Isothiocyanate (FITC) antibody	Hypoxyprobe (Cat No. FITC-Mab)	Burlington, MA, USA
Primocin	InvivoGen (Cat No. ant-pm-1)	San Diego, CA, USA
ProLong Diamond AntiFade Mountant	Thermo-Fisher Scientific (Cat No. P36961)	Waltham, MA, USA
Prostaglandin E2	Tocris (Cat No. 2296)	Bristol, UK
TBS	ACSRC (prepared onsite)	Auckland, New Zealand
TBS-Tween20 (0.1%)	ACSRC (prepared onsite)	Auckland, New Zealand
Trizol Lysis Reagent	Ambion (Cat No. 15596018)	Waltham, MA, USA
Trypan Blue	Thermo-Fisher Scientific (Cat No. T10282)	Waltham, MA, USA
TrypLE Express	Thermo-Fisher Scientific (Cat No. 12605010)	Waltham, MA, USA
Y-26732	LC Laboratories (Cat No. Y-5301)	Woburn, MA, USA

Table 2.2: Table of Kits used in this project with their suppliers.

Kit	Supplier	Location
Bioo Scientific NextFlex Poly(A) Beads	PerkinElmer (Cat No. 512979	Waltham, MA, USA
Bioo Scientific NextFlex Rapid Direction qRNA-Seq kit 2.0	PerkinElmer (Cat No. 519853	Waltham, MA, USA
Qiagen miRNEasy Mini Kit	Qiagen (Cat No. 217004)	Hilden, Germany
Qubit High Sensitivity RNA Kit	Thermo-Fisher Scientific (Cat No. Q32852)	Waltham, MA, USA

Table 2.3: Table of software used in this project with their suppliers.

Software	Version	Supplier	Location
GraphPad Prism	9.3.1	GraphPad Software Inc.	San Diego, CA, USA
ImageJ	1.5.3	National Institutes of Health (USA)	Bethesda, MD, USA
Microsoft Excel	2020	Microsoft Corporation	Seattle, WA, USA

2.2 Organoid Culture:

2.2.1 Source Tissue for Organoid Culture

PDX tumours were established in NSG and NOD scid mice at the University of Auckland from HNSCC patient specimens collected at Auckland City Hospital as carried out by Harms et al (2019). Cryopreserved tumour fragments (1-2 mm) from PDX tumours that had previously undergone two passages in mice were surgically engrafted onto bilateral flanks of NOD scid mice to form third generation (P3) PDX tumours. Once the tumours reached approximately 800-1500 mm^3 in volume the animals were euthanised and the tumours were collected. A small portion of each tumour (~125 mm^3) was resected and sliced into fragments of 1-2 mm in diameter, prior to being subjected to the cell culture steps listed below. All animal work followed protocols approved by the University of Auckland Animal Ethics Committee (#2256) and was undertaken by technical staff within the Auckland Cancer Society Research Centre (ACSRC).

2.2.2 Initial Seeding of Organoids

Immediately following fragmentation, the PDX fragments were immersed in 2 mL 0.13% wt/vol Trypsin for a period of 60 min, in order to allow for the tumour material to fully dissociate. Dissociation was deemed to be complete when the cell-containing solution became cloudy with small clusters of approximately 2-10 cells. This solution was then transferred to a 100 µm cell strainer attached to a 15 mL Falcon tube, prior to being washed with advanced DMEM/F12 with 3 additional substituents added; 100 U/mL Penicillin-Streptomycin, 10 mM HEPES and 1 x GlutaMAX (hereafter referred to as adDMEM/F12+++). This solution was then centrifuged at 200 g at 4 °C for 5 min, with the supernatant aspirated immediately afterwards. The pellet was then resuspended in 10 mL adDMEM/F12+++ and mixed thoroughly. An average cell count per mL was obtained by transferring 0.1 mL of suspension to the Coulter counter (Beckman Coulter, Cat# 6605700). This average cell count was used to determine the number of wells in a clear 24-well plate that the organoid cells would be seeded into. The cells were then centrifuged again, with the corresponding pellet being resuspended in 80% Cultrex Reduced Growth Factor Basement Membrane Extract Type 2 (BME), at a volume such that each well of a clear 24-well culture plate had 125,000 cells divided across 3 × 20 μL domes of BME.

After seeding, the 24-well plate was incubated at room temperature for 5 min, before being transferred to a 37 °C cell culture incubator maintained at 20% O_2 and 5% CO_2 partial pressures for 20 min to allow the BME to solidify. The culture plate was then inverted and returned to the incubator for an additional 1 h to ensure that the cells were evenly distributed within the BME dome. Following this, 500μL of supplemented adDMEM/F12+++ medium (hereafter referred to as Organoid Medium) was added to each well, containing 10% L-WRN conditioned medium (culture media collected from L-WRN cells cultured at the ACSRC that express and secrete Wnt, R-spondin and Noggin proteins during culture), 1 × B27 supplement, 1.25 mM N-acetyl-L-cysteine, 10 mM nicotinamide, 50 ng/mL human epidermal growth factor (hEGF), 10 ng/mL human fibroblast growth factor 10 (hFGF-10), 5 ng/mL human fibroblast growth factor 2 (hFGF-2), 500 nM A83-01, 1 μM prostaglandin E_2 (PGE_2), 0.3 μM CHIR-99021 and 1 μM forskolin. Until the second passage, 10 μM Y-26732 and 50 mg/mL primocin were also included in the culture medium.

2.2.3 Maintenance of Cell Cultures and Passaging

Organoid medium was refreshed every 2-3 days by completely aspirating the existing medium and re-immersing the BME domes in fresh organoid medium. Representative photographs were captured during the growth period.

The organoids were passaged every 10-12 days. Firstly, the BME domes were mechanically disrupted by pipetting the medium inside each well up and down using a P1000 pipette tip pre-wet with adDMEM/F12+++, prior to being transferred to a 15 mL Falcon tube containing 6 mL adDMEM/F12+++ (up to 12 wells per tube). These were then centrifuged at 200 × *g* for 5 min at 4 °C and the supernatant subsequently aspirated. The organoids were treated with 1 mL of 1X TrypLE (Thermo Fisher Scientific, Waltham, USA) for up to 10 min to split them and form a single cell suspension, before being resuspended in 10 mL adDMEM/F12+++. These were centrifuged again at 200 × g for 5 min at 4 °C and the supernatant subsequently aspirated, leaving behind approximately 200 µL of adDMEM/F12+++ on the cell pellet. The cells were then equilibrated in the remaining adDMEM/F12+++ by pipetting up and down. A 10 µL sample of the cell suspension was diluted 1:1 in Trypan blue dye and transferred to a C-Chip haemocytometer (NanoEnTek, Seoul, South Korea) in order to obtain an approximate total cell count using the following formula:

$$Approximate\ total\ cell\ count = \left(\frac{Cell\ count\ from\ 4\ large\ squares}{4} * 2 * 10^4\right) \div 5$$

Based on the observed cell count, the cells were then re-seeded in a new 24-well cell culture plate at a density of 125,000 viable cells per well as per Part A.

2.2.4 Cryopreservation of Organoid Samples

Three days after the first passage, a subset of each organoid model was processed in preparation for long-term storage in the ACSRC liquid nitrogen dewars. Firstly, the BME domes were mechanically disrupted by pipetting up and down with a filter-tip P1000 pipette and transferred to a 15 mL Falcon tube. Organoids were then resuspended in a freezing medium containing 10% DMSO, 20% Foetal Calf Serum (FCS) and 70 % Organoid Medium, at a ratio of 500 µL freezing medium for every 4 wells in the culture plate to be frozen. The organoids were then transferred to cryovials and placed in 'Mr. Frosty' freezing containers and stored at -80 °C overnight, before being transferred to liquid nitrogen dewars the next day.

2.3 Histology

HCT116 spheroid and organoid samples were prepared in parallel for haematoxylin and eosin (H+E) and pimonidazole staining, using the processes outlined in sections 2.3.1 to 2.3.8.

2.3.1 Organoid Harvesting for Histology

Organoid samples were prepared for histology 6 days after the first passage. Organoids were pre-treated in the 24-well culture plate for 3 h at 37 °C with a supplemented organoid medium containing 100 µM pimonidazole. This incubation was immediately followed by a 40-min incubation at 37 °C with adDMEM/F12+++ supplemented with 1 mg/mL dispase II in order to ensure complete dissolution of the BME. After dispase II treatment, the samples were harvested by transferring the contents of the 24-well culture plate to a single 15 mL Falcon tube containing 5-10 mL adDMEM/F12+++. This Falcon tube was centrifuged at 200 × *g* for 5 min at 4 °C and the supernatant aspirated.

2.3.2 HCT116 Spheroid Preparation and Harvesting for Histology

HCT116 spheroids were prepared and harvested for downstream histological sample processing in order to act as positive controls for the organoids. These cells are a human colorectal cancer cell line, and were obtained originally from the American Type Culture Collection and were authenticated by single tandem repeat profiling and confirmed to be mycoplasma negative by PlasmoTest (InvivoGen, San Diego, USA). HCT116 cells were seeded at 1,000 cells per well into a Costar 96-well Round-bottom ultra low-attachment (ULA) plate (Corning, New York, USA), before being centrifuged at 1,000 rpm for 3 min to bring the individual cells into close contact with each other and thereby encourage spheroid growth, with cells being prepared in 200 µL AlphaMEM culture medium containing 10% FCS and 1X Pen-Strep. Cells were grown for 7 days, with 100 µL of this medium being carefully substituted for fresh medium every second day after day 4.

After completion of the culture steps, the corresponding spheroids were harvested and transferred to a 15 mL Falcon tube, prior to being washed twice with PBS and centrifuged, with the supernatant aspirated.

2.3.3 Sample Processing

The samples (both organoids and HCT116 spheroids) were then fixed by resuspending the pellet in 1 mL of 10% neutral buffered formalin (NBF) and left to incubate overnight at room temperature. On the following day, the samples were centrifuged twice more at 1,000 rpm for 3 minutes and the supernatant aspirated each time, first to allow for the removal of excess 10% NBF and then to facilitate a wash step with phosphate-buffered saline (PBS). The samples in PBS were then mixed with 2% agarose inside a clear plastic histology mould, which was then placed on ice to allow a solid dome to form. Upon complete solidification, the histology mould was then peeled from the dome, which was then immersed overnight in 10% NBF. The dome was then transferred to a histology cassette, before being stored in 70% ethanol until ready for paraffin embedding.

2.3.4 Slide Preparation for Staining

Solidified agarose domes were embedded in paraffin wax, prior to being sliced into 4-6 μm sections using a rotary microtome. These sections were then placed on a glass microscope slide in preparation for haematoxylin and eosin (H+E) and pimonidazole staining, with 2-4 sections being included per slide.

2.3.5 Haematoxylin and Eosin Staining

Prior to carrying out H+E staining, slides were deparaffinised and rehydrated by a two-step process. Firstly, slides were heat treated in an oven set to 60 ºC for 20 min in order to melt away the excess paraffin found on the edges of each slide. This was followed by two 5-min immersions in xylene and subsequent rehydration by two 3-min immersions in 100 % ethanol, designed to remove the paraffin found in the centre of the slide, near the organoid sections.

Staining with CAT haematoxylin was carried out immediately after rehydration for 3 min, followed by a wash step in tap water to remove excess stain. The sections were then differentiated by treatment with 1% acid alcohol, followed by blueing with 1% lithium carbonate, with the sections being washed until clear in tap water after both of these steps. The sections were then eosin-stained by dipping 4 times in 1% Eosin y solution, which was then washed until clear in tap water and allowed to dry out. Once the sections were dry, the sections were treated with DPX or CitiFluor AF1 mountant and a LabServ SuperFrost Plus 1mm (LabServ, Arlington, TX, USA) coverslip applied, which was allowed to set overnight at room temperature.

2.3.6 Haematoxylin and Eosin Image Capture

H+E images were captured using a Zeiss Axio Imager M2 (Zeiss, Oberkochen, Germany) microscope located in the Biomedical Imaging Research Unit (BIRU) at the University of Auckland. Slides containing organoids were selected manually, with a single slide loaded into the microscope at a time. This enabled organoid images to be captured using the objective lens at 40× magnification, with Kohler illumination being configured for each individual organoid slide.

2.3.7 Pimonidazole Staining

As there were multiple sections placed on each slide, a diamond plate scraper was used to mark the boundaries of the different sections on each slide. Slides allocated for pimonidazole staining also had to undergo a deparaffinisation and rehydration process, although this process was different to that carried out for H+E. The slides were heat-treated at 58 ºC for 1 h, which was followed by two 10-min immersions in xylene. Rehydration was carried out by two 2-min immersions in 100% ethanol, which was followed by a 5-min wash step in distilled water. These slides were then transferred to TBS in preparation for antigen retrieval.

For antigen retrieval, the slides were transferred to 10 mM citrate buffer at pH 6, before being placed in an Antigen Retriever 2100 pressure cooker (Aptum Biologics, Southampton, UK) for 1 h. Slides were then washed 3 times for 5 min each; once in TBS, and twice in TBS-Tween20 (0.1%). The boundaries of each section were then outlined using the ImmEdge hydrophobic barrier pen (Vector Laboratories, Newark, CA, USA). Blocking was then carried out by treating each individual section with 50 µL of 10% goat serum in TBS-Tween20 (0.1%), with the slides then being incubated for 1 h at 4 ºC. Afterwards, the blocking solution was removed and replaced with 50 µL of antibody solution, comprised of Pimonidazole-FITC antibody diluted 50-fold in TBS-Tween20 (0.1%) containing 5% goat serum, before the slides were incubated overnight at 4 ºC.

The following day, the slides were subjected to three 5-min wash steps; twice with TBS-Tween20 (0.1%), and once with TBS. Samples were then counter-stained, by incubating the cells for 10 min in TBS containing 5 µM Hoechst 33342 nuclear stain for 10 min. The slides were then treated with ProLong Diamond AntiFade mountant with each section on each slide receiving 80 µL of mountant. The slides were then transferred to a cardboard microscope slide box and stored overnight at room temperature in order for the mountant to cure.

2.3.8 Pimonidazole Image Capture

Pimonidazole images were captured using the same Zeiss Axio Imager M2 microscope as was used for H+E brightfield imaging, with one slide being loaded at a time into the microscope. The DAPI filter (385 nm, exposure 0.015 s) was used for Hoechst 33342 imaging, while the FITC filter (470 nm, exposure 0.227 s) was used for pimonidazole imaging. ImageJ version 1.5.3 was utilised to align and overlay the corresponding Hoechst 33342 and pimonidazole images.

2.4 Preparation for RNA Sequencing

RNA samples were extracted from organoid models 6-7 days after the second passage as well as HCT116 spheroids after 7 days' culture in a ULA plate.

2.4.1 RNA Extraction

For the organoid samples, organoid medium was aspirated and 500 µL of Trizol was added to the first organoid-containing well to lyse the cells. This was followed by pipetting up and down to ensure complete dissolution of BME by the Trizol and equilibration of the cell lysate. This solution was then transferred to the next organoid containing well, and the process repeated until all organoid-containing wells had been equilibrated.

96 wells of HCT116 spheroids from were collected from the ULA plate by centrifuging thr plating and aspirating their culture medium, which was followed by their transfer to a 1.5 mL Eppendorf tube. These spheroids were then treated with 500 µL of Trizol inside this tube and pipetted up and down to ensure complete lysis within the spheroid cells.

The corresponding organoid and HCT116 lysates were then transferred to a PhaseMaker^{TM} tube (Thermo Fisher Scientific, Waltham, MA, USA) and 20% v/v chloroform (100 µL) added, prior to being vortexed for 15 s. Samples were then allowed to incubate at room temperature for 3 min, prior to being centrifuged at 13,000 rpm for 15 min at 4 °C for phase separation. After the phase separation had finished, the supernatant inside the PhaseMaker tube (aqueous phase) was transferred to a fresh RNAse-free Eppendorf tube, prior to 900 µL of 100% ethanol being added to the tube, which represents 1.5 × the combined volume of Trizol and chloroform used.

All subsequent steps were carried out according to the RNA extraction protocol stated in the miRNEasy mini kit (Qiagen, Hilden, Germany). A miRNEasy mini column was placed inside a 2 mL collection tube, before 700 µL of sample was transferred to it and centrifuged at 8000 × *g* for 15 s at room temperature. This step was then repeated for any additional sample remaining in the RNAse-free Eppendorf tube. The samples were then washed with 700 µL of buffer RWT and centrifuged at 8000 × g for 15 s at room temperature. Two additional wash steps were then carried out with 500 µL buffer RPE, followed by centrifugation at 8000 × *g* for 15 s for the first wash and for 2 min after the second wash. Buffer RPE was allowed to sit on top of the sample for one min during the first wash prior to centrifugation to aid dissolution of any salts present, including guanidine salts from the Trizol and buffer RWT. After washing, the miRNEasy mini column was transferred to a new 2 mL collection tube and centrifuged at full speed for 1 min to dry the membrane. To elute the RNA, the miRNEasy mini column was transferred to a new 1.5 mL collection tube, 20 µL of RNAse-free water added, followed by centrifugation at 8000 × g for 1 min. To ensure complete elution of RNA, the filtrate was added back into the column and centrifuged for a second time.

2.4.2 Quality Control

Immediately after extraction, initial yield and quality of RNA was determined using the NanoDrop (Thermo Fisher Scientific, Waltham, MA, USA) spectrophotometer. After these measurements were taken, samples were then transferred to the -80 °C freezer to prevent RNA degradation. Additionally, prior to carrying out downstream processing steps, TapeStation (Agilent, Santa Clara, California, USA) was utilised to determine the true RNA yield and sample quality, assessed through a RINe (RNA Integrity Number) score. Only samples with a RINe score greater than 6 and a total yield greater than 10 ng were utilised for downstream processing.

2.4.3 PolyA Enrichment and cDNA Preparation

To enrich the total RNA extracted for mRNA, the Bioo Scientific NEXTflex Poly(A) Beads 2.0 kit was utilised according to protocol. Following PolyA enrichment, the Bioo Scientific Rapid Directional RNA-Seq Kit 2.0 was utilised to carry out cDNA preparation, with samples prepared according to protocol. For steps where a thermal cycler was required, the Eppendorf MasterCycler Nexus GX2 (Eppendorf, Hamburg, Germany) was utilised, with the sample temperatures outlined in Table 2.4.

Table 2.4. Thermal Cycler temperatures used for cDNA preparation.

Protocol Step	Plate Temperature (^{o}C)	Time (min)
A: RNA Fragmentation	94	15 (if RINe > 7) 12 (if 6 < RINe < 7)
B: First Strand Synthesis	25	10
	50	15
	70	10
C: Second Strand Synthesis	16	60
D: Adenylation	65	30
E: Adapter Ligation	20	15
F: PCR Amplification	98	0.5
14 cycles if RNA yield < 100 ng	98	0.25
12 cycles if RNA yield > 100 ng	65	0.5
	72	0.5
End	72	2

2.5 Evofosfamide Drug Treatment Assays

Drug sensitivity of the organoids to evofosfamide was assessed using a modified CellTiterGlo3D cell viability assay.

2.5.1 Cell Preparation

Organoids were grown out for 6 days after the first passage. Mechanical disruption of the BME domes and trypsinisation was then carried out as per Section 2.2.3 in order to form a single cell suspension. However, the trypsinisation reaction was terminated by resuspending the cells in organoid medium containing 5% BME (OM5%) instead of the adDMEM+++ used for regular organoid passaging. The cell suspension was then centrifuged at 200 × *g* for 5 min at 4 °C and the supernatant subsequently aspirated, with approximately 100 µL of OM5% left behind on the resulting cell pellet. The cell pellet was then equilibrated in the remaining OM5% by pipetting up and down, before a 10 µL sample was mixed 1:1 with Trypan blue stain and transferred to a C-Chip haemocytometer in order to obtain an approximate total cell count using the following formula:

$$Approximate\ total\ cell\ count = \left(\frac{Cell\ count\ from\ 4\ large\ squares}{4} * 2 * 10^4\right) \div 10$$

Based on this calculation, cells were then seeded into a 96-well Round-bottom ULA plate at 2,000 cells per well, with OM5% added so that the total volume of solution in each well was 50 µL. The ULA plates were then centrifuged at 1000 rpm for 3 min to ensure that the single cells sank to the bottom of each well in order to increase cell-to-cell contacts and encourage organoid growth in-plate. Fourteen such wells were seeded for each evofosfamide treatment assay; 12 to allow a range of 6 different evofosfamide concentrations ranging from 0.096 µM to 300 µM to be tested in duplicate and 2 to serve as negative (drug-free) controls. Eight media-only wells were also included per plate, with two of these wells being treated with the Cell Titre Glo 3D solution to act as a positive control. 50 µL PBS was added to all unused wells to minimise evaporation and edge effects.

Upon completion of the cell seeding, the ULA plate was returned to the 37 °C incubator overnight. The following day, a further 50 µL of OM5% or PBS was added to each well of the ULA plate, before being returned to the 37 °C incubator for a second overnight incubation.

2.5.2 Drug Treatment

Eight µL of a 30 mM evofosfamide stock solution was added to 392 µL of OM5% in a 1.5 mL Eppendorf tube in order to prepare 400 µL of a 600 µM evofosfamide drug solution. This solution was then used to make six 5-fold serial solutions at twice the target in-well concentrations by transferring 80 µL of the previous dilution to a fresh 1.5 mL Eppendorf tube and adding 320 µL of OM5%. A volume of 100 µL was transferred from each Eppendorf tube to the experimental organoid-containing wells in duplicate so that the final in-well concentrations to be tested were 0.096, 0.48, 2.4, 12, 60 and 300 µM. The ULA plate was then returned to the 37 °C incubator for a further three days.

2.5.3 Data Collection

Upon completion of the three-day drug incubation, all organoids were lysed by treating with 40 µL of CellTiterGlo 3D solution (ProMega, Madison, WI, USA), covered in tinfoil and incubated at room temperature on a plate shaker set to 100 rpm for 30 min. Two of the six media-only wells were also treated with 40 µL CellTiterGlo 3D solution as a positive control. The lysates were then transferred to an opaque, clear-bottom 96-well plate (Corning, New York, USA) which was then read using the Enspire luminescence plate reader (PerkinElmer, Waltham, USA). Luminescence outputs were exported as an Excel CSV file for quality control, data normalisation and analysis.

2.5.4 Quality Control

Microsoft Excel was used to calculate the mean and standard deviations for the luminescence (lum) outputs for the positive ($\mathrm{Ctrl}^{\mathrm{pos}}$) and negative ($\mathrm{Ctrl}^{\mathrm{neg}}$) controls. These values were then used to calculate a Z’ score – an indicator of the dynamic range and quality of the assay – using the following formula:

$$Z' = 1 - \frac{(3 * \ SD[Ctrl^{neg}] + 3 * SD[Ctrl^{pos}])}{Mean\ lum\ Ctrl^{neg} - Mean\ lum\ Ctrl^{pos}}$$

Further downstream analysis was only carried out on assay data that had a Z’-score of 0.5 or greater.

2.5.5 Data Normalisation

Raw luminescence data from each experimental well were converted into percentage relative viability values using the following formula:

$$Organoid\ Viability: 100\% * \frac{Experimental\ well\ value - Mean\ lum\ Ctrl^{pos}}{Mean\ lum\ Ctrl^{pos} - Mean\ lum\ Ctrl^{neg}}$$

2.5.6 Analysis

The normalised relative viability data from Section 2.5.5 were transferred from Excel to GraphPad Prism version 9.3.1. The drug concentration values were log-transformed, prior to being subjected to a non-linear regression analysis to determine the IC_{50} value for evofosfamide in each organoid line. Two such experiments were carried out for each organoid line, allowing for the determination of a mean and standard error for IC_{50} between replicate assays.

3 Culture of PDX-derived HNSCC Organoids

3.1 Introduction

In earlier research, the ACSRC has developed over twenty novel PDX tumour models for HNSCC derived from primary tumour samples obtained from Auckland City Hospital. As part of this research project, 14 PDX tumours from 9 different PDX models (Table 3.1) were used to attempt to develop a range of novel organoid models for HNSCC, with those that were successfully established after two passages subsequently being used in downstream experiments to characterise their cellular morphology, gene expression activity and sensitivity to the hypoxia-activated prodrug evofosfamide. As can be seen from Table 3.1, most of the PDX tumours available for organoid generation were derived from primary tumours in the tongue. Due to there being no published records of PDX-derived organoids for HNSCC being developed, there is no established and optimised protocol to ensure their efficient and sustained growth. However, as Driehuis et al (2019) successfully established fifteen novel organoid lines for HNSCC directly derived from patient primary tumours, the culture protocols used in their research were closely analysed and used as a basis from which a culturing protocol for PDX-derived HNSCC organoids could be developed. As such, the 14 PDX tumours were minced, trypsinised, seeded and passaged as per the organoid culture protocol in Section 2.2. Organoid growth for each line was monitored every 2-3 days with representative images regularly captured on a light microscope as part of routine cell maintenance during the cell culture process. This enabled the determination of which PDX tumours were able to form organoids successfully, and from these organoid models, which ones could most successfully be utilised in the planned downstream experiments.

Table 3.1. Tumour site and type of the original patient specimen that the PDX tumour models used in this project to generate organoids were derived from.

Organoid Line	Tumour Site	Tumour Type
ACS-HN04	Tongue	Primary
ACS-HN06	Oropharynx	Recurrent
ACS-HN08	Tongue	Primary
ACS-HN09	Tongue	Primary
ACS-HN11	Tongue	Recurrent
ACS-HN14	Buccal Mucosa	Primary
ACS-HN18	Tongue	Primary
ACS-HN20	Tongue	Primary
ACS-HN23	Unconfirmed	Unconfirmed

3.2 ACS-HN04

Minced ACS-HN04 PDX tumour cells showed rapid growth into organoids following the initiation of culture, as shown by

Figure 3.1. Indeed, large organoids exceeding 100 µm diameter began to appear after only 3 days in culture. The ACS-HN04 organoids continued to grow rapidly, with numerous organoids exceeding 300 µm being observed after 12 days in culture, at which point the first passage was carried out. After this first passage, organoids were quickly re-established, with large organoids approaching 200 µm in diameter again visible after a further 3 days in culture (Day 15). However, this organoid culture had to be cryogenically frozen after 16 days in culture, due to a laboratory shutdown caused by COVID-19 lockdown restrictions.

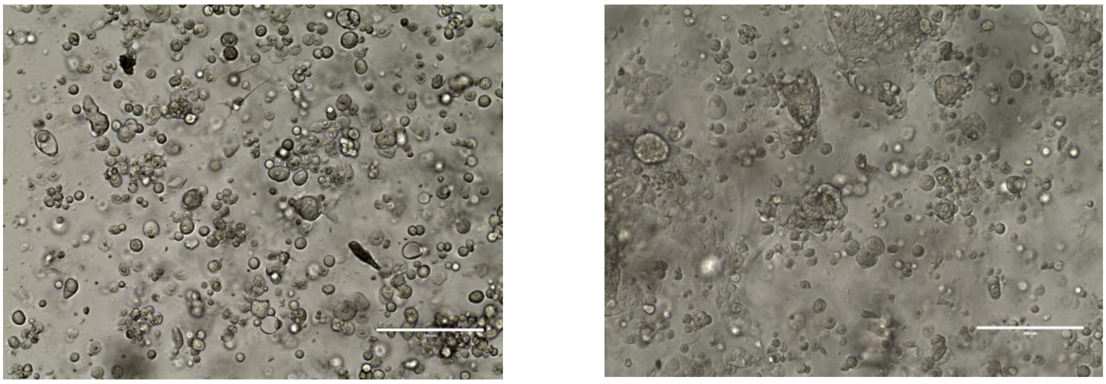

Day 3 (P0)

Day 7 (P0)

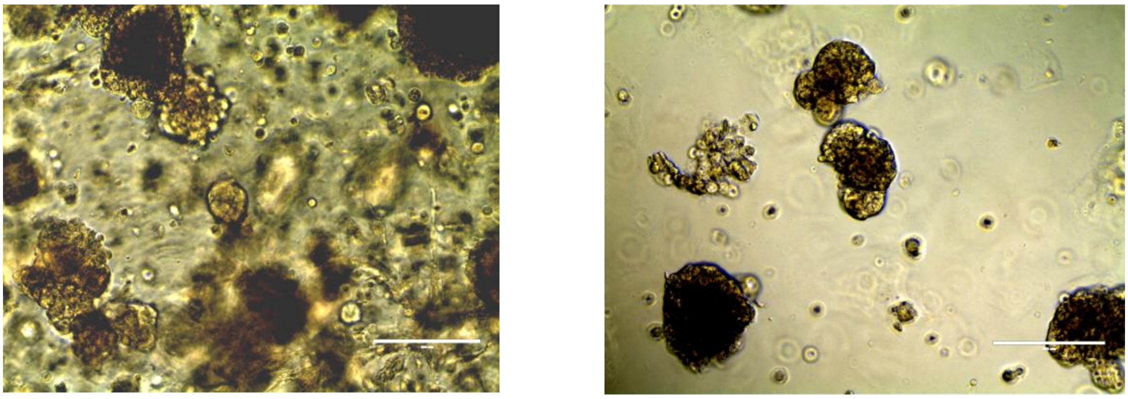

Day 12 (P0)

Day 15 (3 days after first passage)

Figure 3.1: Representative images of the ACS-HN04 organoid line captured by Evos digital light microscope before the first passage (P0), after 3, 7 and 12 days in culture as well as 3 days after the first passage (total 15 days in culture). Scale bars = 200 µm.

Upon the cessation of lockdown restrictions, this organoid line was successfully revived. As can be observed in

Figure 3.2, the organoids demonstrated successful resumption of growth, beginning to exceed 200 µm in diameter after only 5 days post-revival (a total of 21 days in culture). As a result, a second passage was carried out on this organoid line on day 23. After the second passage, some large organoids approaching 200 µm began to emerge by day 26. This growth trend appeared to accelerate somewhat, with numerous large organoids emerging by day 30, with some approaching 400 µm in diameter. In order to monitor whether this growth trend would continue beyond day 30, the organoids were kept in culture for a further 6 days, before being subjected to a third passage on day 36. After this third passage, some small organoids did form by day 40, although none exceeded 100 µm in diameter (

Figure 3.3). Furthermore, the Cultrex BME domes showed a lower level of confluence after this third passage, indicating that cell losses occurred during this passaging process. Beyond day 49, the organoids did not show any further signs of growth. Consequently, no further passages were carried out and the ongoing growth of the revived ACS-HN04 organoid culture was terminated on day 75.

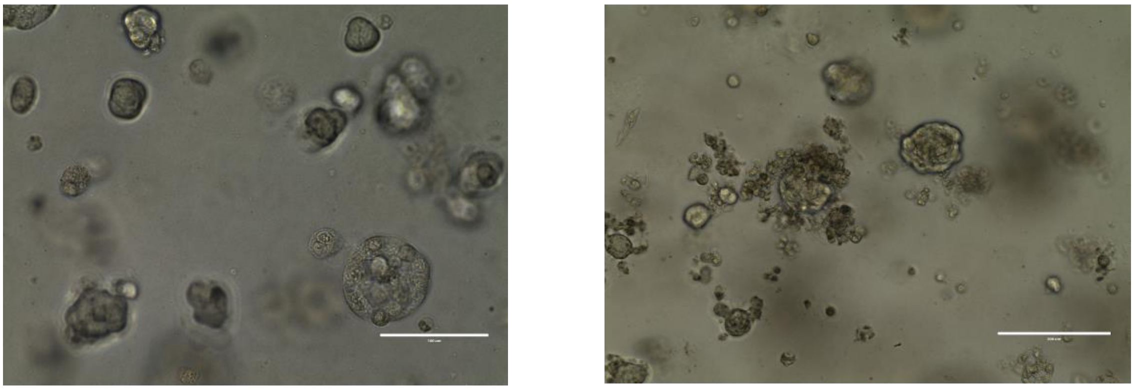

Day 15 (Post retrieval)

Day 21 (P1; 6 days post-retrieval)

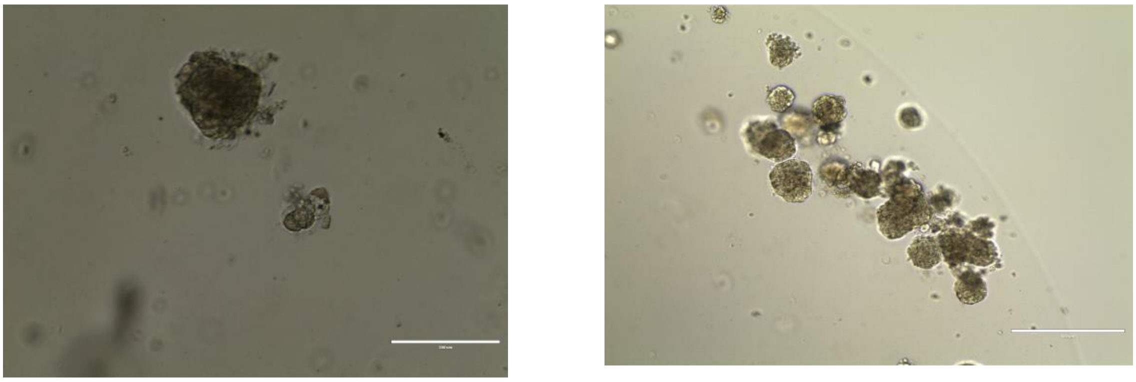

Day 26 (P2; 11 days post-retrieval)

Day 30 (P2; 15 days post-retrieval)

Figure 3.2 Representative images of the ACS-HN04 organoid line captured by Evos digital light microscope immediately after retrieval from cryogenic stores (day 15), and after 21, 26 and 30 days in culture with passage (P) number in brackets. Scale bars = 200 µm for all images except day 30, where the scale bar = 400 µM.

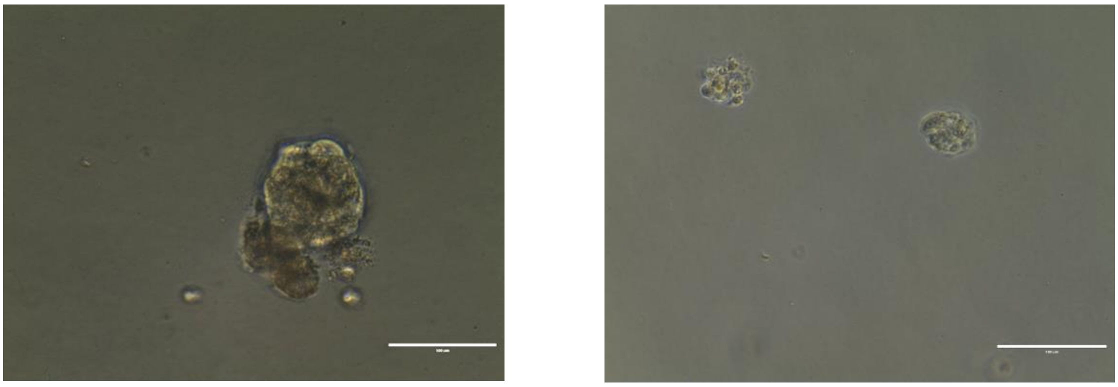

Day 40 (P3; 4 days after passage)

Day 49 (P3: 13 days after passage)

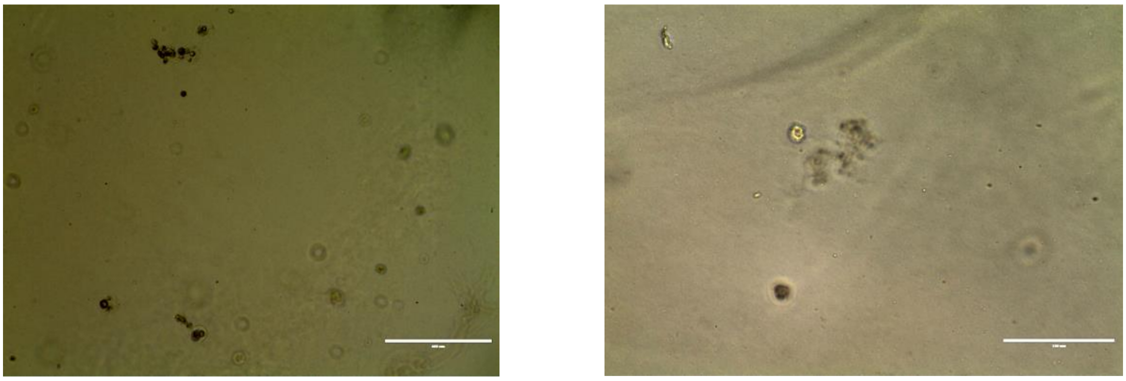

Day 60 (P3; 24 days after passage)

Day 75 (P3; 39 days after passage)

Figure 3.3. Representative images of the ACS-HN04 organoid line captured by Evos digital light microscope after 40, 49, 60 and 75 days in culture with passage (P) number in brackets. Scale bars = 100 µm for all images except Day 60, where the scale bar = 400 µM.

Given that these ACS-HN04 cells successfully established organoids upon seeding, and that these organoids successfully re-established after two passages, this line was chosen for subsequent protocol optimisation of the planned downstream experiments, which include histological stains, CellTiterGlo drug treatment assays with evofosfamide and RNA sequencing.

3.3 ACS-HN06

ACS-HN06 tumours, upon being minced and seeded into the 24-well culture plate, showed a distinct blade-like cell morphology, instead of the rounded morphology that all the other tumour models showed when seeded as single cells as part of this project. Nevertheless, as can be seen in

Figure 3.4, organoids did begin to form after 7 days in culture, and began to approach approximately 100 µm in diameter. This trend continued until day 12, when the first passage was carried out. Following this passage, the tumour cells remained as single cells until day 30, at which point these cells, like ACS-HN04 organoids, had to be cryogenically frozen due to COVID-19 lockdown restrictions.

An attempt was made to re-establish organoids from this PDX tumour by reviving the cryopreserved samples and re-seeding them in a 24-well culture plate. However, this attempt at establishing organoids was also unsuccessful, as the cells continued to remain as single cells. Consequently, no further passages were carried out, and this organoid culture was terminated after 73 days (Figure).

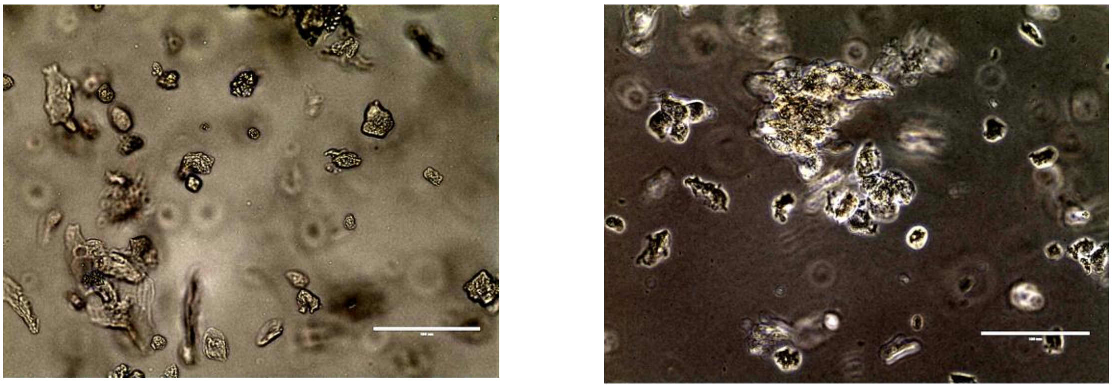

Day 4 (P0)

Day 7 (P0)

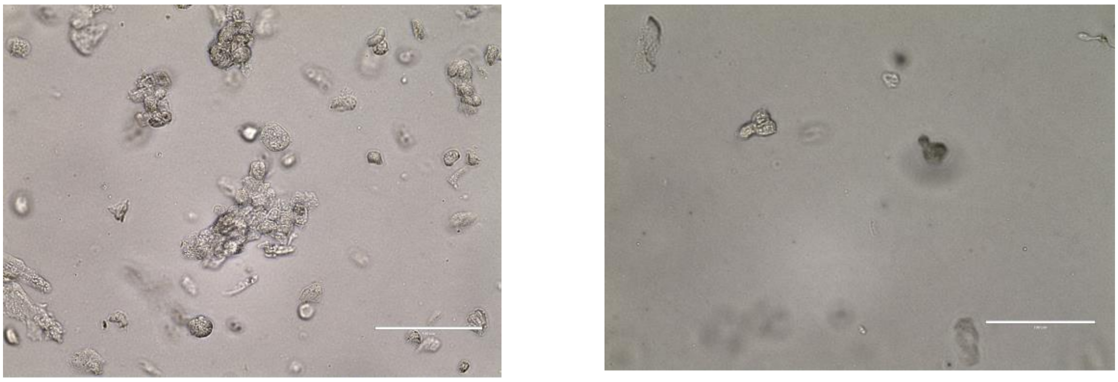

Day 11 (P0)

Day 18 (P1; 6 days after passage)

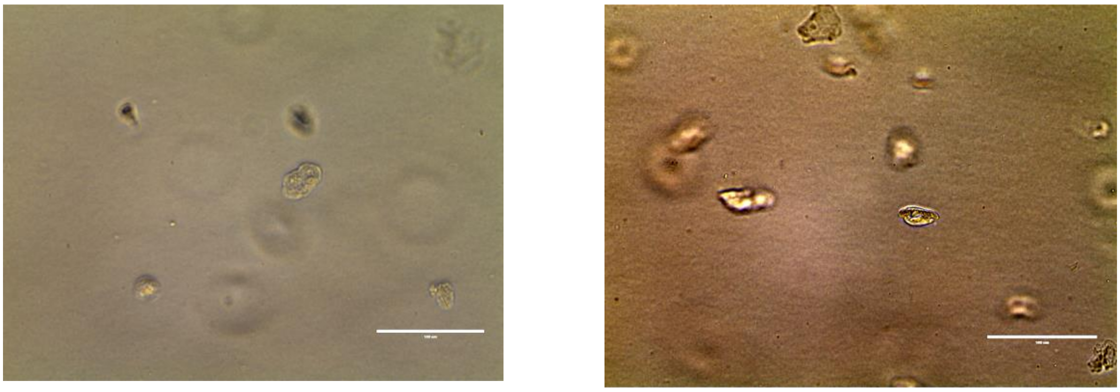

Day 23 (P1; 11 days after passage)

Day 28 (P1; 16 days after passage)

Figure 3.4 Representative images of the ACS-HN06 organoid line captured by Evos digital light microscope after 4, 7, 11, 18, 23 and 28 days in culture with passage (P) number in brackets. Scale bars = 100 µm.

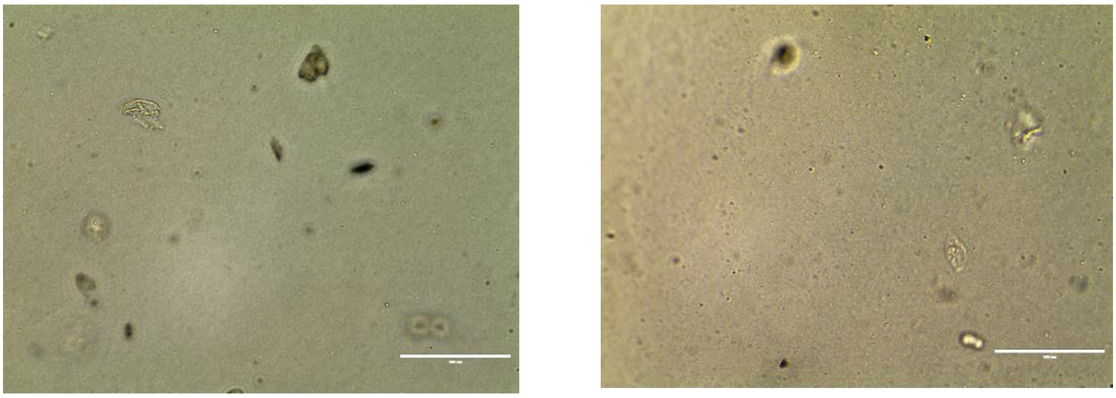

Day 40

Day 73

Figure 3.5 **Representative images of the ACS-HN06 organoid line captured by Evos digital light microscope after 40 and 73 days in culture and revival from cryopreservation on Day 30. Scale bars = 100 µm.**

3.4 ACS-HN08

ACS-HN08 organoid lines were retrieved from cryogenic stores in order to carry out culture prolongation as part of this project, having previously been cryogenically frozen after 1 passage and 18 days in culture as part of a pilot organoid culture attempt carried out by previous researchers in the ACSRC. These cells did not appear to show any signs of organoid development for 6 days post-retrieval (Day 24), with these cells instead remaining as isolated single cells (Figure 3.6). However, by Day 30, some large organoids began to emerge, with these organoids beginning to approach 100 µm in diameter. Based on these findings, a second passage was attempted on this organoid line on Day 37. Some organoids did re-establish after this passaging attempt by Day 46, although none exceeded 40 µm in diameter, with no further growth occurring beyond this time point. These cells were re-seeded at Day 80 without TrypLE in an attempt to re-stimulate organoid growth, but this attempt was unsuccessful. Consequently, ACS-HN08 culture was terminated at Day 87.

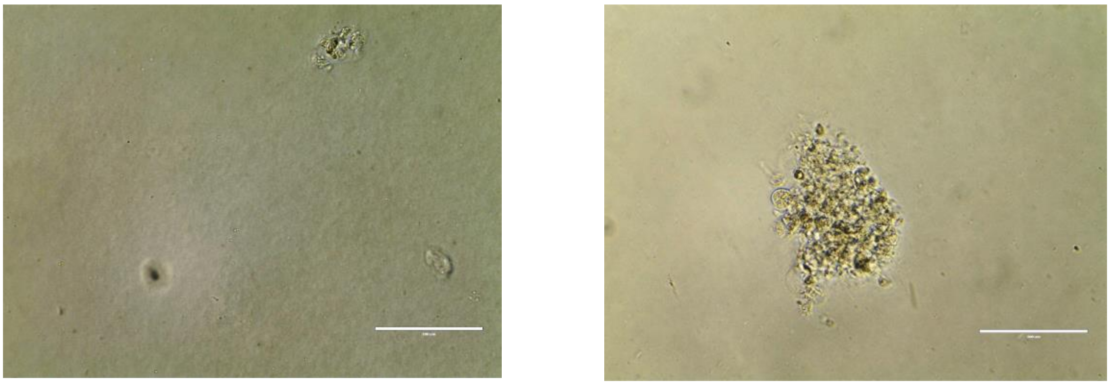

Day 24 (P1, 6 days after retrieval)

Day 30 (P1, 12 days after retrieval)

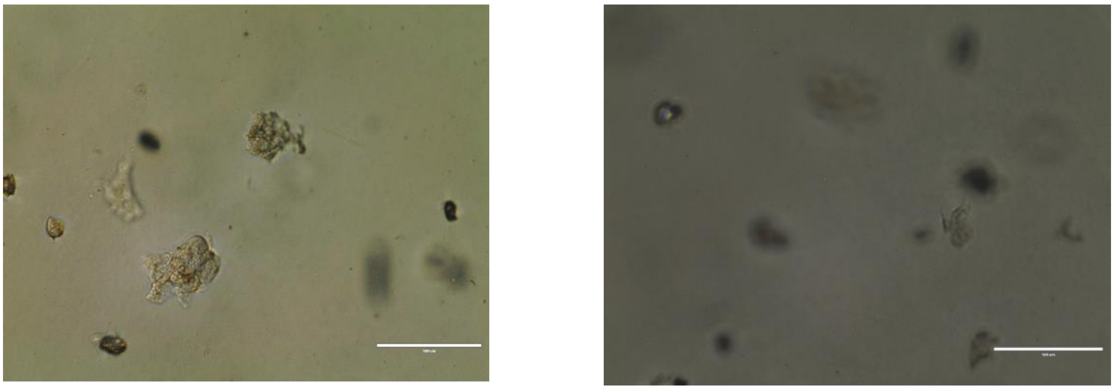

Day 46 (P2)

Day 74 (P2)

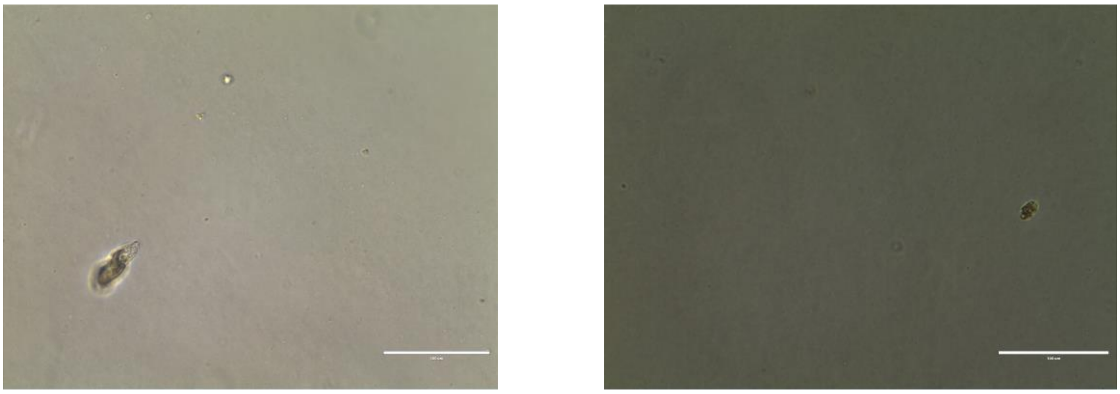

Day 80 (P3)

Day 87 (P3)

Figure 3.6 Representative images of the ACS-HN08 organoid line captured by Evos digital light microscope post retrieval from cryogenic stores, after 24, 30, 46, 74, 80 and 87 days in culture with passage (P) number in brackets. Scale bars = 100 µM.

3.5 ACS-HN09

When ACS-HN09 PDX tumours were minced and seeded as single cells into the 24-well culture plate, organoid formation did successfully occur. Compared to the ACS-HN04 organoids, the rate of formation was much slower, with the first organoids exceeding 100 µm diameter only appearing after 7 days in culture. However, between day 8 and day 10, the organoids growth rate appeared to accelerate, with some organoids beginning to approach 200 µm in diameter (

Figure 3.7). Based on this observation, the first passage was carried out on the following day (Day 11).

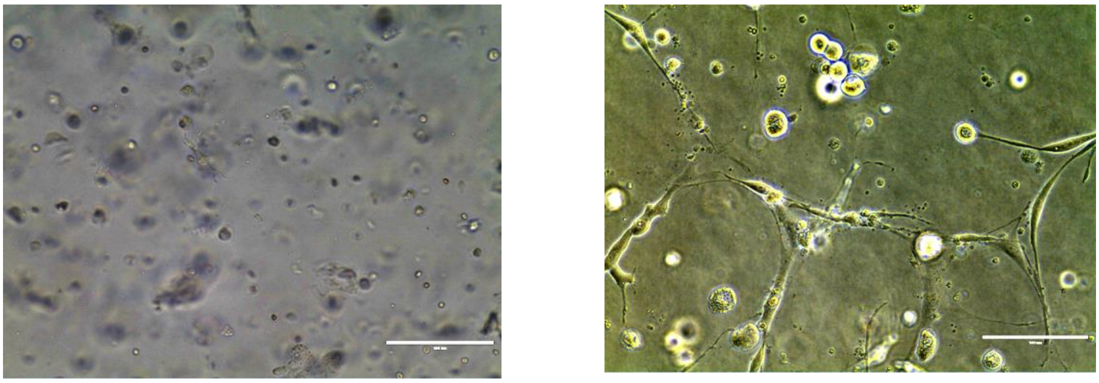

Day 0 (P0, immediately after seeding)

Day 3 (P0)

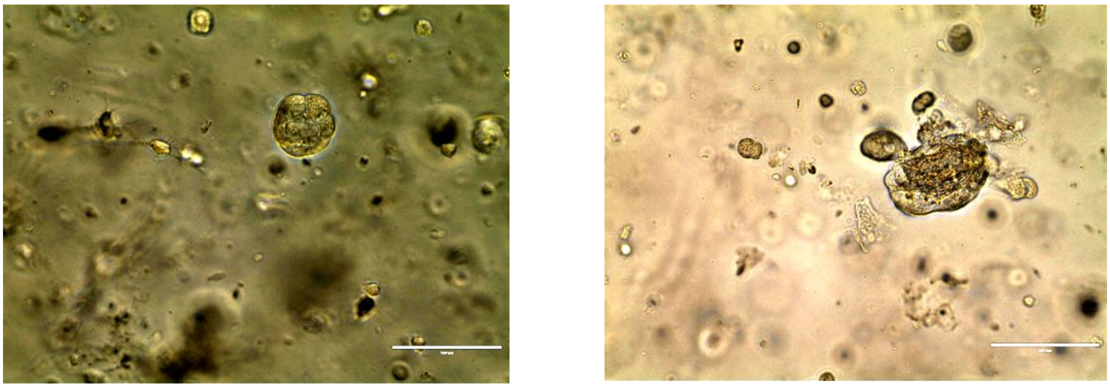

Day 7 (P0)

Day 10 (P0)

Figure 3.7 Representative images of the ACS-HN09 organoid line captured by Evos digital light microscope immediately after seeding (Day 0), and after 3, 7 and 10 days in culture with passage (P) number in brackets. Scale bars = 100 µM.

After the first passage, the ACS-HN09 organoids appeared to re-establish fairly rapidly, with some small organoids approaching 50 µm in diameter 3 days afterwards (day 14). As can be seen from

Figure 3.8, these organoids continued to grow, approaching 100 µm by day 17, at which point some of these cells were used for evofosfamide drug treatment assays. The cells not used for drug treatments continued to grow rapidly, approaching 150 µm by day 22. A second passage was carried out on day 23, with organoids subsequently being re-established and exceeding 100 µm diameter by day 26. Based on these observations of consistent growth across two passages, these organoids were used for characterisation after 27 days in culture, with no long-term culture being attempted on this organoid line.

Day 17 (P1)

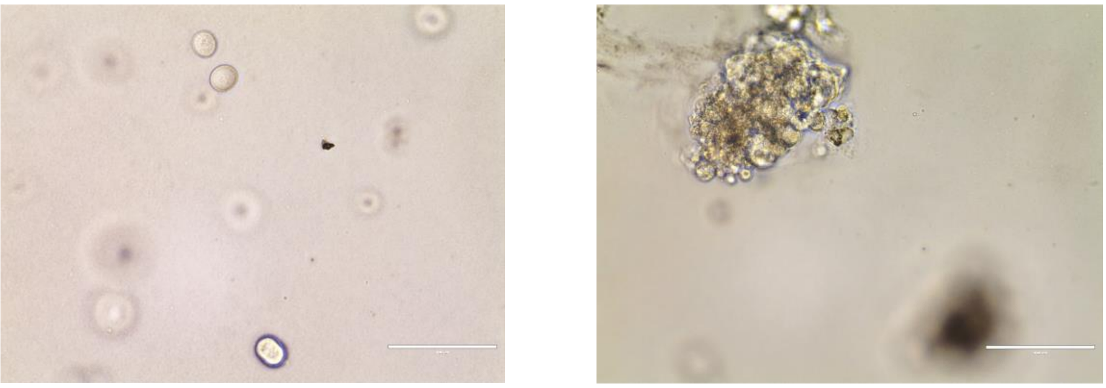

Day 23 (P2; immediately after)

Day 27 (P2; 4 days after passage)

Figure 3.8 Representative images of the ACS-HN09 organoid line captured by Evos digital light microscope after 17, 23 and 27 days in culture with passage (P) number in brackets. Scale bars = 100 µM.

3.6 ACS-HN11

HN11 organoids appeared to establish relatively rapidly, with the first organoids exceeding 100 µm in diameter by day 5. As can be observed from

Figure **3.9**, this trend appeared to be sustained until the first passage, which was carried out on day 17. Organoids approaching 100 µm in diameter began to re-emerge 8 days post-passage (Day 25), leading to a second passage being carried out on day 31. Successful organoid re-establishment did occur after this passage, although the largest organoids visible following this second passage only approached 60-70 µm in diameter after an additional 7 days in culture (Day 38). In an attempt to re-stimulate organoid growth following this observed slowdown in organoid growth rate, a third passage was carried out on day 46. However, this did not result in successful organoid re-establishment, instead leading to the organoids remaining as isolated single cells. Consequently, culture prolongation of this organoid lines was terminated after 87 days.

Organoid Culture

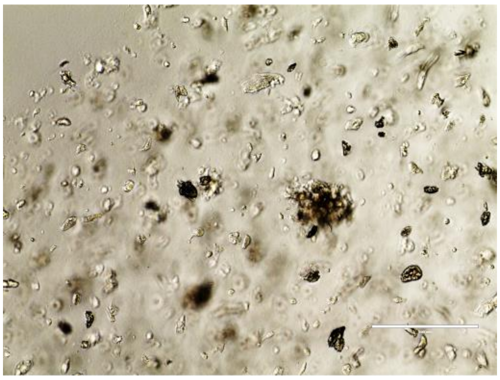

Day 5 (P0)

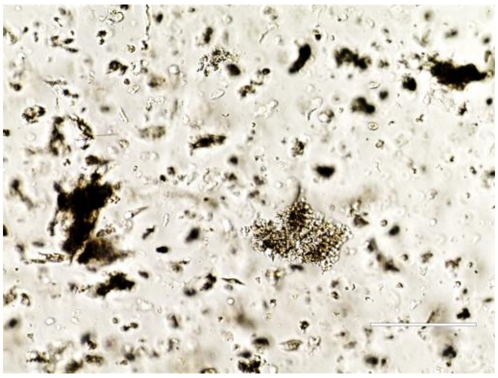

Day 14 (P0)

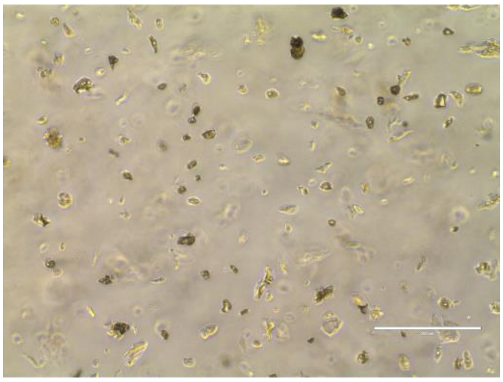

Day 24 (P1)

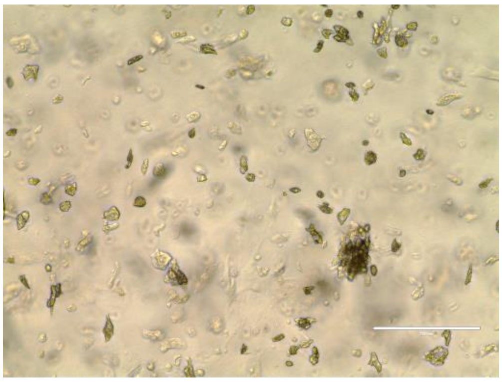

Day 26 (P2)

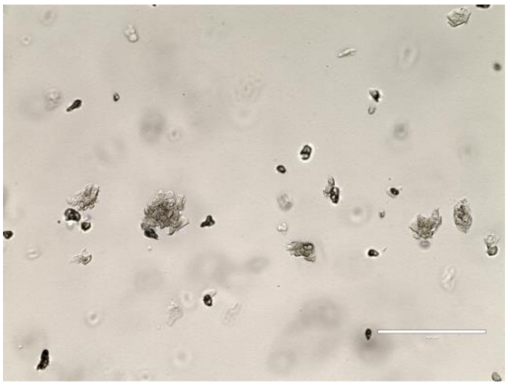

Day 38 (P2)

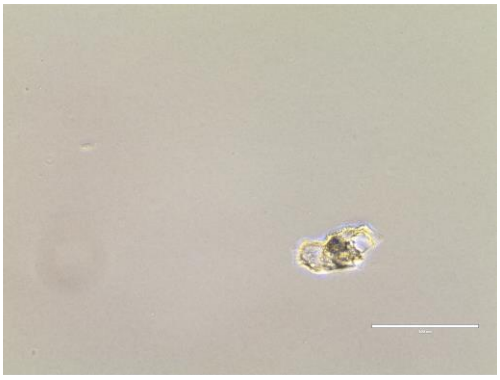

Day 46 (P3)

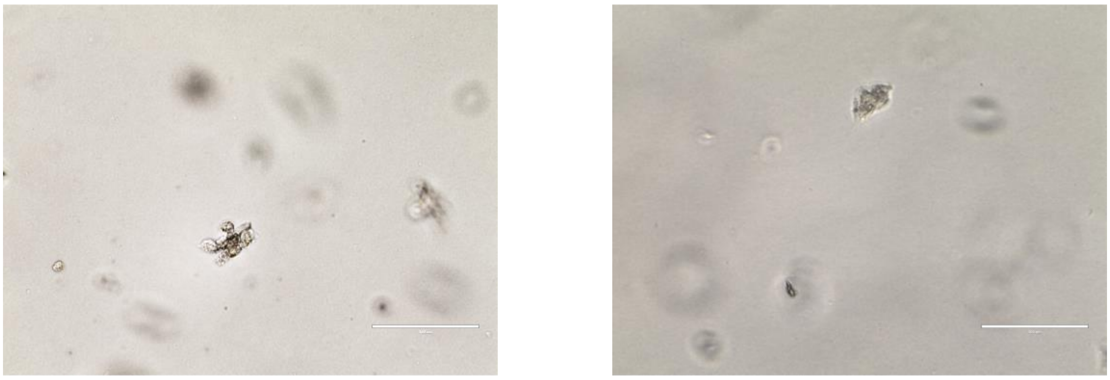

Day 49 (P3)

Day 52 (P3)

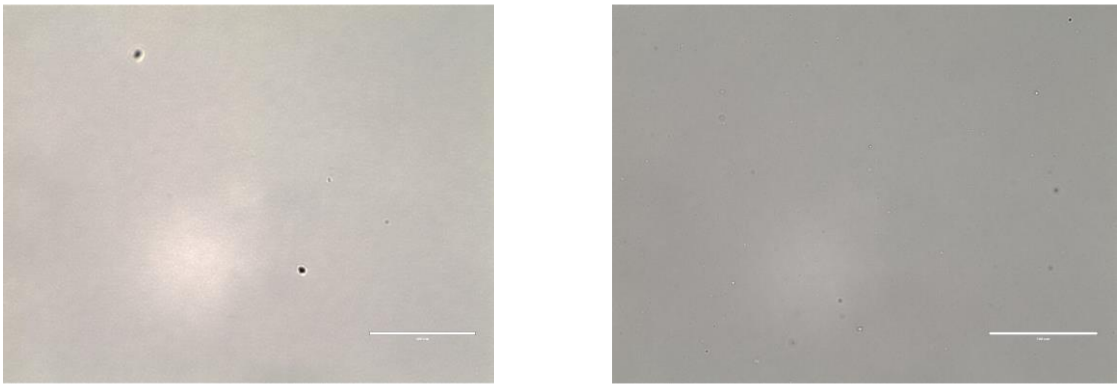

Day 62 (P3)

Day 70 (P3)

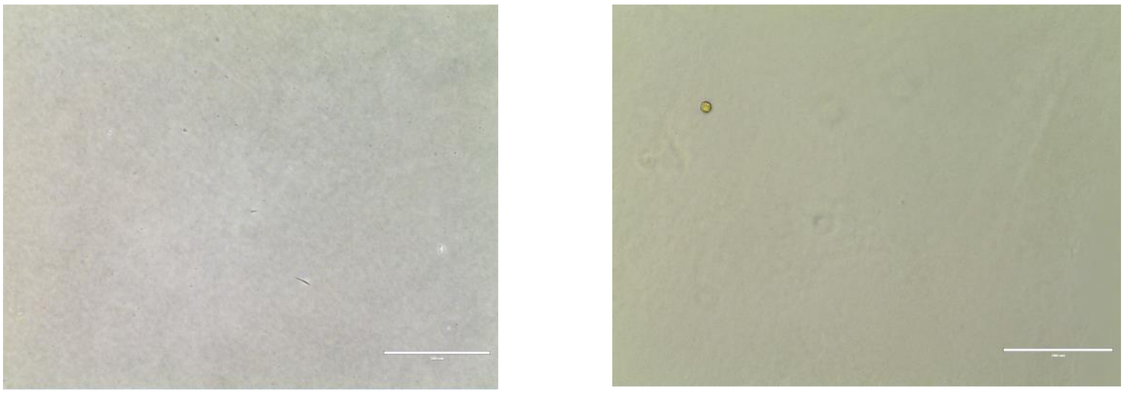

Day 80 (P3)

Day 87 (P3)

Figure 3.9. Representative images of the ACS-HN11 organoid line captured by Evos digital light microscope after 5-87 days in culture with passage (P) number in brackets. Scale bars = 200 µm

3.7 ACS-HN14

Organoid models were cultured from three distinct ACS-HN14 PDX tumours, labelled A, B and C in the chronological order in which they were cultured. Each of these organoid lines were derived from the same primary tumour, but were grown from three separate PDX tumours in three different mice.

3.7.1 ACS-HN14A

As can be observed from Figure 3.10, the ACS-HN14A cells failed to establish organoids after 25 days in culture. Instead, the tumour cells remained as disparate single cells which did not appear to show any signs of growth throughout the cell culture period. As a result, no passaging was attempted on this line and cell culture was terminated after day 25.

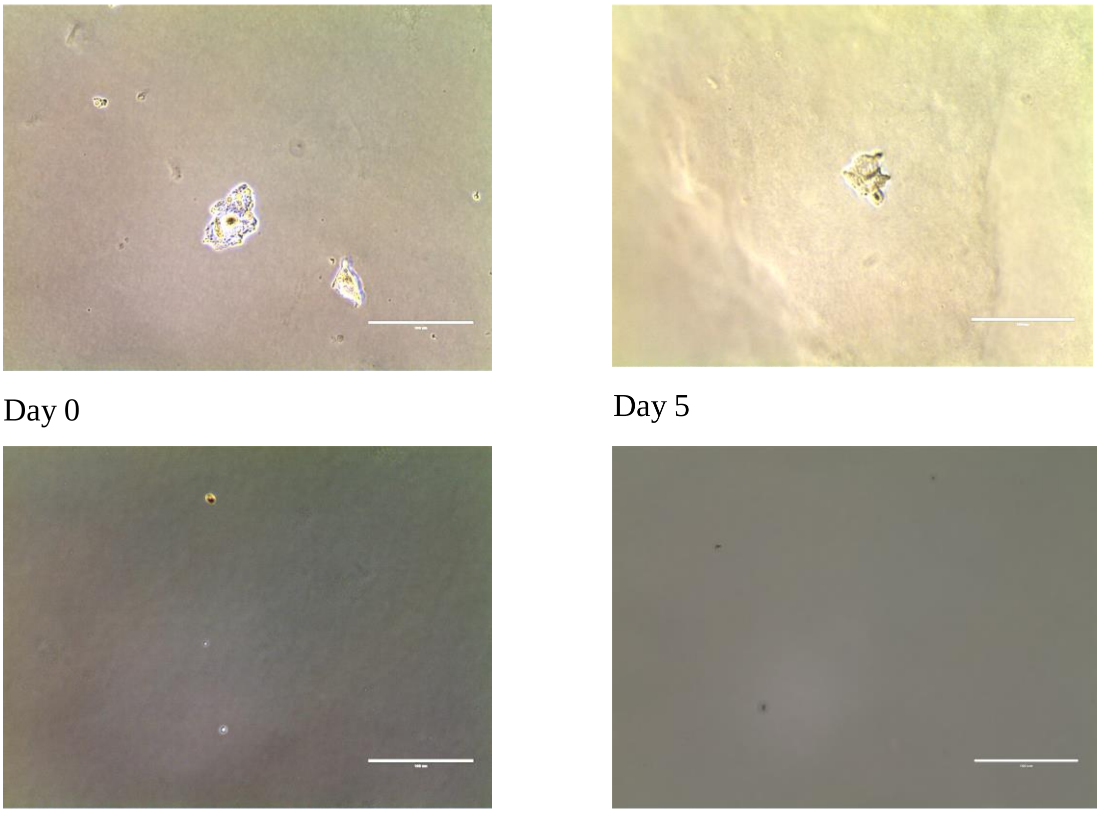

Day 0

Day 5

Day 14

Day 25

Figure 3.10. Representative images of the ACS-HN14A organoid line captured by Evos digital light microscope immediately after seeding (Day 0) and after 5, 14 and 25 days in culture. Scale bars = 100 µm

However, shortly after cell culture was terminated, it was identified that seven of the key reagents that comprise the organoid culture medium (hEGF, hFGF-10, hFGF-2, A83-01, PGE_2, CHIR-99021 and forskolin) used were over-diluted by 10-fold relative to their planned concentrations.

3.7.2 ACS-HN14B

In order to determine whether preparing the medium with the correct reagent concentrations would enable ACS-HN14 organoid formation, a second ACS-HN14 organoid line was plated, this time with the correct medium concentrations. One day after seeding, the isolated single cells were the prevailing morphology (

Figure 3.11). The first large organoids approaching 100 µm in diameter began to appear after 5 days in culture, with more of these larger organoids appearing by day 12. When the organoids were imaged on day 19 immediately prior to the first passage, several large organoids exceeding 200 µm in diameter were observed. Moreover, these organoids were evenly distributed across the BME domes.

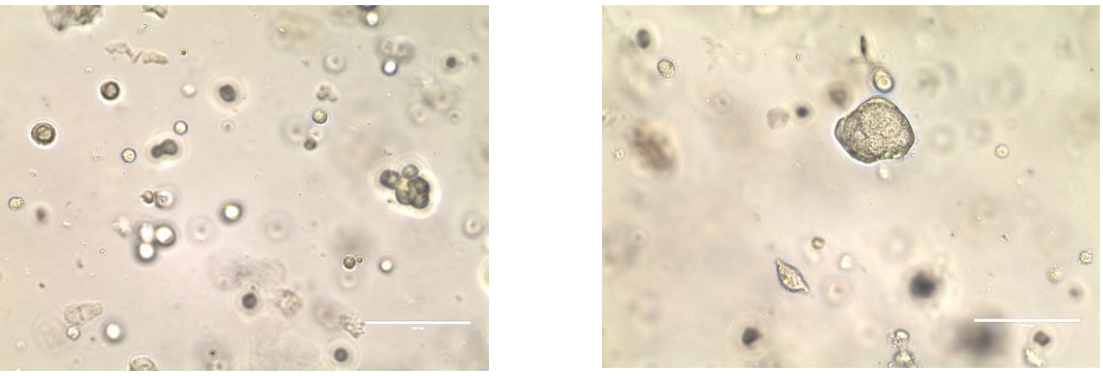

Day 1 (P0)

Day 5 (P0)

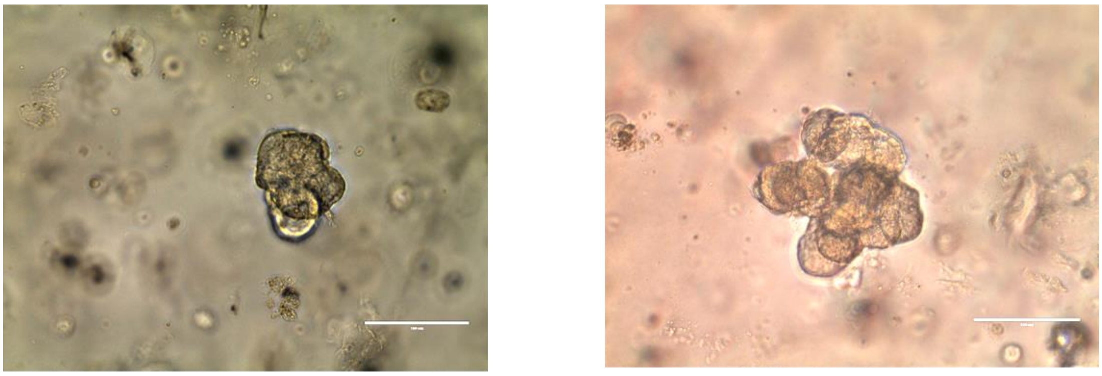

Day 12 (P0)

Day 19 (P0; immediately prior to first passage)

Figure 3.11. Representative images of the ACS-HN14B organoid line captured by Evos digital light microscope before the first passage (P0), after 1, 5, 12 and 19 days in culture. Scale bars = 100 µm

After the first passage, some organoids did re-establish successfully (. On day 24, 5 days after the first passage, the cells observed were mainly single cells, although some early organoids began to appear (

Figure **3.12**). By day 29, however, three distinct cell morphologies began to emerge: clusters of single cells close together, isolated single cells and larger organoids approaching 100 µm in diameter (

Figure **3.12**). The single organoids that had been observed at day 29 continued to grow until day 38, with some organoids exceeding 300 µm, while some of the clustered single cells began to form larger organoids in close proximity to each other (

Figure 3.13). In addition, some isolated single cells were still present. After the second passage, the tumour cells failed to form organoids, with the cells instead remaining as isolated single cells (

Figure 3.14). Consequently, growth of this organoid line was terminated after 70 days in culture.

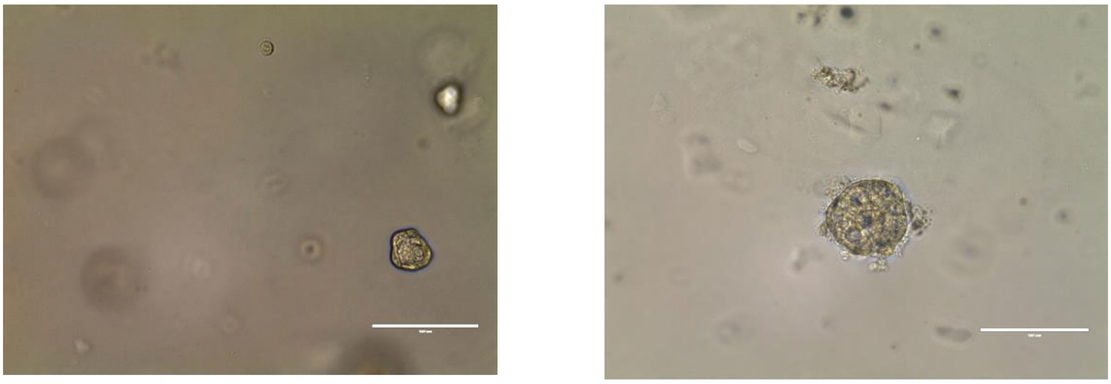

Day 24 (P1)

Day 29 (P1) (Organoids)

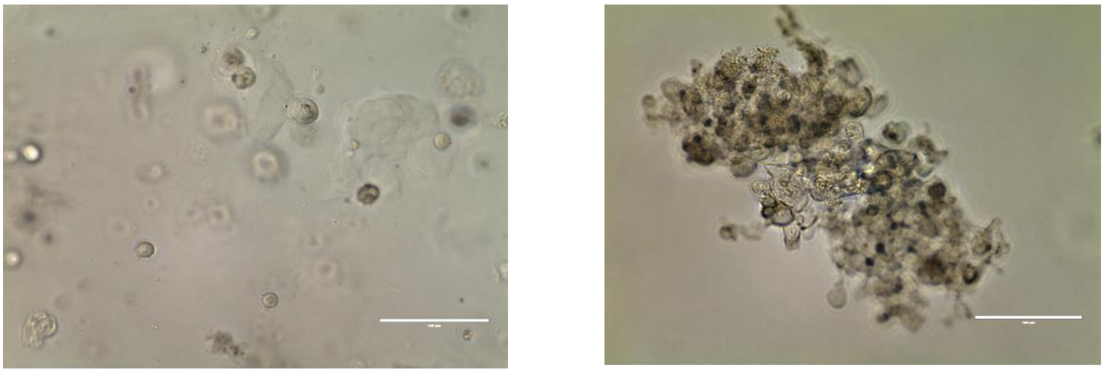

Day 29 (P1) (Separate Single Cells)

Day 29 (P1) (Clustered Single Cells)

Figure 3.12. Representative images of the ACS-HN14B organoid line captured by Evos digital light microscope after the first passage (P1), at day 24 and day 29, with three distinct morphologies (Organoids, Separate Single Cells, Clustered Single Cells) observed at day 29. Scale bars = 100 µm.

Day 38 (P1) (Enlarged Organoids)

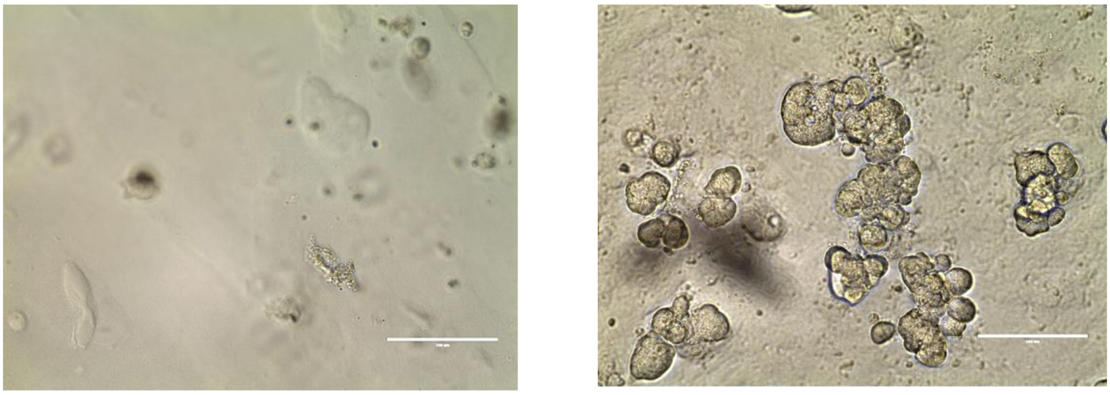

Day 38 (P1) (Separate Single Cells)

Day 38 (P1) (Clustered Organoids)

Figure 3.13. Representative images of the ACS-HN14B organoid line captured by Evos digital light microscope after 38 days in culture and one passage (P1) demonstrating three distinct morphologies (Enlarged Organoids, Separate Single Cells, Clustered Organoids). Scale bars = 100 µm

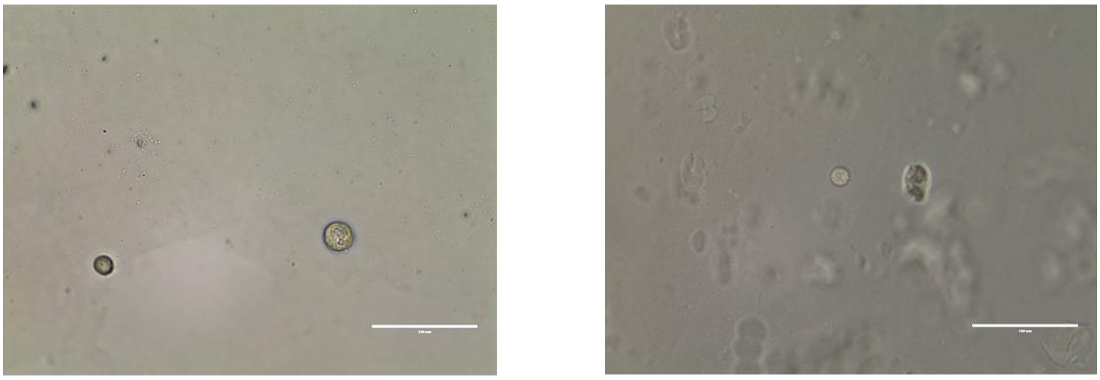

Day 43 (P2)

Day 51 (P2)

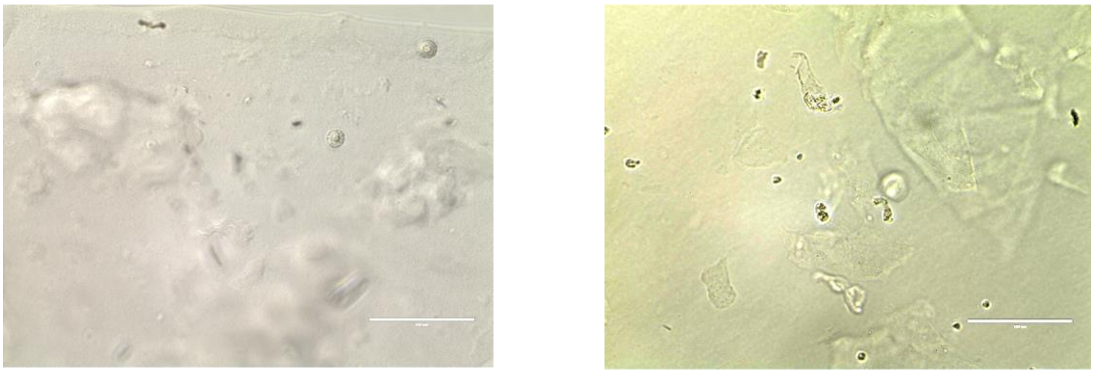

Day 64 (P2)

Day 70 (P2)

Figure 3.14. Representative images of the ACS-HN14B organoid line captured by Evos digital light microscope after the second passage (P2), after 43, 51, 64 and 70 days in culture. Scale bars = 100 µm

3.7.3 ACS-HN14C

A third attempt at growing ACS-HN14 organoids (ACS-HN14C) was carried out from a separate ACS-HN14 PDX tumour. Up until the first passage, ACS-HN14C appeared to demonstrate a very similar growth pattern to ACS-HN14B. Immediately after seeding, separate single cells were the prevailing morphology observed. Some early organoids began to appear after 3 days in culture, with some of these organoids exceeding 100 µm in diameter by day 7. These organoids continued to grow until day 13, with approximately 30% of the established organoids exceeding 200 µm in diameter. Based on these results, the first passage was carried out on day 13. However, after the first passage was carried out, the organoids failed to re-establish, with the corresponding cells remaining as separate single cells, and showed no further signs of growth (

Figure 3.16). Consequently, growth of this organoid line was terminated after 38 days in culture, with no second passage being carried out.

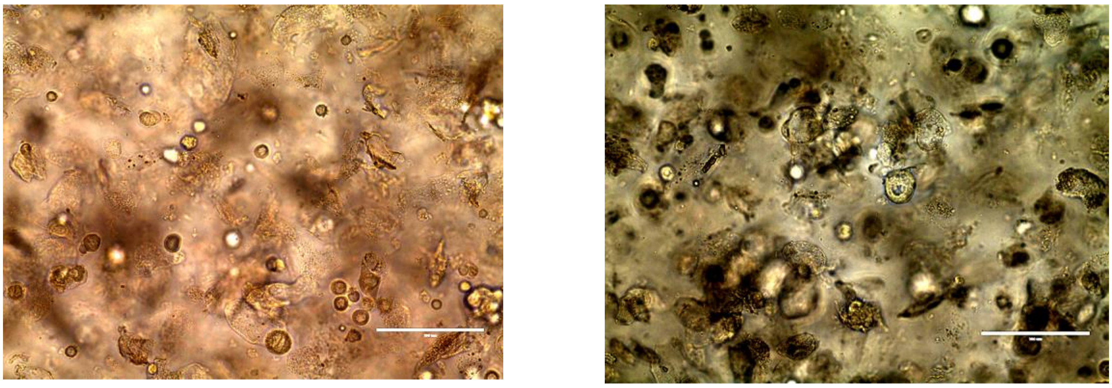

Day 0 (P0)

Day 3 (P0)

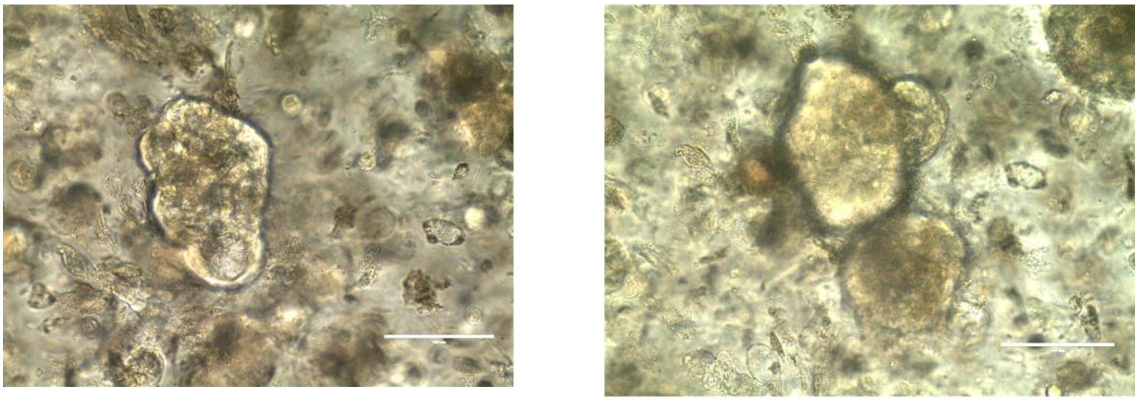

Day 7 (P0)

Day 13 (P0, immediately prior to first passage)

Figure 3.15. Representative images of the ACS-HN14C organoid line captured by Evos digital light microscope immediately after seeding (Day 0), and after 3, 7 and 13 days in culture at passage 0 (P0). Scale bars = 100 µm

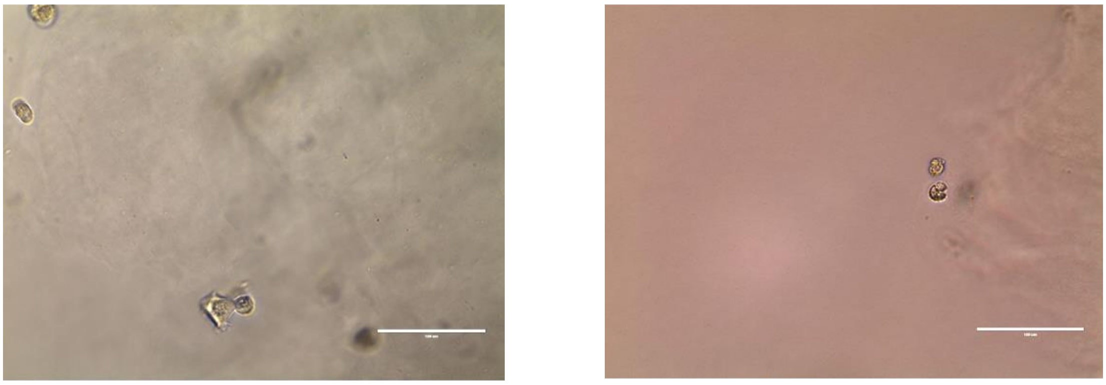

Day 18 (P1) Day 24 (P1)

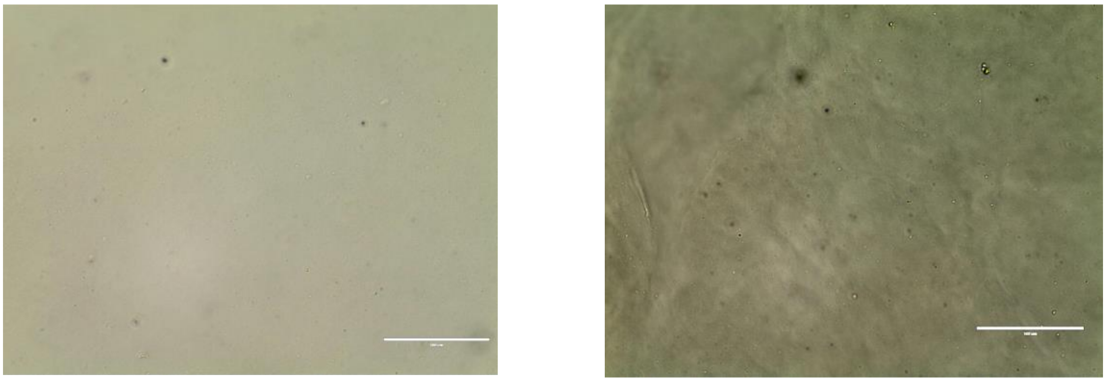

Day 31 (P1) Day 38 (P1)

Figure 3.16. Representative images of the ACS-HN14C organoid line captured by Evos digital light microscope following the first passage (P1), after 18, 24, 31 and 38 days in culture. Scale bars = 100 µm

3.8 ACS-HN18

Two attempts to culture ACS-HN18 PDX-derived organoids were carried out, using two distinct PDX tumours that originated from the same patient primary tumour. These were labelled A and B, which represent the chronological order in which these attempts were carried out.

3.8.1 ACS-HN18A

Like with ACS-HN04, ACS-HN18A tumours showed rapid organoid formation, with organoids exceeding 100 µm appearing after only two days in culture. As can be seen from

Figure 3.17, this rapid organoid growth continued until the first passage, with the number of organoids exceeding 100 µm diameter steadily increasing in number until the first passage, which was carried out on day 10. Organoids successfully re-established 5 days after this first passage, with large organoids beginning to emerge on day 20 (

Figure 3.18). Based on these findings, a second passage of these organoid lines was carried out after 21 days in culture. Organoids reappeared four days later, approaching a diameter of 50 µm. Based on rapid growth after 2 passages, this organoid line was selected for characterisation, with half of the cells in culture at that point being harvested. The remainder were kept in culture for long-term evaluation. However, the observed growth after the second passage appeared to stop after day 30, with the organoid appearing as similar sizes to what was previously recorded, and with existing single cells remaining as such. Consequently, culture for this line was terminated after 43 days in culture (Figure 3.19).

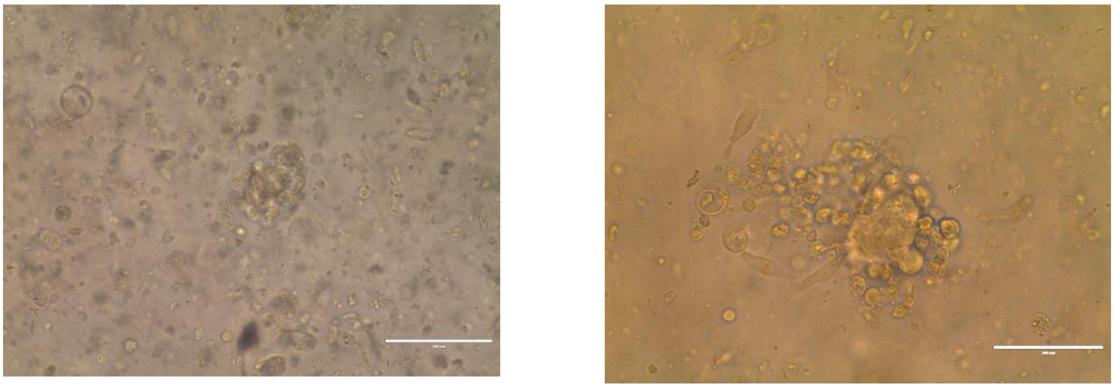

Day 2 (P0)

Day 4 (P0)

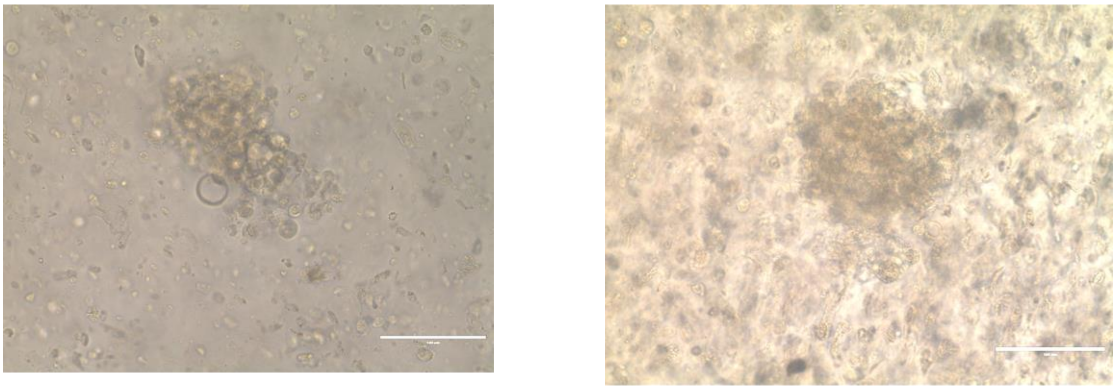

Day 6 (P0)

Day 9 (P0)

Figure 3.17. Representative images of the ACS-HN18A organoid line captured by Evos digital light before the first passage (P0), after 1, 4, 6 and 9 days in culture. Scale bars = 100 µm

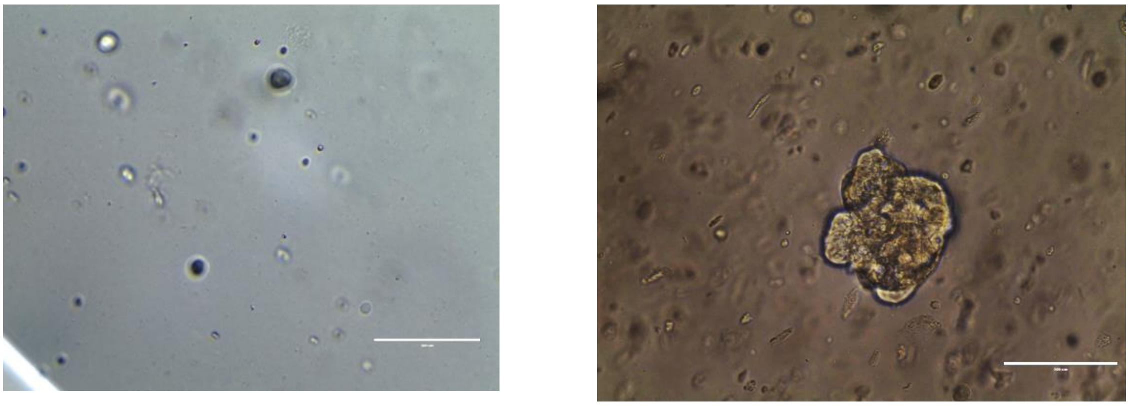

Day 10 (Immediately after P1)

Day 15 (P1)

Day 20 (P1)

Figure 3.18. Representative images of the ACS-HN18A organoid line captured by Evos digital light after the first passage (P1), after 10, 15 and 20 days in culture. Scale bars = 100 µm

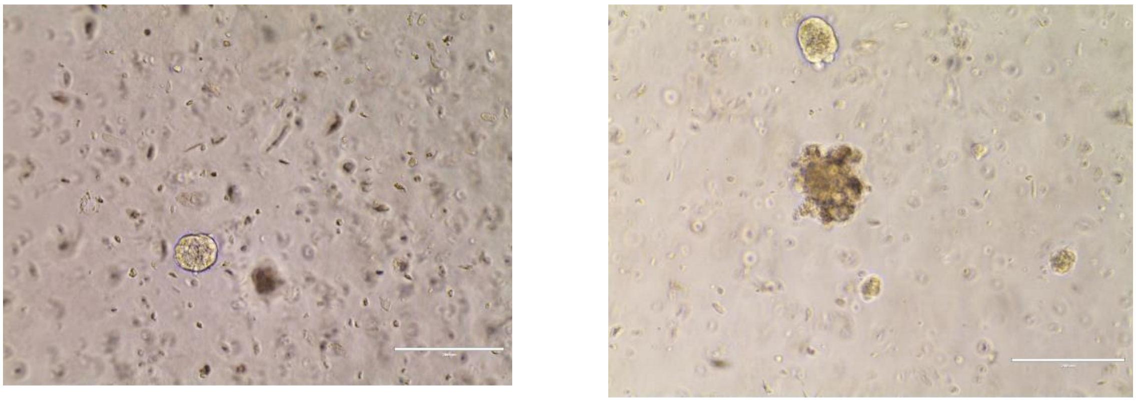

Day 21 (1 day after P2)

Day 24 (P2)

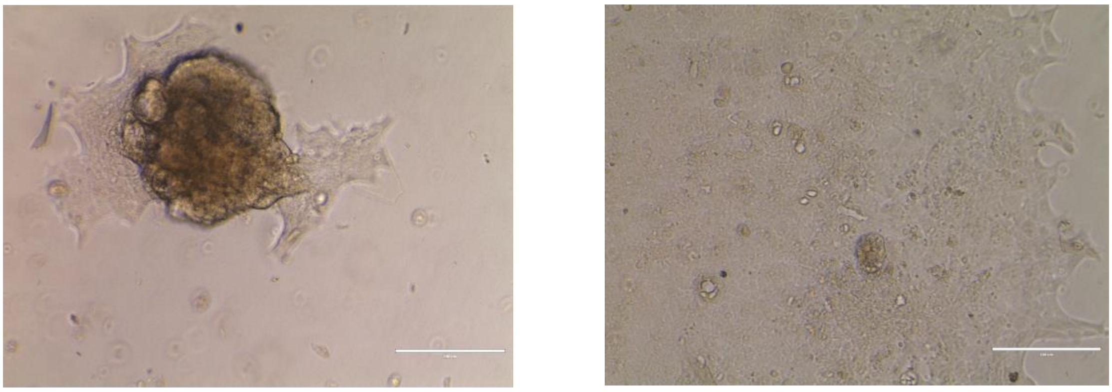

Day 27 (P2)

Day 34 (P2)

Day 43 (P2)

Figure 3.19. Representative images of the ACS-HN18A organoid line captured by Evos digital light after the second passage (P2), after 21, 24, 27, 34 and 43 days in culture. Scale bars = 200 µm

3.8.2 ACS-HN18B

ACS-HN18B PDX tumour cells did successfully form organoids, although the observed growth rate was noticeably slower compared to ACS-HN18A. Immediately after seeding, the

prevailing cell morphology that was observed was isolated single cells. These isolated single cells began to form clusters after 2 days in culture, with these clusters exceeding 100 µm in diameter beginning to form after 7 days in culture. Between day 7 and day 10, these enlarged clusters began to convert into organoids exceeding 100 µm, with cells held together more densely than the earlier cell clusters (Figure 3.20). The successful formation of large organoids within this timeframe allowed for the first passage to be carried out on day 11. Large organoids had re-formed at four days after this first passage (day 15), with some of the organoids already exceeding 100 µm at this point and continuing at this size until the second passage, which was carried out on day 21 (

Figure 3.21). However, while organoids did re-establish 4 days post passage (day 25), considerable cell losses occurred during the second passage, meaning that it was not possible to carry out long-term culture of this organoid line.

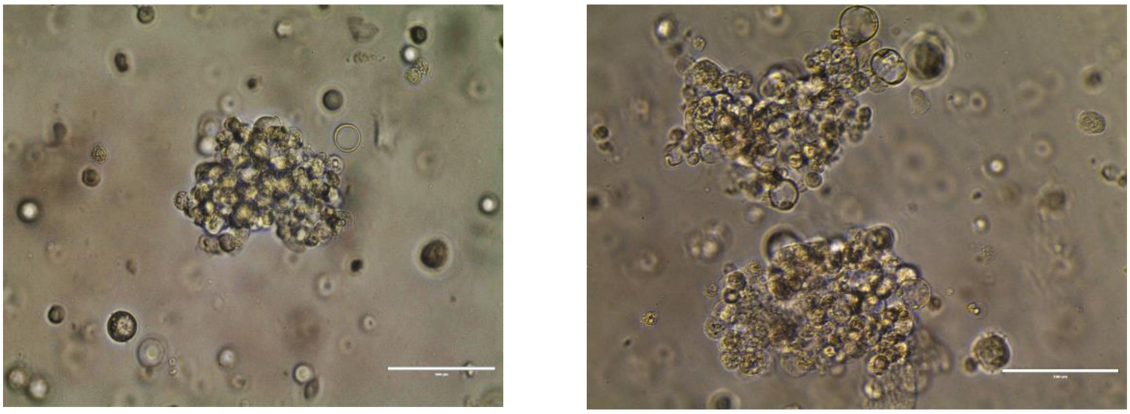

Day 3 (P0)

Day 7 (P0)

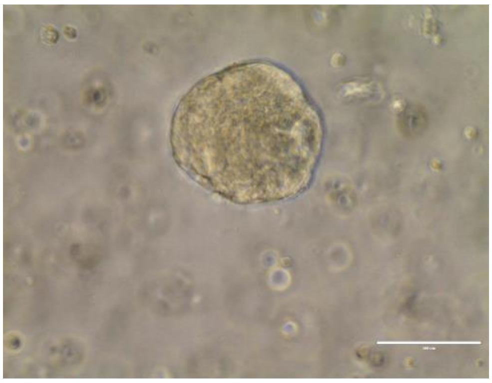

Day 10 (P0)

Figure 3.20. Representative images of the ACS-HN18B organoid line captured by Evos digital light microscope before the first passage (P0), after 3, 7, and 10 days in culture. Scale bars = 100 µm

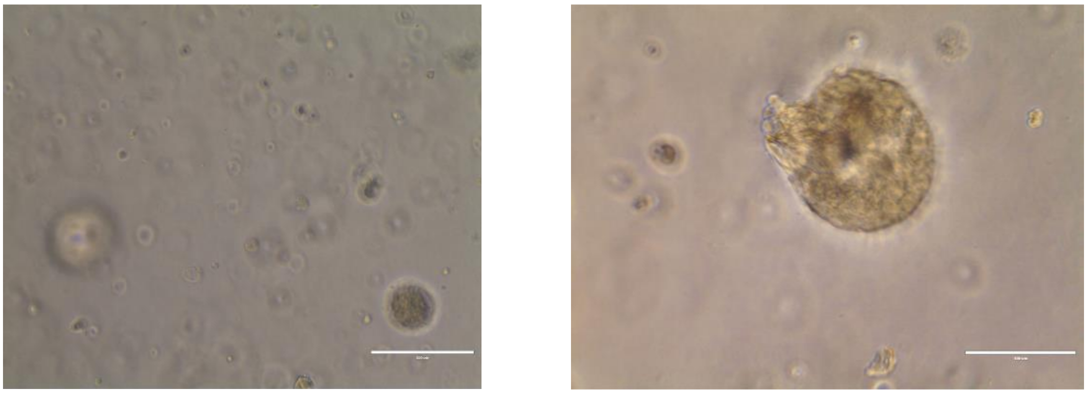

Day 11 (P1) Day 14 (P1)

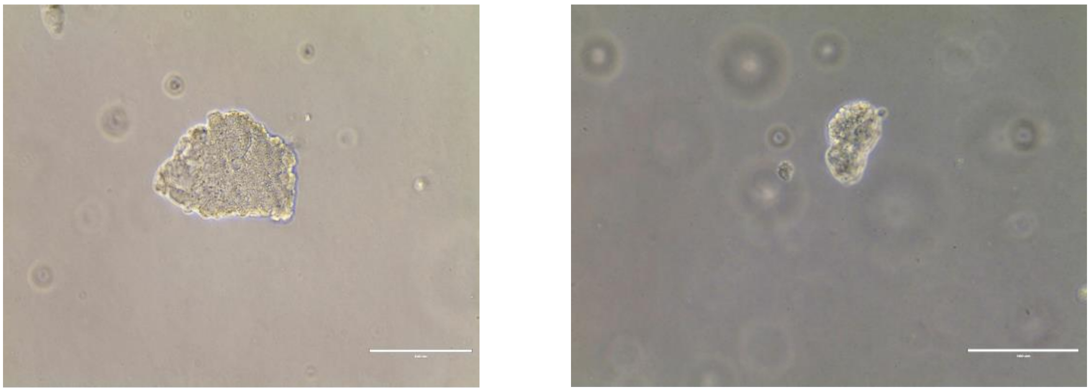

Day 18 (P1) Day 21 (P2)

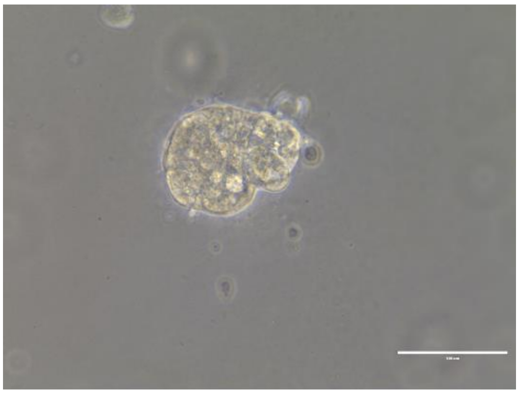

Day 25 (P2)

Figure 3.21. Representative images of the ACS-HN18B organoid line captured by Evos digital light after the first (P1) and second (P2) passages, following 11, 14, 18, 21 and 25 days in culture. Scale bars = 100 µm

3.9 ACS-HN20

Like with the ACS-HN14 and ACS-HN18 tumours, three attempts at establishing organoids from ACS-HN20 PDX tumours were also carried out. These are named A, B and C in chronological order, and represent three distinct tumours grown on three different mice, but are derived from the same patient primary tumour.

3.9.1 ACS-HN20A

ACS-HN20A cells failed to show any signs of growth or establish organoids during the cell culture period (Figure 3.22). Instead, the tumour cells remained as isolated single cells. Consequently, no passaging was attempted on this organoid line, with the cell culture attempt being terminated after 25 days. However, like with the HN14A organoid line that was grown simultaneously with this organoid line, it was later identified shortly after culture termination that seven reagents that comprise the organoid culture medium, (hEGF, hFGF-10, hFGF-2, A83-01, PGE_2, CHIR-99021 and forskolin) were over-diluted by 10-fold relative to their planned concentrations. In addition, considerable fibroblast growth was also visible from Day 6. A sample of these cells were cryogenically frozen at day 25 for subsequent retrieval, although when this was carried out, no organoids were established.

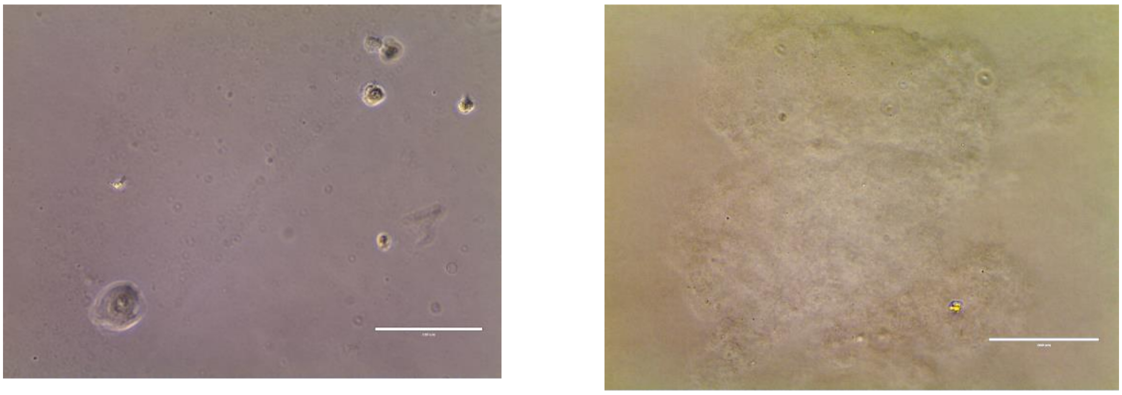

Day 1 (P0)

Day 6 (P0)

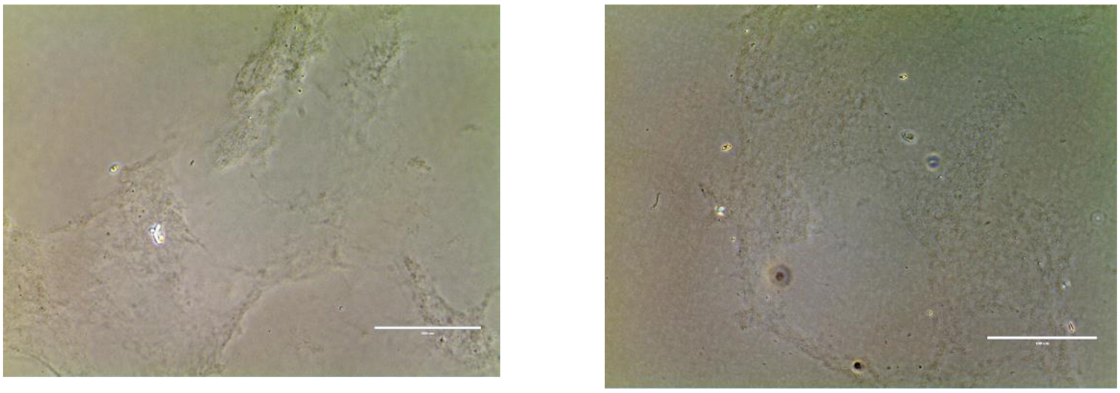

Day 13 (P0)

Day 25 (P0)

Figure 3.22. Representative images of the ACS-HN20A organoid line captured by Evos digital light microscope before the first passage, after 1, 6, 13 and 25 days in culture. Scale bars = 100 µm

3.9.2 ACS-HN20B

ACS-HN20B showed a highly similar growth trajectory compared to ACS-HN14B. Like with ACS-HN14B, this organoid was grown with the correct medium concentrations, which ensured a superior growth rate compared to ACS-HN20A. As can be seen from

Figure 3.23, the prevailing morphology immediately after seeding was isolated single cells. The cells grew steadily from that point, with the first organoids beginning to emerge after 5-7 days in culture. The first large organoids exceeding 100 µm in diameter began to appear after 12 days in culture, with this trend of steady growth continuing until the first passage, which was carried out on day 19.

After the first passage, however, the organoids did not successfully re-establish. Instead, the cells remained as isolated single cells. An attempt was made to re-seed the cells without TrypLE after 64 days in culture. However, this did not result in an improvement in organoid growth rate, with the cells continuing to remain as single cells. Consequently, this culture was terminated after 77 days.

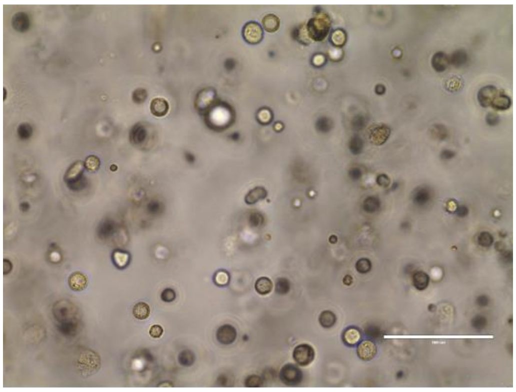

Day 1 (P0)

Day 7 (P0)

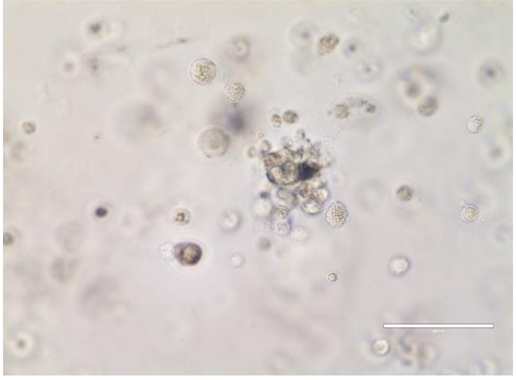

Day 12 (P0)

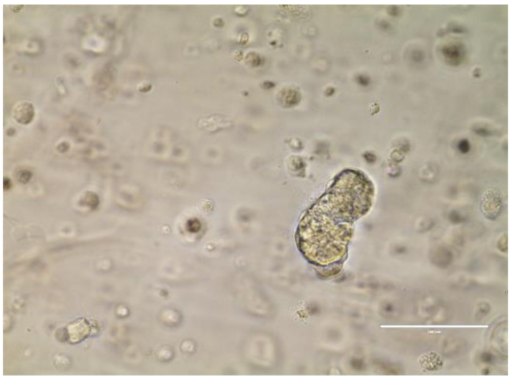

Day 14 (P0)

Day 17 (P0)

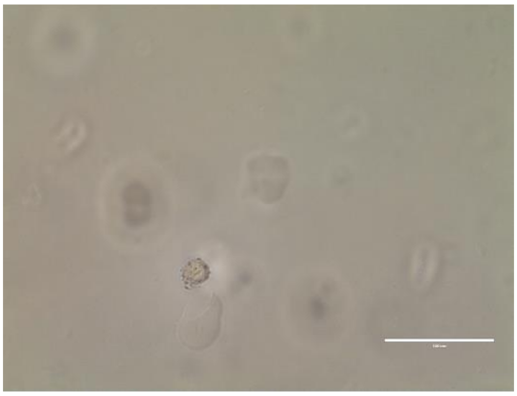

Day 24 (P1, 5 days after passage)

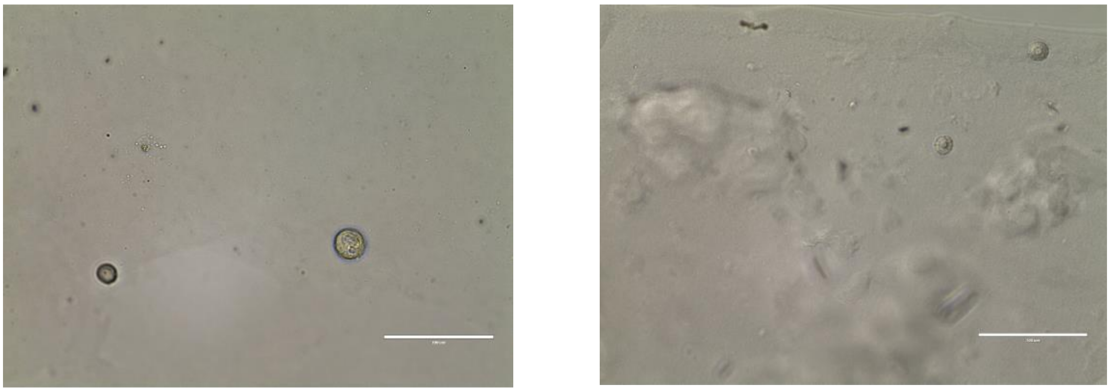

Day 43 (P1, 24 days after passage)

Day 64 (P1, 45 days after P1, re-seed without TrypLE)

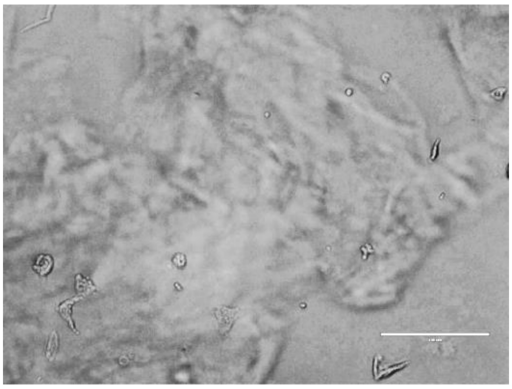

Day 77 (P1, 58 days after P1, 13 days after re-seed without TrypLE)

Figure 3.23. Representative images of the ACS-HN20B organoid line captured by Evos digital light microscope after 1, 7, 12, 14, 17, 24, 43, 64 and 77 days in culture at passage 0 (P0) or 1 (P1). Scale bars = 100 µm

3.9.3 ACS-HN20C

ACS-HN20C showed some organoid growth, although the rate of growth was considerably slower than ACS-HN20B. As can be seen from

Figure 3.24, the ACS-HN20C PDX tumour cells remained as single cells until after 13 days in culture, at which point small organoids of approximately 40 µm in diameter began to emerge. Beyond this point, further organoid growth appeared to cease, with the majority of cells remaining as single cells. Consequently, no passages were carried out on this organoid line, with culture being terminated after 29 days.

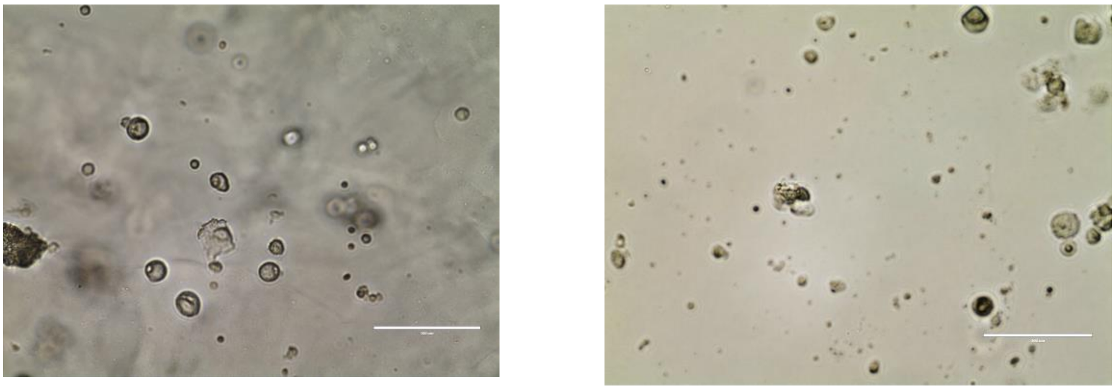

Day 1 (P0)

Day 7 (P0)

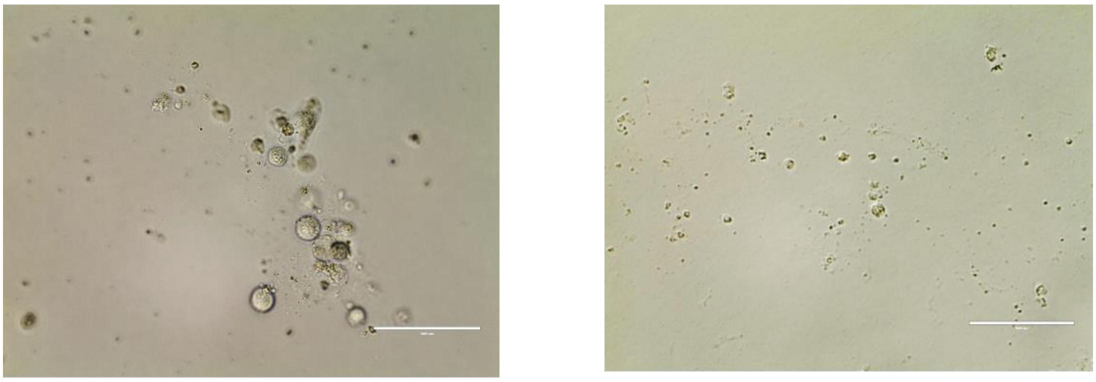

Day 13 (P0)

Day 29 (P0)

Figure 3.24. Representative images of the ACS-HN20C organoid line captured by Evos digital light microscope at passage 0 (P0), after 1, 7, 13 and 29 days in culture. Scale bars = 100 µm

3.10 ACS-HN23

A single attempt was made to grow organoids derived from an ACS-HN23 PDX tumour. For the first 21 days in culture, all of the cells in culture remained as single cells. Some small clusters of cells began to appear after 26 days in culture, although these did not exceed 30 µm in diameter. By day 32, these clusters had grown to approximately 50 µm diameter. However, this cluster formation did not result in organoid formation. Instead, the cell morphology appeared to remain static after 32 days in culture, with no further cell growth being observed. As a result, no passages were carried out on this cell culture, with cell culture being terminated after 59 days.

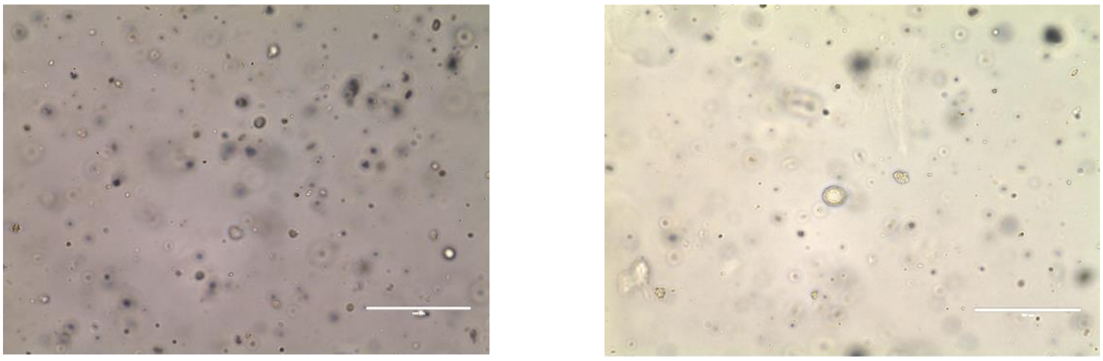

Day 0 (P0)

Day 7 (P0)

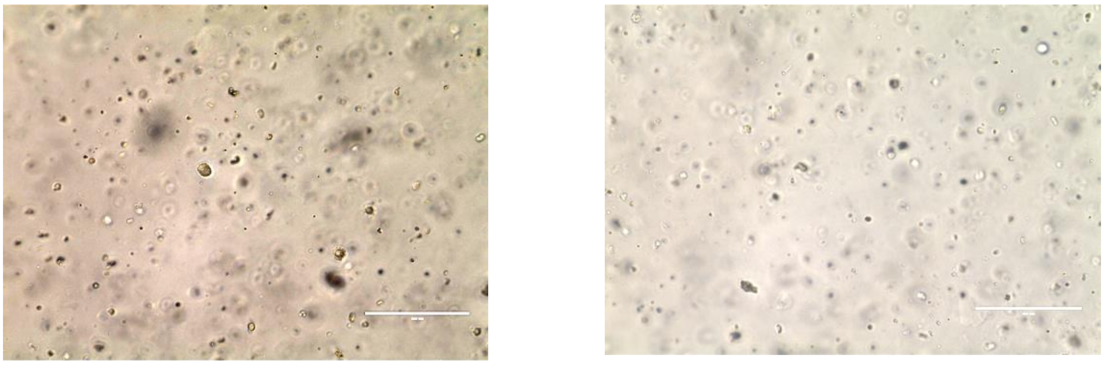

Day 13 (P0)

Day 18 (P0)

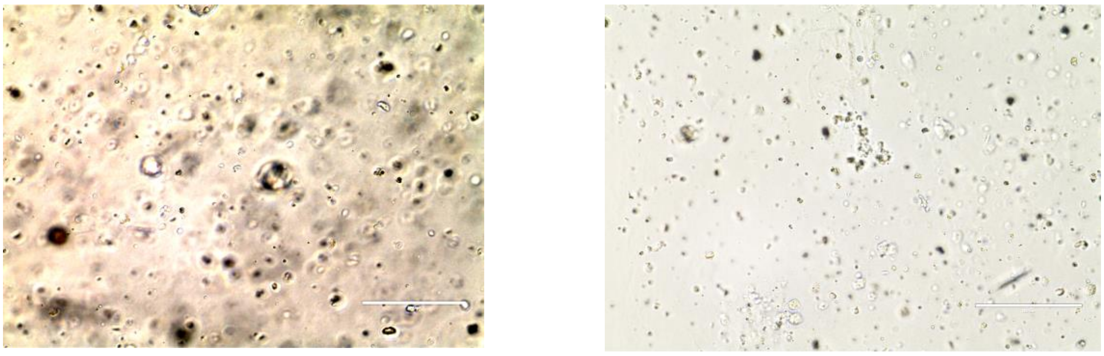

Day 26 (P0)

Day 32 (P0)

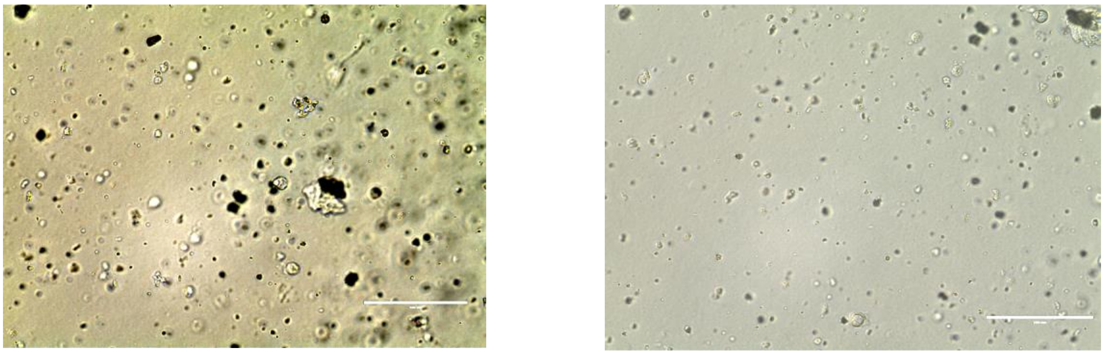

Day 46 (P0)

Day 59 (P0)

Figure 3.25. Representative images of the ACS-HN23 organoid line captured by Evos digital light microscope immediately after seeding (Day 0), 7, 13, 18, 26, 32, 46 and 59 days in culture at passage 0 (P0). Scale bars = 100 µm

3.11 Discussion

HNSCC PDX tumours were minced into small fragments, split into single cells and seeded into a culture plate in order to generate and perpetuate large numbers of organoids for subsequent characterisation. Initially, attempts were made to establish long-term cultures of at least five passages, prior to utilising these organoids in the planned downstream experiments, as this approach was utilised successfully by Driehuis et al (2019) for patient-derived HNSCC organoids. However, although organoids from 10 of the 14 PDX tumours successfully grew up to their first passage (representing a take rate of 71.4%), only 5 (35.7%) of these organoid models re-established after their second passage. No organoid model survived beyond the third passage. As such, the take rate for these organoid models does outperform that reported by Tanaka et al (2018) until the first passage (37.2%), while only 7% of their organoids survived beyond the second passage. However, the take rates observed in this project are still in stark contrast with those reported by Driehuis et al (2019), who reported a successful organoid establishment rate of 65% across 15 passages.

In the initial long-term culture approach, passage timing was determined using a size-based criterion of approximately 30% of observable organoids reaching 150 µm, based on what was implemented by Li et al (2021b) for patient-derived adenocarcinoma organoids. This approach was utilised for the ACS-HN06, ACS-HN08, ACS-HN11, ACS-HN14 (A-C) and ACS-HN20 (A-C) organoid models. Given that none of the organoid cultures survived beyond three passages, it was necessary to optimise the organoid culture protocol for maximal short-term growth up to two passages in order to have sufficient cellular material for the planned downstream experiments. To do this, the growth of subsequent cultures was actively monitored by brightfield microscope imaging, in order to determine the ideal timing for the first and second passages. It was observed that if organoids successfully formed within 7 days of seeding, passaging these organoids after 10-12 days in culture was likely to result in successful regrowth after the first passage. This trend was observed with the ACS-HN04, ACS-HN09, ACS-HN18A and ACS-HN18B cultures, which all subsequently showed organoid re-establishment after two passages and were successfully used in the downstream experiments. Furthermore, this timing period for the first two passages was consistent with the culture protocol developed by Driehuis and colleagues, who carried out passages on their patient-derived organoid models for HNSCC every 7-14 days (Driehuis et al., 2019; 2020).

Although the organoid growth conditions used throughout this project closely reflected that used by Driehuis et al (2019), there were key differences that may have affected organoid growth. Due to the excessive cost of adding recombinant Wnt, R-spondin and Noggin proteins as separate reagents at set concentrations into the organoid culture medium as carried out by Driehuis et al (2019), conditioned media from L-WRN cells was added instead. L-WRN cells are fibroblast-like cells that can be used to secrete Wnt, R-spondin and Noggin proteins into their culture medium, thereby allowing this medium to be added to organoid cultures as a solution containing all three of these proteins (VanDussen et al., 2019). However, it has been identified that considerable batch-to-batch variability exists with respect to their secretion into the medium (Zheng et al., 2021). Given the role of these proteins in driving EMT and stem cell proliferation in organoid cultures, it is possible that any deficiency in these proteins could have stymied stem cell growth and proliferation within the organoids, thereby leading to stem cells being selected against in culture (Urbischek et al., 2019). Indeed, the organoid medium used by Tanaka et al (2018) did not contain any of these three proteins, and thus may have contributed to their low reported organoid survival rates after two passages (7%). Furthermore, it is possible that the squamous epithelial cells within each organoid were entering a stage of senescence after approximately 30 days in culture. Thus, the lack of successful establishment of long-term organoid cultures could be due to the cumulative effect of senescent epithelial cells and a lack of available stem cells available to differentiate and replace the senescent epithelial cells. Taken together, these findings suggest that while the organoid culture protocols used in this project can be utilised to generate organoid tissue for characterisation following short-term tissue culture, further optimisation of both the timing of the organoid passages and the composition of the organoid medium is required to successfully perpetuate the PDX-derived HNSCC organoid cultures in the longer term.

In addition to optimising the timing of organoid passages for short-term organoid growth, it was also necessary to determine the ideal stage in culture that organoids were to be harvested for the downstream experiments. Rapid organoid re-establishment was observed after the first passage with the ACS-HN04, ACS-HN09, ACS-HN18A and ACS-HN18B organoid lines, beginning 2-3 days post-passage with organoids approaching 100 µm visible 4-5 days post first passage. This implies that after the first passage, these organoid models undergo an initial lag phase of growth lasting 1-2 days, which is followed by an exponential phase of growth leading up to and including 6 days post-passage. This is in stark contrast to patient-derived HNSCC organoids, which observed continual exponential growth across their culture period (Driehuis et al., 2019). Indeed, additional organoid research has identified exponential growth as a necessary condition to ensure rapid organoid re-establishment following transfer to the assay plate (Driehuis et al., 2019; Jacquemin et al., 2022). On this basis, 6 days after the first passage was chosen as the time-point for organoid harvesting for experiments in Chapters 4 and 6, which ensured that there were sufficient numbers of large organoids to harvest as well as allowing for the differentiation of cells within each organoid. Upon closer inspection, the ACS-HN11 organoids showed a similar growth pattern after their first passage; thus, it is likely that had organoids have been harvested at this time-point, there would have been suitable numbers for downstream evaluation.

A similar trend in the ACS-HN04, ACS-HN09, ACS-HN18A and ACS-HN18B organoid lines was observed following the second passage compared to after the first; an initial lag phase of 2 days followed by an exponential phase up to and including 4 days post-passage. This approach to the timing of organoid RNA extraction has been utilised with other PDX-derived organoid models, as it was identified in those models that overall gene expression is elevated in the exponential phase compared to the lag phase (Guillen et al., 2022; Huang et al., 2020). Finally, as some organoid models such as ACS-HN09 showed evidence of mouse fibroblast growth alongside the tumour cells after initial seeding, it was necessary to remove these by passaging the cells prior to any experimentation being carried out. Given these findings, 4 days after the second passage was chosen as the time-point for organoid harvesting for gene expression analysis..

Cryogenic freezing as per Section 2.2.4 was carried out on four different organoid limes as part of this project (ACS-HN04, ACS-HN06, ACS-HN09 and ACS-HN20A). The timing of this cryogenic freezing differed between each organoid line, which enables comparison of how the success of organoid cryopreservation and revival varied with length of time in culture. ACS-HN04 was cryogenically frozen on Day 16 (4 days after the first passage), ACS-HN06 on Day 30 (18 days after the first passage), ACS-HN09 on Day 14 (3 days after the first passage), and ACS-HN20A on Day 25 (no passages carried out). ACS-HN04 and ACS-HN09 organoids were successfully re-established after being revived and re-seeded into a 24-well culture plate, while ACS-HN06 and ACS-HN20A remained as single cells (see Section 3.3 and 3.9.1). However, in the lines that successfully re-established organoids, there was still a considerable reduction in the overall number of viable cells post-revival. Additionally, the low retrieval rates observed with ACS-HN04 and ACS-HN09 also limited the supply of cells available for experimentation, as well as further contributing to the inability to establish long-term cultures of these organoid lines. As such, further optimisation of the protocol to cryogenically freeze organoids is required in order to improve retrieval rates. These optimisation steps could include further reductions of the time the organoids spend in culture prior to cryopreservation, as well as experimenting with different organoid freezing medium compositions.

4 Histology and Hypoxic Characterisation of PDX-derived HNSCC Organoids

4.1 Introduction

In order to confirm that the organoids recapitulated the squamous cell carcinoma (SCC) morphology of the PDX models they were derived from and to evaluate their hypoxia status, two sets of histological stains were carried out: haematoxylin and eosin (H+E), as well as pimonidazole staining.

H+E staining has been widely used in histopathological analyses to distinguish between different cell types within a tissue sample (Fischer et al., 2008). Indeed, this approach has successfully been utilised in the characterisation of cell and tissue arrangement for patient-derived organoid models for multiple different cancer types, with these characterisations showing that the organoids had a high level of morphological similarity to the primary tumours they were derived from (Boj et al., 2015; Driehuis et al., 2019; Xie & Wu., 2016). Additionally, more recent research has identified a similar trend between PDX-derived organoid models and the original PDX tumour (Aizawa et al., 2022; Guillen et al., 2022; Kaushik et al., 2021). In each of these cases, the morphological similarities included the size and shape of the nuclei within the organoids relative to the source tissue, as well as the overall arrangement of the cells.

Tumour hypoxia has been implicated as a major driver of HNSCC progression and has been shown to be present in PDX models of HNSCC previously developed by the ACSRC (Harms et al., 2019). In these PDX models, combination nuclear and pimonidazole fluorescent staining was carried out to determine which regions within the PDX tumour demonstrated tumour necrosis and hypoxia. This approach did successfully distinguish between normoxic and hypoxic tumour regions, with the hypoxic regions being indicated by bright green fluorescence (Harms et al., 2019). Therefore, to determine whether hypoxia was present in the PDX-derived organoid models, the same staining technique was applied to the organoids as part of this project. Pimonidazole staining has successfully been implemented for organoid models from a wide range of other cancer types, including pancreatic, gastrointestinal and non-small cell lung carcinomas (Fanchon et al., 2020; Yamasaki et al., 2022; Ziolkowska-Suchanek, 2021).

4.2 Protocol Development

4.2.1 Organoid Tissue Processing

As PDX-derived organoids for HNSCC have not been previously developed, there was no previously published protocol for harvesting and processing these organoids in preparation for staining. Therefore, it was necessary to first establish a protocol for harvesting and processing organoids prior to carrying out the downstream staining. To do this, the protocol for organoid harvesting and processing used by Li et al (2021b) for patient-derived lung adenocarcinoma organoids was used as a starting point, from which further optimisations were made in order to arrive at the optimised organoid harvesting and processing protocol described in Section 2.3.3.

Initially, attempts were made to harvest ACS-HN04 organoids directly by scraping the BME domes from the cell culture plate and transferring to a 15 mL Falcon tube, as carried out by Li et al (2021b). However, the BME domes collapsed, which led to a complete loss of the cell sample to be processed and so staining could not be carried out. In order to prevent further losses in subsequent attempts, this harvesting technique was replaced with an indirect harvesting technique, in which the organoid medium was replaced with a fresh medium containing 1 mg/mL Dispase II, with the cells being allowed to incubate at 37 ^{0}C for 40 min. The addition of Dispase II facilitated the dissolution of the BME domes, while ensuring that the structural integrity of the organoids contained within was preserved (Driehuis et al., 2020).

While Dispase II treatment minimised cell losses due to harvesting, some downstream processing steps had also been identified as exacerbating cell losses. After harvesting, the organoids were fixed using 10% neutral-buffered formalin (NBF) for 2 h and washed with PBS, prior to 2% agarose being added directly to the Falcon tube. However, the agarose solidified prematurely inside the tube, requiring the tube to be scraped manually to retrieve the agarose block. When staining was attempted on this sample, no organoids had transferred successfully to the slides, with only isolated single cells visible. This implied that not only did organoid losses occur, but that those organoids that did transfer successfully to the slide had degraded considerably. As a result, two key optimisations were implemented for further staining attempts. Firstly, to minimise the degradation of the organoid samples post-harvesting, the incubation time in 10% NBF was increased to 24 h. Secondly, instead of adding the 2% agarose directly to the 15 mL Falcon tube, pre-heated agarose was added to a clear plastic histology mould, with the organoids being mixed with the liquid agarose inside the mould, before being placed on ice to solidify and form a dome. This enabled the plastic mould to be peeled from the dome, prior to paraffin embedding and allowed the organoids to be successfully transferred to microscope slides and staining to be carried out.

4.2.2 Haematoxylin Substitution

In the first H+E staining attempt, ACS-HN04 organoid samples were stained with Gill II haematoxylin to highlight the locations of individual cell nuclei within the organoid structure. However, while some individual cell nuclei were visible, they could not be clearly distinguished from the surrounding cell cytoplasm (

Figure 4.1). To address this, Gill II haematoxylin was substituted for CAT haematoxylin to ensure darker staining of cell nuclei for all subsequent H+E organoid stains carried out as part of this project.

Figure 4.1 Representative image of the ACS-HN04 organoid line stained with Gill II haematoxylin for H+E staining, captured by Zeiss Axio Imager M2 digital phase contrast microscope. Scale bar = 20 µm.

4.3 Haematoxylin and Eosin Staining

H+E staining was done on ACS-HN04, ACS-HN09, ACS-HN18A and ACS-HN18B organoids 6 days after the first passage. For the other organoid lines, it was planned for them to undergo five passages prior to being harvested for histological processing. As none of these organoid lines survived beyond three passages, it was not possible to carry out staining on any of them.

While squamous cells were present in both the ACS-HN04 PDX and PDX-derived organoids (Figure 4.2), considerable differences in the observed morphologies exist. The nuclei present are inconsistent in size, with the organoid sample in Figure 4.2B showing an enlarged cell nucleus near the centre of the organoid, surrounded by smaller nuclei closer to the periphery. In contrast, the nuclei observed in the ACS-HN04 PDX tumour are more uniform in size. Additionally, while the cells are relatively densely packed within the ACS-HN04 organoids, the PDX tumour shows regions of densely packed cells, interspersed with more loosely-packed cells amid regions of keratinisation that appear a lighter shade of pink compared to the surrounding tissue. No regions of keratinisation were obvious in the corresponding ACS-HN04 organoids. Immediately beside the ACS-HN04 organoid samples on the microscope slides, there appeared to be blank, agarose-free lacunae that although larger than the organoids, shared a similar overall shape (Figure 4.2A and B). Indeed, the ACS-HN04 organoids that stained successfully appeared to show a relatively small overall diameter, rarely exceeding 50 µm.

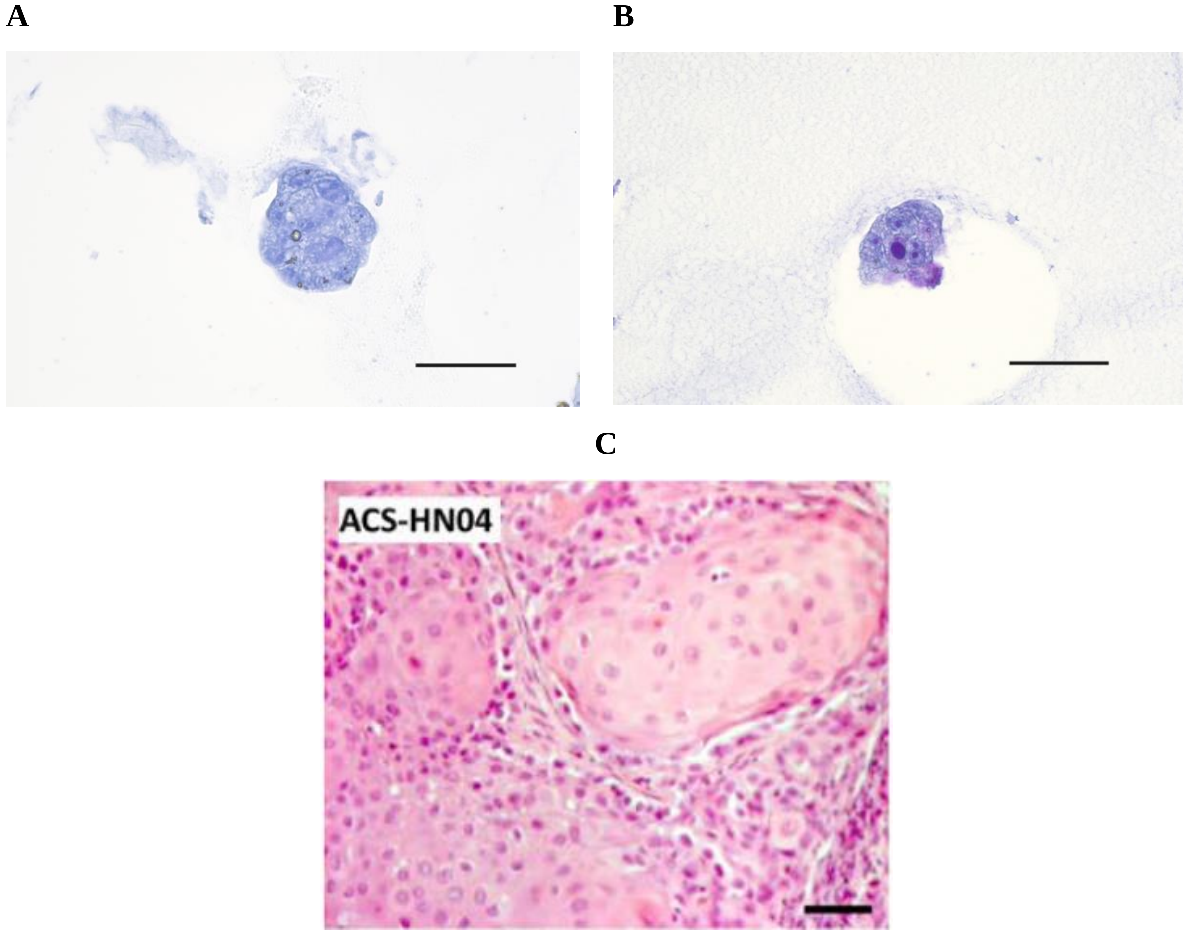

Figure 4.2. Representative H+E images of ACS-HN04 organoid models (A and B), obtained 6 days after the first passage. The Zeiss Axio Imager M2 was utilised to capture brightfield images of the organoid slices. C is a representative image of the matched PDX tumour, obtained by Harms et al (2019). Scale bars = 50 µm for all panels.

Meanwhile, the ACS-HN09 organoids showed a much higher level of morphological similarity to their corresponding PDX tumour. Unlike the ACS-HN04 organoids, the ACS-HN09 organoids contain nuclei of a relatively similar size throughout, with an average diameter of approximately 5 µm. The ACS-HN09 organoids do appear to possess some small regions of keratinisation, as can be observed by the pink shading present in Figure 4.3. Additionally, the ACS-HN09 PDX tumour cells appear to be more densely packed across the whole tumour sample, appearing to have a relatively low level of keratinisation compared to the ACS-HN04 PDX tumour. The ACS-HN09 organoids that stained had a larger size than the ACS-HN04 organoids, although lacunae were still present surrounding some organoids (e.g.

Figure 4.3A).

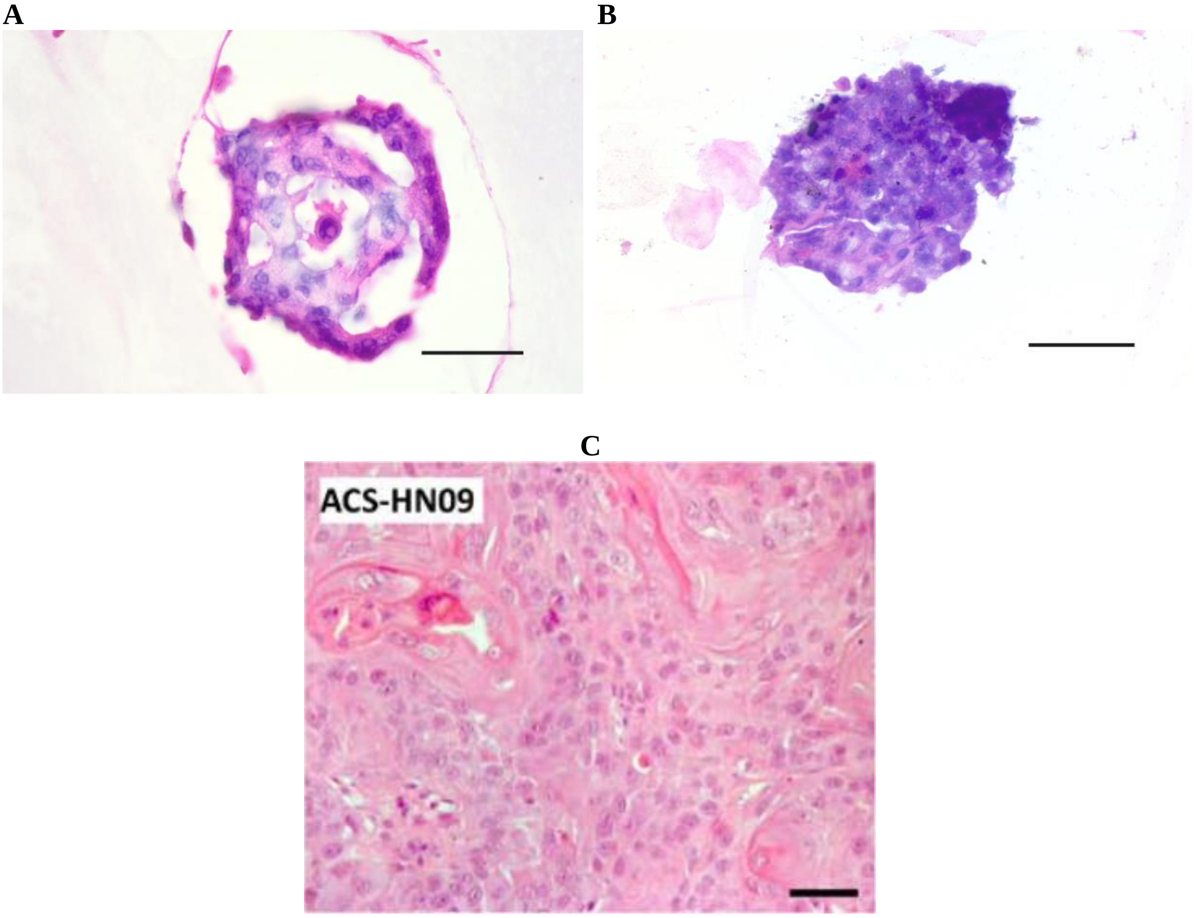

Figure 4.3. Representative H+E images of ACS-HN09 organoid models (A and B) , obtained 6 days after the first passage. The Zeiss Axio Imager M2 was utilised to capture brightfield images of the organoid slices. (C), a representative image of the matched PDX tumour, obtained by Harms et al (2019) Scale bars = 50 µm for all panels.

When compared to each other, the ACS-HN18A and ACS-HN18B organoids show two very distinct cell morphologies. While similar in overall diameter, the ACS-HN18A organoids possess a more rounded shape with smoother edges, compared to the rougher edges present in the ACS-HN18B organoids. Despite the individual cells within ACS-HN18A and ACS-HN18B organoids appearing to be similarly densely packed, the nuclei within the ACS-HN18A organoids appear to be considerably larger in diameter (5-6 µm for ACS-HN18A compared to 2-3 µm for ACS-HN18B, Figure 4.4). Additionally, the ACS-HN18A organoids show the most extensive keratinisation out of all the organoid models, which can be demonstrated by the sizeable light pink region observed in the centre of the ACS-HN18A organoid in Figure 4.4. In contrast, the ACS-HN18B organoids did not appear to show any regions of keratinisation. The

ACS-HN18A and ACS-HN18B organoid lines did not show any signs of lacunae and were of similar size to the ACS-HN09 organoids. As no H+E images have been previously captured for the ACS-HN18 PDX tumours, it was not possible to directly compare these organoids to their PDX tumours.

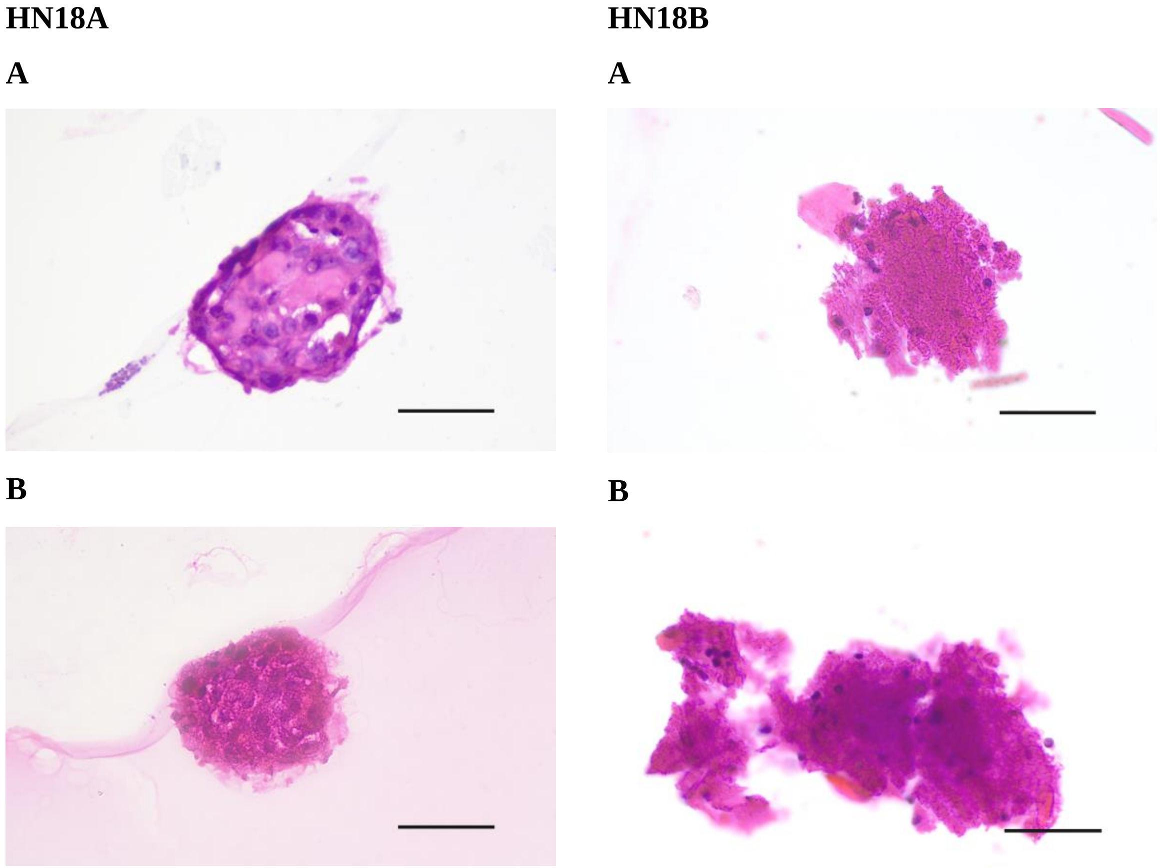

Figure 4.4. Representative H+E images of ACS-HN18A and ACS-HN18B PDX-derived organoid models, obtained 6 days after the first passage. Image capture was carried out using the Zeiss Axio Imager M2. Scale bars = 50 µm.

4.4 Pimonidazole Staining

Pimonidazole staining was carried out on 2 different organoid lines (ACS-HN04 and ACS-HN18A), with HCT116 being utilised as both a positive control (when stained with Hoechst 33342 and pimonidazole) and a negative control (stained with Hoechst 33342 alone). The HCT116 spheroids had a diameter of approximately 400 µm and showed key morphological characteristics indicative of tumour hypoxia (). Firstly, the cells located in the centre of the spheroid showed elevated levels of Hoechst 33342 fluorescence at 385 nm compared to the cells in the periphery. As can be observed in F, the central core was surrounded by a band of cells showing elevated green fluorescence at 470 nm, indicating that the specific antibody-fluorophore conjugate bound successfully to intracellular pimonidazole adducts located within the hypoxic cells. Taken together, these findings suggest the presence of a non-viable core within the spheroids, surrounded by hypoxic live cells, with viable non-hypoxic cells visible on the outer edges.

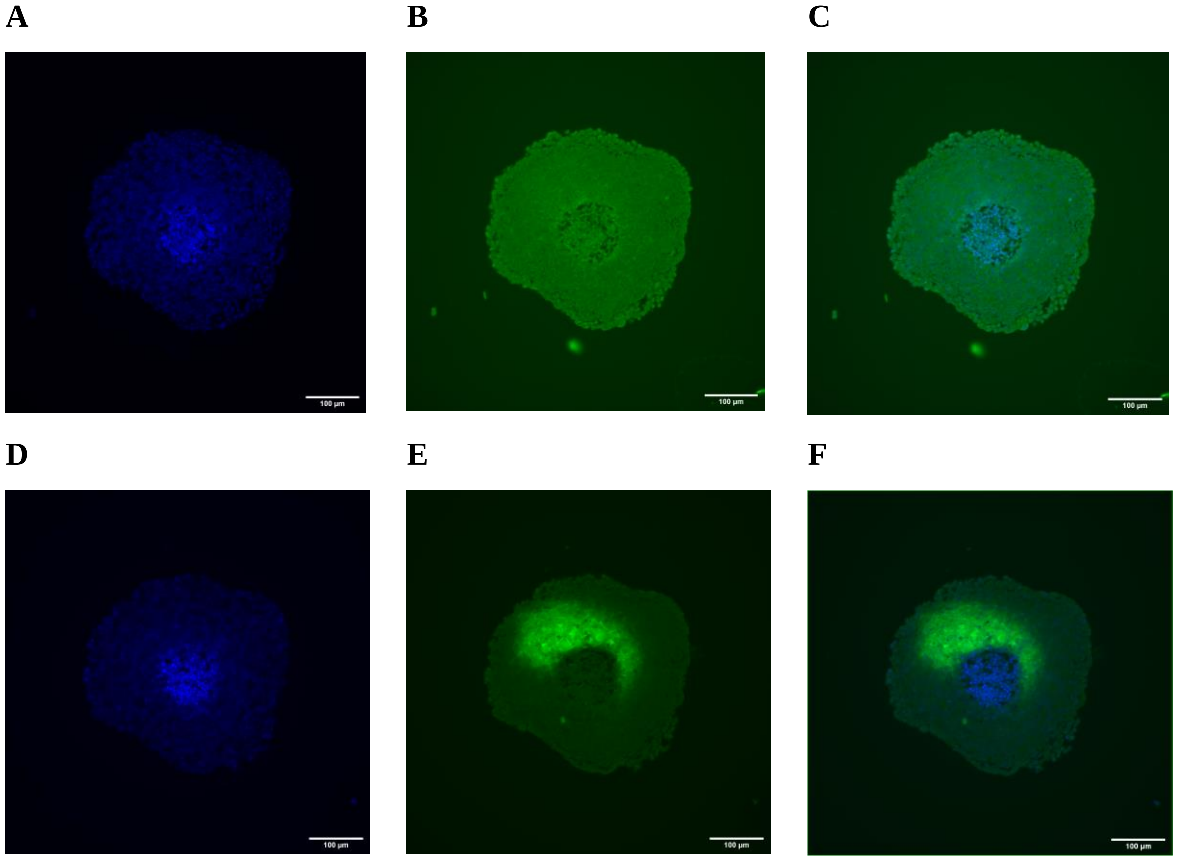

Figure 4.5. Representative immunohistochemistry fluorescent images captured at 385 (A,D) and 470 nm (B,E) for HCT116 spheroids, treated with Hoechst 33342 staining alone (A-C) or with Hoechst 33342 + pimonidazole (D-F), alongside overlays (C,F) of these images. Green, pimonidazole; blue, Hoechst 33342. Scale bars: 100 µm.

The trends observed in the HCT116 spheroids were not observed with the ACS-HN04 (approximately 100 µm diameter) or ACS-HN18A organoids (approximately 200 µm diameter) (Figure 4.6 and Figure 4.7). Instead, the Hoechst 33342 fluorescence at 385 nm was relatively consistent throughout the entire organoid structures, although the ACS-HN04 organoid nuclei were more loosely arranged compared to ACS-HN18A. Furthermore, the pimonidazole staining of these organoids did not show any consistent regions of bright green fluorescence at 470 nm, with the ACS-HN04 organoids showing some bright green fluorescent spots that appear relatively evenly distributed across the whole organoid. Given that these spots were not observed in any other organoid line, it is likely that they emerged due to non-specific binding of the Pimonidazole-FITC antibody. Taken together, these findings potentially indicate a lack of hypoxia present in these organoids.

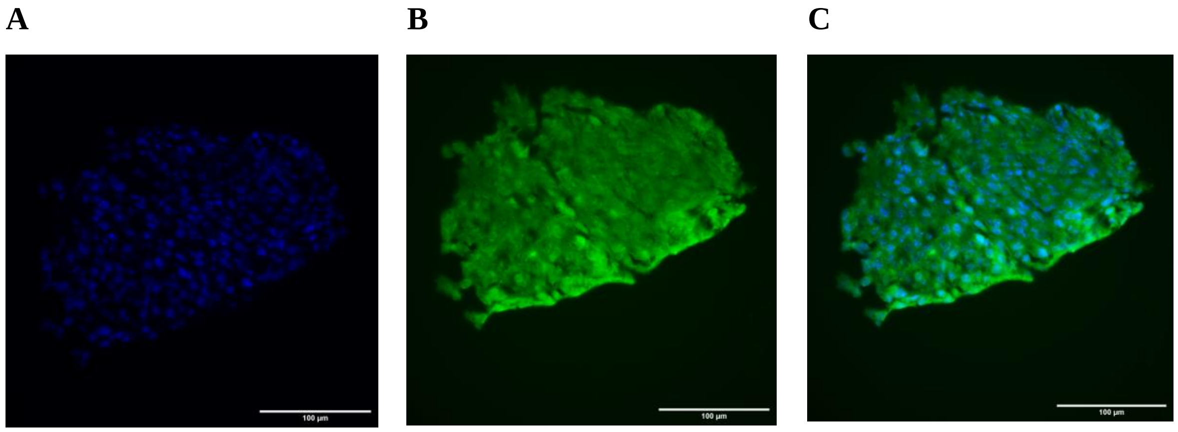

Figure 4.6. Representative immunohistochemistry fluorescent images of ACS-HN18A organoids stained with Hoechst 33342 (A) and pimonidazole (B) combined (C). Scale bars: 100 µm.

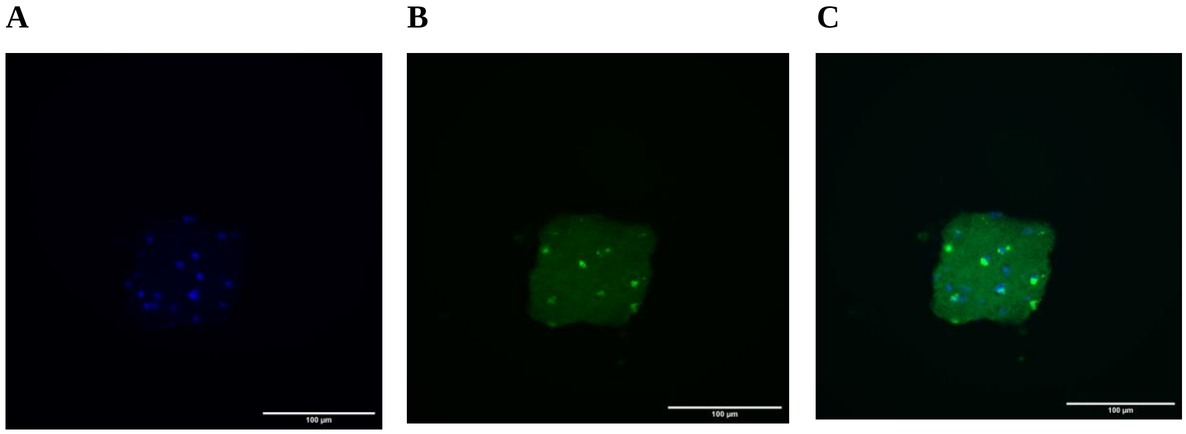

Figure 4.7. Representative immunohistochemistry fluorescent images of ACS-HN04 organoids stained with Hoechst 33342 (A) and pimonidazole (B) combined (C). Scale bars: 100 µm.

4.5 Discussion

H+E staining was carried out across 4 different organoid models generated as part of this project. This enabled direct comparison of two of these models (ACS-HN04 and ACS-HN09) of the tissue cellular composition between these organoid models and the matched PDX tumours generated by Harms et al (2019). As can be observed from Figure 4.2 and Figure 4.4, the organoid models appear to successfully recapitulate the squamous cells present in the PDX tumours. However, no such relationship could be detected with respect to keratinisation. Although the reasons for these differences are not known, it is possible that in the ACS-HN04 organoid line, where no keratinisation appeared to be present, the keratinous cells were selected against during the tissue culture process. Additionally, it is also possible that the keratinous regions in this organoid line and ACS-HN09 broke off from the organoid during histological processing. Furthermore, the inconsistent keratinisation reported in this project contrasts with what was reported with previously-generated HNSCC organoids. For instance, in the H+E stains carried out by Driehuis et al (2019) and Tanaka et al (2018), extensive regions of keratinous tissue were observed in the primary tumour tissue, with these differences successfully recapitulated in the corresponding organoids. However, as ACS-HN18 tumours were not included in the H+E analysis carried out by Harms et al (2019), it is not possible to determine whether either the ACS-HN18A or B organoid models recapitulate the original PDX tumour morphology. Nevertheless, these preliminary findings hint that the organoids generated in this project may not recapitulate their source PDX tumour as closely as those previously reported (Driehuis et al., 2019; Tanaka et al., 2018). However, only two organoid could be compared to their matched PDX tumours; this is not a sufficiently wide variety of organoid models to draw any definitive conclusions regarding their ability to recapitulate the PDX tissue morphology.

As can be observed when staining the ACS-HN04 organoid line (Figure 4.1 and Figure 4.2), the use of CAT haematoxylin yielded a clearer nuclear stain compared to using Gill II haematoxylin. When utilised for H+E staining, haematoxylin is oxidised to hematein, which can form complexes with a mordant, thereby enabling the hematein to bind directly to nuclear DNA, eliciting a blue colour (Kiernan, 2018). However, the two haematoxylin solutions used in this project contained different mordants; while Gill II uses an aluminium sulphate mordant, CAT haematoxylin, a modified Mayer's haematoxylin with acid added, uses an ammonium alum mordant that contains ammonium ions (Kiernan, 2018). Given that a regressive staining technique was utilised where each slide was immersed in haematoxylin stain prior to the excess being washed away, this suggests the presence of the acid and ammonium ions may have increased the selectivity for cell nuclei compared to Gill II haematoxylin. This is in stark contrast to an earlier comparison by Gabriel et al (2021), which determined that Gill II was more readily able than Mayer's haematoxylin to identify nuclei in primary patient tumour of basal cell carcinoma. Taken together, these findings suggest a need to optimise the haematoxylin stain used to each tissue type.

H+E images captured the presence of lacunae adjacent to the ACS-HN04 organoids, as well as the ACS-HN09 organoids to a lesser extent. In contrast, these lacunae were absent in the ACS-HN18A and ACS-HN18B images. Although the cause of these lacunae is not known, their rounded shape may indicate that part of the organoid samples may have broken off while these samples were being processed for staining. This implies that organoid breakage may have occurred for the ACS-HN04 and some ACS-HN09 organoids during the embedding of the 2% agarose block into paraffin in preparation for the transfer of organoid sections to microscope slides. The brightfield images of organoids in culture (see Sections 3.2 and 3.5) indicate that the individual cells within the ACS-HN04 and ACS-HN09 organoids were more loosely packed compared to ACS-HN18A and ACS-HN18B, and is further reinforced by comparing the Hoechst 33342 images between ACS-HN04 and ACS-HN18A. This looser arrangement may make ACS-HN04 and ACS-HN09 organoids more susceptible to breakage during paraffin embedding and perhaps loss of keratinisation, and indicates that further optimisation may be needed for tissue processing steps after organoids have been transferred to 2% agarose.

As can be observed from Figure 4.6 and Figure 4.7, no visible regions of hypoxia fluorescence could be detected when organoid samples were treated with pimonidazole and Hoechst 33342 stains. This is potentially due to the organoid diameter not being sufficiently large enough to result in any impairment in oxygen perfusion to cells in the centre of the organoids. Indeed, the diameters of the ACS-HN04 and ACS-HN18A organoids were relatively small, at approximately 100 µm and 200 µm respectively compared to the diameter exceeding 400 µm observed with the HCT116 spheroids that did successfully demonstrate hypoxia (Figure 4.5). Of the PDX model lines stained with pimonidazole by Harms et al (2019), ACS-HN04 was among the PDX tumours that demonstrated the most extensive levels of hypoxia, although there are no published pimonidazole staining records for ACS-HN18A PDX tumours. Previously published records of organoid pimonidazole stains demonstrated fluorescent hypoxic regions in organoids exceeding 250 µm in diameter across multiple cancer types

(Fanchon et al., 2020; Ramamoorthy et al., 2019; Ruscetti et al., 2020). Further confounding matters is the presence of condensed nuclei in the centre of the HCT116 spheroids as detected by Hoechst 33342 staining; this is a morphology more commonly associated with cells undergoing apoptosis rather than the necrotic cells typically observed in HNSCC tumours (Crowley et al., 2016; O'Connor et al., 2016b), although a similar morphology has been observed in HCT116 cells confirmed to be hypoxic when imaged in 3D (Beghin et al., 2022). In contrast, no such apoptotic core can be observed in the ACS-HN04 or ACS-HN18A organoid models (Figure 4.6 and Figure 4.7).

5 Genomic Characterisation of PDX-derived Organoid Models of HNSCC

5.1 Introduction

In order to characterise the gene expression profile for PDX-derived organoid models of HNSCC, a whole-transcriptome sequencing method known as paired-end RNA sequencing (RNAseq) was selected. This approach possesses two key advantages that make it uniquely well suited to characterising the organoid models generated in this project. Firstly, this technique allows for the detection of all genes present in the transcriptome and the quantification of their expression, irrespective of the cell species and without prior knowledge of the genome (Singh et al., 2018). Thus, the fact that there is no published record of prior PDX-derived HNSCC organoid generation or characterisation does not serve as a hindrance to carrying out RNAseq. Secondly, as this technique has been carried out previously on the PDX models that the organoids were derived from (unpublished data), it is possible to establish a correlation coefficient between the gene expression profiles of the PDX models and the corresponding PDX-derived organoids. In earlier research, PDX-derived organoid models have been shown to faithfully recapitulate the gene expression activity of their matched PDXs across a wide range of different cancer types (Guillen et al., 2022; Huang et al., 2020; Takada et al., 2021; Wang et al., 2022). For example, using a single-cell RNAseq technique, Wang et al (2022) demonstrated that patient-derived organoids for colorectal carcinoma preserve the aberrant mutational landscape (including copy number variations) and gene regulatory networks present in the primary tumours. Similar results were observed with patient-derived-HNSCC organoids as carried out by Driehuis et al (2019), where the mutational landscape of the primary tumours was recapitulated by the organoids across the three tumour lines where primary tumours and patient-derived organoids were sequenced in parallel. However, the variant allele frequency was slightly elevated in the organoids, which was attributed to the lack of immune cells present in the organoids (Driehuis et al., 2019). Against this backdrop and in light of the fact that there is no published record of such a study being carried out with PDX-derived organoids for HNSCC, it is predicted that the PDX-derived organoids generated in this project would similarly recapitulate the expression profile of their matched PDXs.

In addition to establishing correlations at the whole-genome level, RNAseq can also be used to establish correlations of expression patterns from a small number of genes associated with a specific phenotype, known as a gene signature. One such phenotype for which a multitude of signatures have been developed and implemented is tumour hypoxia (see Section 1.2.2). An example of such a signature is the Toustrup tumour hypoxia signature, comprised of 15 different genes that can stratify HNSCC patients on the hypoxia status of their tumour (Toustrup et al., 2012; 2016). Evaluation of the Toustrup signature in the organoid models provides an orthogonal method to pimonidazole for the evaluation of tumour hypoxia, while also allowing for the direct comparison of gene expression between these models and the corresponding PDX tumours developed by Harms et al (2019).

5.2 RNA Extraction

RNA extraction was carried out using Trizol on three different organoid models; ACS-HN04, ACS-HN09 and ACS-HN18A as well as HCT116 spheroids as per Section 2.4.1, after which point a 1 µL sample was analysed by TapeStation for total RNA yield and sample quality, measured by RNA Integrity Number (RINe). Total RNA yields across all organoid samples varied between 68 ng and 218 ng, with a lowest RINe of 6.2 and a highest of 9.9 (see Table 5.1). The HCT116 spheroids had a total RNA yield of 8,080 ng and RINe of 9.9. The relatively low yields of organoid RNA compared to HCT116 are due to comparatively low cell inputs, with 150,000 total cells each for the ACS-HN04 and ACS-HN09 samples, and 390,000 total cells for the ACS-HN18A organoids, which was necessitated by the need to set aside cells for the other characterisations in Chapters 4 and 6. Due to cell losses occurring during passaging of ACS-HN18B, there was not sufficient cellular material available to carry out RNA extraction. Given these results and that subsequent steps of PolyA enrichment and cDNA preparation required a minimum total RNA input of 10 ng according to kit protocols, the organoid samples were deemed to have sufficiently high quality and yield to proceed with these downstream processing steps.

Table 5.1 RNA total yields and quality after extraction

Organoid Sample	Total Yield (ng)	RINe
ACS-HN04	70	7.8
ACS-HN09	68	6.2
ACS-HN18A	218	9.9
HCT116 Spheroid	8,080	9.9

5.3 cDNA library preparation

RNA samples were enriched for mRNA using the the Bioo Scientific NEXTflex Poly(A) Beads 2.0 kit, after which the the Bioo Scientific Rapid Directional RNA-Seq Kit 2.0 was utilised to prepare cDNA libraries as described in Section 2.4.3. The cDNA samples were quality checked using the Qubit High Sensitivity DNA kit and TapeStation. However, neither method was able to calculate a concentration readout for any of the samples tested. Therefore, these samples were deemed to have failed the quality checks necessary for downstream sequencing using the Illumina protocol. Given that all of the available RNA was used for cDNA library preparation and these results emerged less than 4 weeks before the scheduled end of the project, there was not sufficient time available to regrow the cells, extract the RNA and prepare new cDNA libraries. Therefore, it was not possible to generate RNAseq data for the organoids or HCT116 spheroids in this project.

5.4 Discussion

Despite RNA being successfully extracted from the organoids and from the HCT116 spheroids, the lack of any Qubit or TapeStation signal suggests that complete sample losses occurred during cDNA preparation. Although it is not known at what stage during the library preparation protocol the sample losses occurred, it is possible that human error may have had some role. The fact that lack of Qubit signal occurred after PCR amplification suggests that the sample loss occurred upstream of this step. A possibility was the step that was carried out immediately after RNA extraction; Poly(A) enrichment. This step is designed to filter the mRNA from the total extracted RNA by hybridising OligoDT primers attached to magnetic beads to the Poly(A) tails present in mRNA molecules (Grentzinger et al., 2020). Thus, it becomes possible to separate the non-mRNA fraction – approximately 85-90% of total extracted RNA – from the mRNA molecules (Bogdanova et al., 2008; Grentzinger et al., 2020). If, however, the OligoDT primers failed to hybridise with the Poly(A) tails, the mRNA would have been discarded alongside the non-mRNA fraction during the separation process. Indeed, previous research has indicated an elevated risk of this occurring in low-input samples of RNA (Zhao et al., 2014). Thus, if higher concentrations of extracted RNA from the organoid samples were available, it is possible that cDNA preparation could have still been successful.

An alternative method of gene expression quantitation for HNSCC organoids that could have been utilised in this project was NanoString. This technique involves the use of fluorophore-conjugated reporter probes that bind specifically to the mRNA sequences that relate to a predetermined set of genes, with the level of fluorescence emitted by each probe proportionate to the levels of gene expression (Bentley-Hewitt et al., 2016). As such, NanoString possesses a key limitation that whole-transcriptome sequencing based techniques do not; as genes to be analysed have to be preselected prior to carrying out the quantitation, some knowledge of the genome is required (Ellinghaus et al., 2017). However, due to the development and validation of hypoxia gene signatures for HNSCC such as that by Toustrup et al (2012), this technique can be utilised to evaluate differences in hypoxia-mediated gene expression between different cell models for HNSCC. Indeed, this technique was previously utilised by the ACSRC to demonstrate that PDX models for HNSCC strongly recapitulate the hypoxia-mediated gene expression profiles present in their primary source tumours (Harms et al., 2019). Thus, a similar experiment could have been carried out to compare the expression of genes within the Toustrup hypoxia gene signature berween these previously generated PDX models and the PDX-derived organoid models. This would have provided greater clarity of the hypoxic state of the cells within each organoid, thereby enabling a stronger conclusion to be drawn about the sensitivity of pimonidazole staining. Furthermore, this approach could also have been utilised to determine whether any correlation between organoid tumour hypoxia and reported evofosfamide sensitivity. This approach does not require Poly(A) enrichment nor cDNA library preparation, thus minimising the risk of sample loss post-extraction (Bentley-Hewitt et al., 2016). Finally, the Toustrup gene signature could also have been utilised with other approaches, such as qRT-PCR (Real-Time Quantitative Reverse Transcription PCR) or ddPCR (Droplet Digital PCR).

6 Sensitivity of PDX-derived HNSCC Organoids to Evofosfamide

6.1 Introduction

To assess if the PDX-derived HNSCC organoids were a suitable model for evaluating drug therapy, the organoids were subjected to a range of concentrations of the hypoxia-activated prodrug evofosfamide, after which they were subjected to the CellTiterGlo 3D assay. CellTiterGlo 3D assays are a form of luminometric assay which can be used to directly measure the viability of 3D cell cultures. To carry out these assays, a CellTiterGlo 3D solution is added to cells in 3D culture, allowing the cells to be lysed directly in the well, releasing their ATP. In addition to lysing the cells, CellTiterGlo 3D solution contains a luciferase enzyme which converts luciferin into oxyluciferin, a reaction that leads to luminescence being emitted (Forsyth et al., 2018; Gantenbein-Ritter et al., 2008). This luciferase enzyme is catalysed by the ATP released from lysing the cells; thus, the amount of luminescence emitted is directly proportional to the ATP released and therefore the overall number of viable cells (Dominijanni et al., 2021; Gantenbein-Ritter et al., 2008).

In organoid models, CellTiterGlo3D assays have been frequently used to elucidate the effect of drug treatment on the viability of organoid cells (Lee at al., 2018; Xie & Wu, 2016). For example, Lee et al (2018) pretreated 11 different patient-derived organoid models with 26 different anticancer drugs to demonstrate what differing concentrations of these drugs had on overall cell viability compared to controls. In these assays, CellTiterGlo 3D assay was successfully utilised to determine concentration-response relationships and IC_{50} values in all the organoid models tested (Lee et al., 2018). Similarly successful results have been observed with HNSCC patient-derived organoids. Indeed, Driehuis et al (2019) successfully observed concentration-response relationships on organoid viability with three drugs that form part of the current standard-of-care therapeutic regimen for HNSCC (cisplatin, carboplatin and cetuximab).

Evofosfamide (also known as TH-302) is a HAP that is selectively activated in cells undergoing hypoxia. Mechanistically, this is achieved by a two-step process. Evofosfamide is first subjected to one-electron reduction to a radical anion prodrug mediated by endogenous reductase enzymes, such as Cytochrome P450 reductase (POR) and other members of the cytochrome P450 superfamily (Hong et al., 2018; Weiss et al., 2008). Under normoxia, the radical anion prodrug reacts with the oxygen present in the cell, yielding superoxide and the original evofosfamide prodrug (Hong et al., 2018). Thus, evofosfamide remains inert under normoxic conditions (Weiss et al., 2011). However, under conditions of severe hypoxia, the radical anion prodrug is free to undergo further reduction at its nitroimidazole site to form a hydroxyl amine compound, followed by fragmentation to form the active compound, known as a brominated isophosphoramide mustard (Br-IPM) (Hong et al., 2018, Weiss et al., 2008). Alternatively, Br-IPM can be fragmented from evofosfamide directly (Weiss et al., 2008). Once Br-IPM is formed, it is able to induce cross-linking of DNA, leading to the inability for the affected cell to replicate its DNA and therefore undergo mitosis (Hong et al., 2018). This is sufficient to result in apoptosis of the affected cells (Weiss et al., 2008).

CellTiterGlo 3D assays have not been previously attempted with PDX-derived organoid models for HNSCC. Here, CellTiterGlo 3D assays are used to evaluate the potency of evofosfamide in PDX-derived HNSCC organoid lines through the calculation of an IC_{50} value for the reduction of cell viability compared to untreated cells.

6.2 Protocol Optimisation

As this assay had never been previously attempted on PDX-derived organoids for HNSCC, the CellTiterGlo 3D treatment protocol had to first be optimised. Multiple assay development steps were taken to arrive at the finalised protocol described in Section 2.5, which are outlined in the subsections below.

6.2.1 Correlation between Organoid Cell Number and Luminescence

In order to ensure that viable cell number can be correlated with luminescent signal, the optimal seeding density in the assay plate needed to be determined. Before this, however, a suitable method for transferring the organoids from the culture plate to the assay plate without losing cell viability needed to be determined. Initially, the direct transfer of organoids without splitting into single cells was attempted by transferring between 250 and 4000 organoids from the culture plate to an opaque 96-well assay plate, as this approach had been successfully implemented with other cancer organoid models (Francies et al., 2016; Hou et al., 2018). However, this approach was not successful with the ACS-HN04 organoids, as when they were treated with the CellTiterGlo 3D solution, there was no clear relationship between observed luminescence and seeding density. A second attempt at this approach was then carried out with the opaque 96-well plate substituted for a clear-bottom 96-well plate with opaque walls. Upon visual inspection of this plate, it was discovered that no organoids had been successfully transferred from the 24-well culture plate. This necessitated a different approach to organoid cell transfer, where the organoids were disrupted to form a single cell suspension, then transferred to a 96-well round-bottom ultra-low attachment plate and seeded at 3 different densities (1,000, 2,000 and 5,000 cells per well). This was immediately followed by centrifugation for 3 min at 1,000 rpm to ensure close cell-to-cell contact, thereby encouraging organoid re-establishment. This technique has been used successfully to encourage rapid organoid formation in-well across multiple cell types in preparation for CellTiterGlo 3D assays (Ouchi et al., 2019; Tamura et al., 2018; Whyard et al., 2020; Xie & Wu., 2016).

Representative images were captured using a light microscope after seeding into the assay plate for validation. To determine the extent to which the PDX-derived HNSCC organoids form, images were captured after two days incubation at 37 °C. After two days, the cells seeded at 1,000 cells per well remained single cells, whereas approximately 50-100 small organoids had formed at the 2,000 cell per well seeding condition (Figure 6.1). In contrast, a large spheroid-like structure had appeared in the 5,000 cells per well condition, surrounded by smaller organoids and single cells.

Day 0 **Day 2**

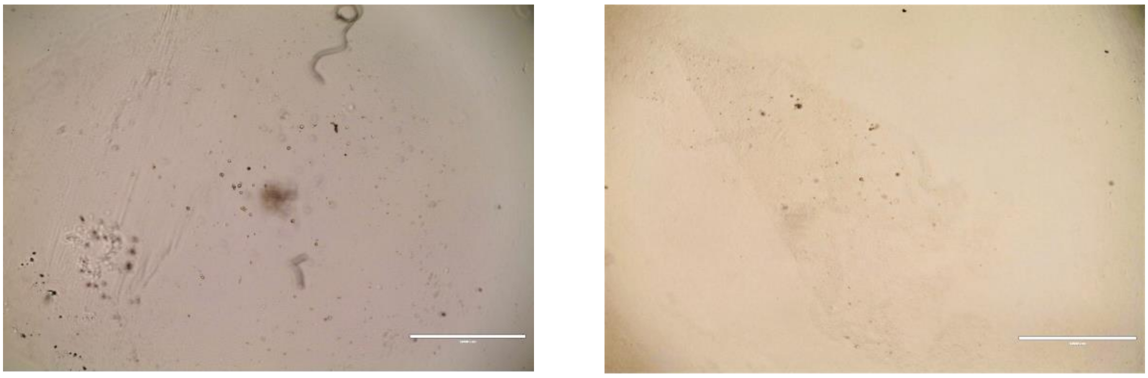

1,000 cells per well 1,000 cells per well

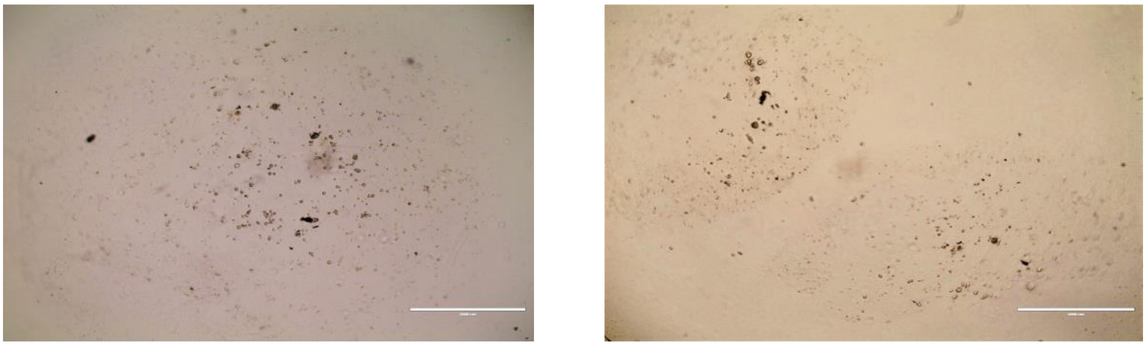

2,000 cells per well 2,000 cells per well

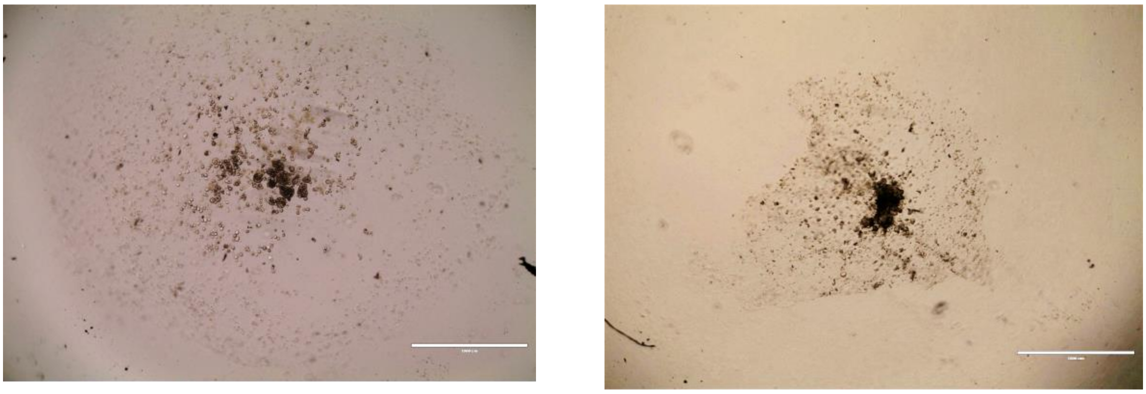

5,000 cells per well 5,000 cells per well

Figure 6.1 Representative organoid cell images captured using an Evos light microscope following seeding the single cells into an ultra-low attachment plate, captured immediately after seeding into the plate and after 2 days incubation at 37 ^{0}C. Scale bar = 1000 µM.

After 5 days post-seeding, the organoids were treated with CellTiterGlo 3D solution and luminescence was detected using the Enspire plate reader. A clear relationship between observed luminescence and viable cell number could be observed (Figure 6.2), although this was only at n=1, due to cell losses that occurred during a media change on Day 3 in some of the replicate wells. Based on these findings, 2,000 cells per well was chosen as the optimal seeding density for future CellTiterGlo 3D treatment assays, as this seeding density provided a strong luminescence signal while limiting the overall number of cells required for these experiments, meaning that the scarce cell resources available could be deployed to other experiments included in this project. All samples were also subjected to a two-day incubation period at 37 ^{0}C to allow for the formation of small organoids in-well prior to the administration of drug treatments.

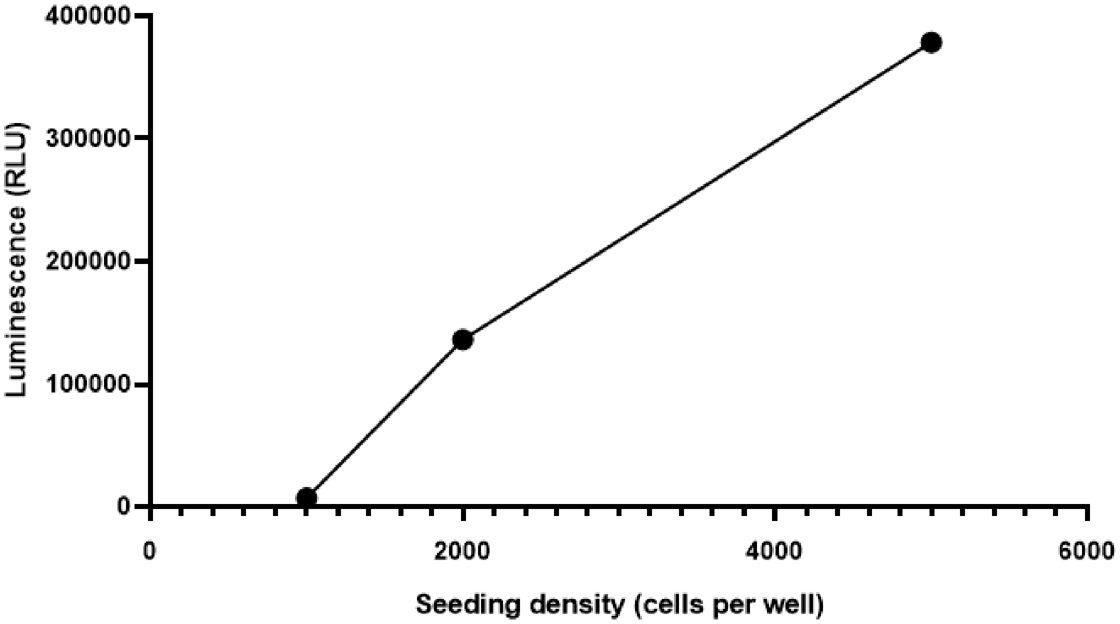

Figure 6.2. ACS-HN04 Organoid luminescence readouts after 5 Days incubation in the ultra-low Attachment 96-well plate. Organoids were split into single cells and seeded into ultra-low attachment plates at 3 different seeding densities: 1000, 2000 and 5000 cells per well.

6.2.2 Correlation between Evofosfamide-mediated Cytotoxicity and Luminescence

Having established the optimal seeding density, it was then necessary to evaluate the suitability of the CellTiterGlo 3D assay for evaluating evofosfamide activity in the 3D cultures, prior to testing on the organoids. A sigmoidal concentration-response relationship was observed in HCT116 spheroids treated with evofosfamide, allowing for the calculation of an IC_{50} value for evofosfamide-mediated cytotoxicity, which was 9.70 µM (n=1) (Figure 6.3). Based on the successful result of this trial assay in HCT116 spheroids, CellTiterGlo 3D evofosfamide treatment assays were next carried out on the organoid lines.

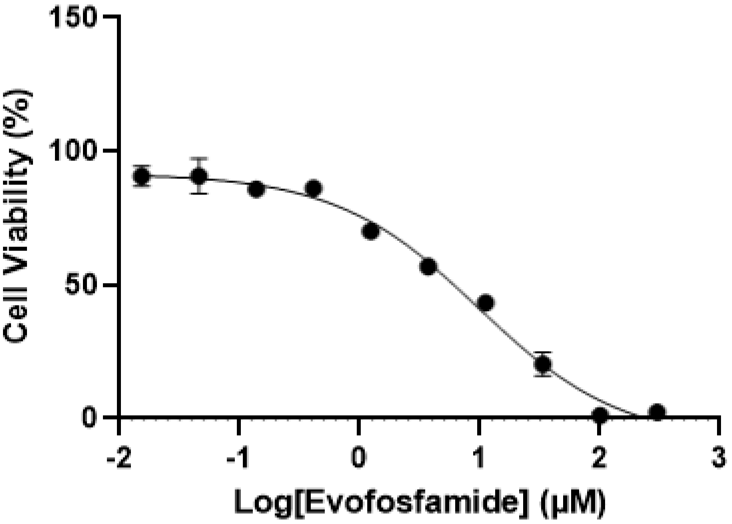

Figure 6.3. IC_{50} Concentration Response Curve (n=1) for Evofosfamide for HCT116 spheroids. Spheroids were split into single cells and seeded at 2,000 cells per well into 96-well ultra-low attachment plates, prior to treatment with evofosfamide at concentrations ranging from 0.015 µM to 300 µM for 3 days. Data was visualised using GraphPad Prism and error bars are mean ± SEM for duplicate data points.

6.3 Organoid Evofosfamide Drug Treatments

Four different organoid lines (ACS-HN04, ACS-HN09, ACS-HN18A and ACS-HN18B) were used to test for evofosfamide sensitivity by Cell Titer Glo 3D cell viability assay. Cells were treated with evofosfamide in duplicate wells, with concentrations ranging from 0.096 µM to 300 µM prepared as serial dilutions in Organoid Medium containing 5% BME (OM5%) (see (Section 2.5.2). Organoids were incubated with each drug condition for 3 days, prior to being lysed with the CellTiterGlo 3D solution and analysed for luminescence.

Evofosfamide showed a high level of potency for cytotoxicity across all organoid lines tested. As can be observed from Figure 6.4 and Table 6.1, the mean IC_{50} values for evofosfamide were below 10 µM. One organoid line, ACS-HN04, showed a similar mean IC_{50} value (8.86 ± 0.93

µM) to that observed with the HCT116 cell line (9.70 µM), while the three other organoid lines tested showed considerably lower IC_{50} values, including the ACS-HN09 organoid line with an IC_{50} value of 1.44 ± 0.15 µM, the ACS-HN18B line at 3.93 ± 0.01 µM and the ACS-HN04 line at 8.86 ± 0.93 µM (Table 6.1). Notably, there was a >9-fold difference in IC_{50} value between the ACS-HN18A and ACS-HN18B organoid lines, despite both organoid lines being derived from the same primary tumour.

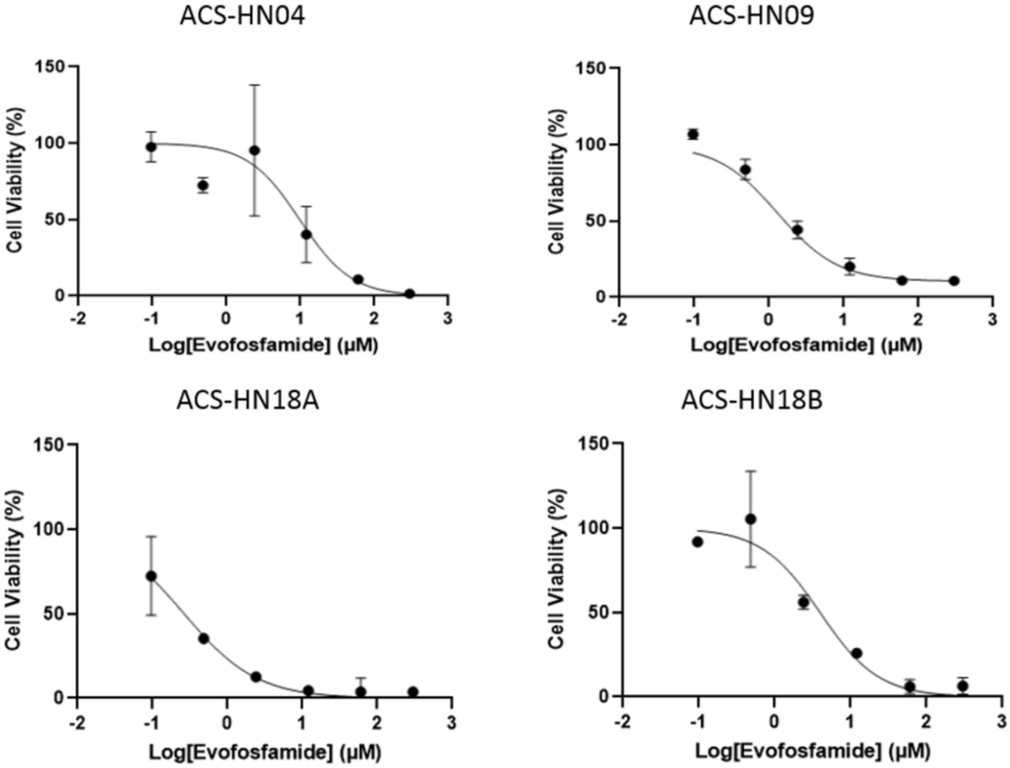

Figure 6.4. Representative IC_{50} Concentration Response Curves for Evofosfamide (TH-302) across 4 organoid lines (ACS-HN04, ACS-HN09, ACS-HN18A, ACS-HN18B). Organoids were split into single cells and seeded into 96-well ultra-low attachment plates, prior to treatment with evofosfamide at concentrations ranging from 0.096 µM to 300 µM for 3 days. Data was visualised using GraphPad Prism and error bars are mean ± SEM for duplicate data points.

Table 6.1. IC_{50} values for organoid viability following treatment with evofosfamide, calculated from two independent experiments in duplicate (mean ± SEM).

Organoid Line	Mean IC_{50} (µM)
ACS-HN04	8.86 ± 0.93
ACS-HN09	1.44 ± 0.15
ACS-HN18A	0.42 ± 0.16
ACS-HN18B	3.93 ± 0.01

6.4 Discussion

In order to evaluate the suitability of the organoid models as a tool for evaluating drug therapies, four PDX-derived HNSCC organoid lines (ACS-HN04, ACS-HN09, ACS-HN18A and ACS-HN18B) were incubated with evofosfamide for a period of 3 days in order to assess the impact of drug concentration on overall organoid cell viability. All four organoid lines showed high levels of evofosfamide sensitivity in these assays, with an IC_{50} of below 10 µM observed in all organoid models assessed. ACS-HN18A was the most sensitive with an average IC_{50} of 0.42 µM, which was almost 10-fold more sensitive than the IC_{50} for ACS-HN18B. Given that these organoid models showed sensitivity to evofosfamide, it is likely that they would be suitable for evaluating other drug therapies.

Evofosfamide was used in this project to assess the utility of the organoid models for evaluating drug therapy since it has been previously tested in the PDX tumours that the organoids were derived from. The evofosfamide growth inhibition assays carried out on the PDX models by Harms et al (2019) showed that the ACS-HN18 showed elevated levels of evofosfamide sensitivity compared to the ACS-HN04 and ACS-HN09 PDXs (Figure A1 in Appendix). Thus, the PDX models show a similar rank order in terms of evofosfamide sensitivity to what was observed in the corresponding organoid models. This similarity in rank order suggests that the organoid models successfully recapitulate the evofosfamide sensitivities reported in the PDX tumours.

Of additional interest is how the organoid IC_{50} values for evofosfamide treatment compared to previously reported evofosfamide IC_{50} data for immortalised cell lines for HPV-negative HNSCC. Indeed, Jamieson et al (2018) carried out evofosfamide growth inhibition assays across 26 such cell lines, grown as 2D monolayer cultures. The organoid models treated with evofosfamide as part of this project appear to show a higher level of evofosfamide sensitivity overall, with three of the four organoid models (ACS-HN09, ACS-HN18A and ACS-HN18B) reporting lower evofosfamide IC_{50} values than all of the immortalised cell lines tested by Jamieson et al (2018) (Figure A2 in Appendix). Furthermore, only one of the immortalised cell lines (UT-SCC-16A) demonstrated a lower mean IC_{50} (6.7 µM) than the ACS-HN04 organoid line (8.9 µM) (Jamieson et al., 2018). However, as these immortalised cell lines were only incubated with evofosfamide for 4 h prior to being assessed for growth inhibition, compared to the 3-day long incubation for the organoids in this project, it is possible that the organoid models simply appeared more sensitive due to the longer incubation time. Yet, in a more recent study, two HPV-negative HNSCC cell lines (FaDu and Cal33) grown as both 2D monolayers and 3D tumour spheroids, were incubated with evofosfamide for 3 days and, reported mean IC_{50} values of 65.6 µM (FaDu) and 135 µM (Cal33 spheroids) (Close & Johnston, 2022). Intriguingly, despite showing more extensive hypoxia when stained with pimonidazole, the 3D spheroid cultures were less sensitive to evofosfamide than the 2D monolayers (Close & Johnston, 2022). When these findings are taken together with the absence of pimonidazole staining in the ACS-HN04 and ACS-HN18A organoid observed in Section 4.4, the possibility is raised that both the organoid samples generated in this project and the FaDu and Cal33 immortalised cell lines are mildly hypoxic, but below the threshold of detection for pimonidazole. Alternatively, the growth of the organoids in the ULA plate 2 days prior to being treated with evofosfamide could have potentially caused the organoids to become more hypoxic. Further investigation is required to elucidate what the role of hypoxia might be in driving the observed evofosfamide sensitivity in these organoids.

Despite being derived from the same primary patient tumour, a difference over 9-fold in mean IC50 values across the ACS-HN18A and ACS-HN18B organoids was observed for evofosfamide-mediated organoid cytotoxicity. A potential driver of these differences is the distribution of cells within the PDX tumour that was utilised to generate the organoids in this project. If the cells within the 800-1500 mm^3 PDX tumours that the organoids were derived from were unevenly distributed, it is possible that the 125 mm^3 fragment selected for organoid culture did not contain the same diversity of cell types present in the original PDX tumour. The H+E images captured for both ACS-HN18A and ACS-HN18B organoids appear to demonstrate that such differences exist, with each ACS-HN18 organoid showing a distinct cellular arrangement and morphology (Figure 4.4). Alternatively, as the PDX tumours that these organoid models were derived from were grown in different mice, it is possible that differences specific to the mouse host may influence gene expression, and that these differences may affect evofosfamide sensitivity in the corresponding organoids. Indeed, it has already been observed that in 5 different PDX cancer models including HNSCC, new PDX-specific alterations in gene expressions occurred, with these alterations increasing with each passage number (Ben-David et al., 2017). However, due to the lack of RNAseq data for these organoid lines, it was not possible to fully characterise the range of cell types contained within each organoid, nor investigate the differences in gene expression that may have resulted in differences in evofosfamide sensitivity.

7 Overall Discussion

The primary aim of this project was to establish novel PDX-derived organoid models for HNSCC, and to evaluate the ability of these newly-generated models to recapitulate key aspects of the PDX tumours they were derived from. Ten such models grew successfully until their first passage, while four of them were successfully characterised. These four models did appear to recapitulate some key aspects of the PDX models. These characterisations include the histological investigation of cellular arrangement and regions with tissue hypoxia, as well as evofosfamide sensitivity. Clear similarities existed between the organoids and the PDX models they were derived from. For instance, histological staining using H+E identified that all the organoid models appeared to preserve the prevailing morphology of the key cell type involved in HNSCC: squamous epithelial cells. Additionally, all organoid models showed sensitivity to evofosfamide, with the degrees of sensitivity in each organoid line appearing to correlate with the observed evofosfamide sensitivities in the matched PDX tumours.

However, there did appear to be some key differences between the matched organoid and PDX models. For example, although the ACS-HN04 and ACS-HN18A were stained with pimonidazole, no hypoxia was visible, despite hypoxia clearly being present on the corresponding PDX tumour (Harms et al., 2019). Furthermore, as RNA-seq data could not be generated for the organoid models, it was not possible to compare the expression of hypoxia gene signatures in the organoids to that observed in the matched PDX tumours, nor was it possible to correlate it to the extent of observed organoid pimonidazole staining.

Given the negative pimonidazole staining result in both ACS-HN18A and ACS-HN04 organoids, which were the most and least evofosfamide-sensitive lines respectively, the mechanism driving the evofosfamide sensitivity observed in the organoids is not completely clear. Previous research has identified that tissue samples must have regions with a pO_2 of 10 mmHg or lower in order to stain positively for pimonidazole (Raleigh et al., 1998; Westbury et al., 2007). Additionally, combination staining of HNSCC primary tumours with pimonidazole and anti-HIF1α fluorescent antibodies showed extensive regions of mild hypoxia that was not detected by pimonidazole staining (Swartz et al., 2022). Thus, the combination of high observed evofosfamide sensitivities and negative pimonidazole staining suggest that the organoid models could contain mild hypoxia ($10 \text{ mmHg} < pO_2 < 20 \text{ mmHg}$) that could potentially be sufficient to activate evofosfamide, but not sufficient to stain positively for pimonidazole (McKeown, 2014). This in turn suggests that a more sensitive hypoxia staining technique is necessary to determine the presence or absence of mild hypoxia in these organoid models.

Alternatively, it is also possible that evofosfamide could be activated in these organoids in a hypoxia-independent manner. One early hypothesis for hypoxia-independent evofosfamide sensitivity was a bystander effect, which suggests that while evofosfamide is converted via a radical anion prodrug intermediate to Br-IPM in hypoxic cells, Br-IPM can readily perfuse cell plasma membranes in neighbouring normoxic cells (Sun et al., 2012). This can then lead to evofosfamide-mediated cytotoxicity in these neighbouring cells in addition to the hypoxic cells (Sun et al., 2012). However, this hypothesis has since been refuted, with Hong et al (2018) demonstrating using HCT116 3D cultures that the bystander effect observed by Sun et al (2012) is due to the presence in their multicellular cocultures of the E. coli nitroreductase NfsA, a hypoxia-nonspecific two-electron reductase that produces a hydroxylamine metabolite different to Br-IPM. Additionally, Hong et al (2018) showed that Br-IPM, unlike evofosfamide, does not readily perfuse cell plasma membranes due to its high hydrophilicity. It has been observed that high concentrations of intracellular evofosfamide can lead to cytotoxicity in normoxic HCT116 cells grown as 3D cultures, potentially due to some of the radical anion prodrug intermediate escaping back-conversion to evofosfamide and instead being converted to Br-IPM and subsequently mediating downstream cytotoxic effects (Hong et al., 2018). However, further research is required to determine which of these mechanisms, if any, are driving the observed normoxic cytotoxicity present in the organoid models included in this project.

Although a novel approach with respect to HNSCC, PDX-derived organoid models have been successfully established for other cancer types. This enables a comparison between the different types of PDX-derived organoids of their ability to recapitulate their source tissue. Like PDX-derived organoid models for other cancer types (Guillen et al., 2022; Huang et al., 2020; Takada et al., 2021), the organoid models generated in this project recapitulate the oncogenic tissue type of interest when subjected to H+E staining. However, one key difference distinguishes these published records with the organoid models generated in this project; all these records used organoid models that had been successfully established using long-term culture methods (Guillen et al., 2022; Huang et al., 2020; Takada et al., 2021). In contrast, none of the organoid models grown as part of this project survived 3 passages. As a result, fewer comparisons were carried out in this project compared to the published protocols, due to the relative scarcity of organoid tissue available for experimentation. Further exacerbating this issue was the inability to generate RNA-seq data as part of this project, meaning that neither the gene mutational landscape nor expression activity could be analysed. Given these issues, the characterisation experiments carried out in this project cannot be used to conclusively demonstrate that the organoids recapitulate the primary tumours. However, had sufficient tissue been available for analysis and based on the preliminary findings from this project with respect to histological characterisation and evofosfamide drug sensitivity, it is likely that the organoid models generated in this project would have been able to successfully recapitulate the PDX tumours in the same fashion as the PDX-derived organoids generated for other cancer types (Guillen et al., 2022; Huang et al., 2020; Takada et al., 2021).

ACS-HN18A and ACS-HN18B were derived from the same PDX model, yet considerable differences existed in their tissue histology and evofosfamide sensitivity. This is likely due to the heterogeneity of cell types contained within the PDX tumour, as each PDX tumour originates from different tumour fragments and therefore can have a different cell composition.. One method to account for the cellular heterogeneity of the PDX tumours would be to grow multiple organoid models in parallel from different tumours from the same PDX model.

7.1 Limitations and Future Directions

As with all scientific research, the methods of experimentation had limitations which adversely impacted the utility of the data collected. By identifying these limitations, they can be used to guide the development of improved experimental protocols so that they are ameliorated in the future.

7.1.1 Organoid Culture

Perhaps the limitation with the most widespread effects across this entire project is that none of the organoid models that were grown were successfully established as long term cell cultures, with negligible growth occurring in most models beyond 1 month and three passages. This significantly limited the amount of tissue available for downstream characterisation, and is the reason why evofosfamide was the only drug therapy that could be tested (and only at 6 different concentrations) and only a small number of H+E and pimonidazole images could be generated for the organoid models. This also limited the total RNA amount that was extracted from the organoids. Indeed, if PDX-derived organoid models for HNSCC are to have clinical utility as a platform for testing novel anti-HNSCC therapies, the organoids need to be able to be grown and expanded across multiple passages to ensure there is sufficient tumour material available. Thus, further optimisation of these organoid culture protocols is necessary in order to enhance the rate of growth of these cultures, as well as prolong the period in which they remain a viable cell culture.

One approach for culture optimisation is to follow a recent long-term organoid culture technique that has been successfully utilised to maintain viable organoid cultures for up to 6 months (Price et al, 2022). This culture technique has been validated across three patient-derived organoid models including oesophageal SCC, and involves the growth of organoids on an ultra-low-attachment (ULA) plate in a suspension that contains a relatively low concentration of extracellular matrix solution (5% BME) (Capeling et al., 2022; Price et al., 2022), compared to the highly concentrated solidified dome cultures (70% BME) used in this project. Additionally, the oesophageal SCC organoid model showed elevated rates of growth and enlarged diameters when grown in 5% BME suspension compared to solidified BME domes (Price et al., 2022). This is thought to be due to the organoids having increased space available to them for growth in the 5% BME suspension instead of being physically confined within the solidified BME domes (Capeling et al., 2022; Price et al., 2022). Although this culture method has not been validated in PDX-derived models in HNSCC, fairly rapid organoid growth was observed in all the organoid models in this project that were briefly grown in 5% BME suspension in preparation for evofosfamide drug treatment assays (Figure 6.1). Finally, the oesophageal SCC organoids grown in 5% BME suspension were also reported to highly conserve morphological characteristics, as well as gene expression profile and drug sensitivities compared to their primary tumours (Price et al., 2022). Thus, growing the organoids in a 5% BME suspension can be utilised as a starting point for which a long-term culture protocol for PDX-derived HNSCC organoids could be developed. Unfortunately, this protocol had not been published when the current study began. Given the aforementioned potential limitations of the L-WRN conditioned medium, this suspension culture method could be attempted with an organoid culture medium that has Wnt, R-spondin and Noggin at fixed concentrations, or alternatively, L-WRN medium whose Wnt, R-sponding and Noggin concentrations had been previously validated using the TOPflash assay (Veeman et al., 2003).

Additionally, when organoid models were cryopreserved and subsequently revived, the percentage retrieval rate of viable organoids was low across all cell models tested. Thus, improvements need to be made to the cryopreservation methods in order to improve cell retrieval rates. One solution that has been proposed is to reduce the amount of dimethyl sulfoxide (DMSO) present in the organoid freezing medium. While DMSO is necessary to prevent the formation of crystals inside the cryovial during the freezing process that can directly kill cells, DMSO has also been shown to itself be cytotoxic to organoid cells (Lee et al., 2022). Typically, organoid cryogenic freezing medium contains 10% DMSO (Driehuis et al., 2019; Karakasheva et al., 2020). However, recent research has identified that 5% DMSO can preserve the prevention of crystal formation while reducing the cytotoxicity to organoid cells (Lee et al., 2022). However, there is no published record of this difference having been validated in HNSCC organoid cells, both patient-derived and PDX-derived. Thus, in order to establish whether freezing medium composition has any effect on viable cell retrieval rates post cryogenic freezing, comparisons will need to be made between organoids cryogenically frozen in 5% DMSO and 10% DMSO freezing medium.

7.1.2 Histology

As mentioned above, the limited number or organoids in culture meant few organoids could be utilised for H+E staining. Furthermore, considerable sample losses occurred when organoid slides were being prepared for pimonidazole staining. One method to counteract this would be to minimise the sample processing steps used in this project that could potentially cause sample losses, from organoid harvesting to subsequent slide preparation using 10% NBF and 2% agarose. To that end, a novel method that enables direct cell staining and imaging has recently been developed by Beghin et al (2022). In this approach, tumour cells that have been trypsinised to single cells are seeded into a small chip located in the centre of each well of a 6-well culture plate. Within each chip are an array of cone-shaped wells known as JeWells, which can have a narrow tip of approximately 70 µm and a wider base of approximately 300 µm (Beghin et al., 2022). Tumour models that have been split into single cells can then be seeded into these wells, with the cone-shaped design ensuring that the cells in each JeWell remain in close contact with one another. This approach has resulted in relatively rapid organoid formation across multiple tumour cell types (Beghin et al., 2022). Furthermore, this approach has also been shown to support hypoxia and antibody-based staining techniques, as well as 3D live-cell imaging, thereby enabling hypoxia to be studied directly across the entire organoid structure (Beghin et al., 2022). As the samples are being imaged inside the JeWells, the potential for sample loss is greatly reduced compared to the current processing methods. Additionally, this method can also be used to supplement existing protocols. In this project, organoids were harvested for histological processing 6 days after the first passage. On the contrary, using a JeWell imaging workflow, the organoid cells intended for histology could be transferred directly to the JeWells at the time of their first passage and allowed to grow inside the JeWells prior to imaging. Indeed, a combined standard organoid culture and JeWell imaging workflow was validated by Beghin et al (2022).

7.1.3 RNA-Seq

Due to limited tissue available (150,000 cells each for ACS-HN04 and ACS-HN09 and 390,000 cells for ACS-HN18A) and complete sample loss during cDNA library preparation, no RNA-seq of the organoid models generated in this project could be carried out. Additionally, the low cell numbers available for genomic characterisation meant that no further attempts at library preparation could be pursued to determine if sample loss occurred due to user error or that the methodology was not appropriate for low input samples. One such alternative approach that could be used in future is known as Poly(A)-ClickSeq (Routh et al., 2017). Unlike the NextFlex protocol used in this project, which requires that Poly(A) enrichment and fragmentation be carried out prior to PCR amplification, the Poly(A)-ClickSeq protocol can be carried out directly on total extracted RNA (Elrod et al., 2019; Routh et al., 2017). Furthermore, this approach has been validated on total RNA samples with yields under 100 ng that had been extracted using Trizol, which further suggests that this approach may be suitable for low-yield organoid samples. However, as there are no published records of this method being used with organoid models, further validation is required.

7.1.4 Evofosfamide Treatments

Although the Cell Titre Glo 3D experiments were able to clearly demonstrate the differential sensitivities to evofosfamide between different organoid models, these experiments did contain some minor limitations. In some of the assay repeats, there were reported outlier wells, with reported cell viabilities exceeding 100% relative to the negative controls. Under microscope observation, it became apparent that these elevated viability values could be attributed to the presence of enlarged organoids exceeding 100 µm that failed to dissociate during the earlier trypsinisation step. Thus, these wells had an elevated number of cells compared to the standardised 2,000 cells per well and were consequently excluded from the final analysis. Secondly, for each assay carried out, only six concentrations of evofosfamide could be utilised for these assays, due a limited number of cells being available for each assay as a consequence of the aforementioned limitations with organoid culture, which may have impacted the accuracy of the IC_{50} determinations. Furthermore, there were not enough organoids available to test any other drug therapies to confirm the suitability of the organoid models for evaluating drug therapies.

Of great interest was the fact that all the organoid models showed a high sensitivity to evofosfamide (as measured by IC_{50}), yet the two models that were stained with pimonidazole (HN04 and ACS-HN18A) did not show any signs of hypoxia. This suggests there is a need to more clearly understand exactly what was driving evofosfamide sensitivity in these organoid models. In the future, this could be achieved by two distinct set of experiments.

Firstly, to confirm if the comparison in Section 6.4 that the PDX-derived HNSCC organoids are more sensitive to evofosfamide than HNSCC cell lines still holds true under the same assay conditions, the Cell Titre Glo evofosfamide sensitivity experiments carried out in this project could be repeated with the HNSCC immortalised cell lines utilised by Jamieson et al (2018). This would enable the evofosfamide sensitivities between the organoid models and the HNSCC cell lines to be directly compared. If the organoids continued to show elevated evofosfamide sensitivity compared to the immortalised cells lines (demonstrated by a lower IC_{50}) under the exact same assay conditions, then this may suggest there is hypoxia present in the organoids that is contributing to this increased sensitivity. This hypoxia could then be confirmed using the aforementioned combination pimonidazole and anti-HIF-1α staining technique utilised by Swartz et al (2022), which would have the added benefit of providing a semi-quantitative indicator of the severity of hypoxia within different regions of each organoid. The second future experiment to characterise the evofosfamide sensitivity in the organoids involves measuring the intracellular concentrations directly of evofosfamide and its pharmacologically active metabolites; Br-IPM and IPM. To do this, organoids can be treated with evofosfamide and incubated for the standard 3 days as per Section 2.5.2, prior to lysing the cells and performing a liquid chromatography with tandem mass spectrometry (LC-MS/MS) experiment to quantify the concentrations of evofosfamide, Br-IPM and IPM. Indeed, such an experimental approach has been validated using multiple cell types, including HCT116 spheroids and HNSCC immortalised cell lines (Hong et al., 2018; Jamieson et al., 2018). If evofosfamide is activated independently of hypoxia, these experiments will aid in determining whether the activation pathway is via Br-IPM or IPM, or by some as-yet-unidentified reaction pathway.

7.2 Conclusion

This project serves as the first documented record of the development of PDX-derived organoids for HNSCC. As such, it was necessary to develop and implement a novel tissue culture protocol so that the organoids could successfully be utilised for downstream experimentation. Such a protocol was developed and optimised for short-term organoid culture as part of this project, and led to the successful downstream characterisation of the cellular arrangement and drug sensitivity of four distinct PDX-derived organoid models for HNSCC. This preliminary research has identified that PDX-derived organoid models do successfully recapitulate squamous epithelial cells present in the PDX tumours, as well as mimic the variability in sensitivity to the hypoxia-activated prodrug evofosfamide in the source PDX tumours. However, the amount of tissue available for these comparisons was limited by the failure to establish long-term organoid culture, implying that further optimisation of HNSCC PDX-derived organoid culture protocols is required. This in turn would enable further characterisations such as gene expression analyses to be carried out on these organoid models, further shedding light on their suitability for evaluating the clinical utility of novel anticancer therapies.

Appendix 1 – Mean Growth and Survival Curves of PDX Models Treated with Evofosfamide

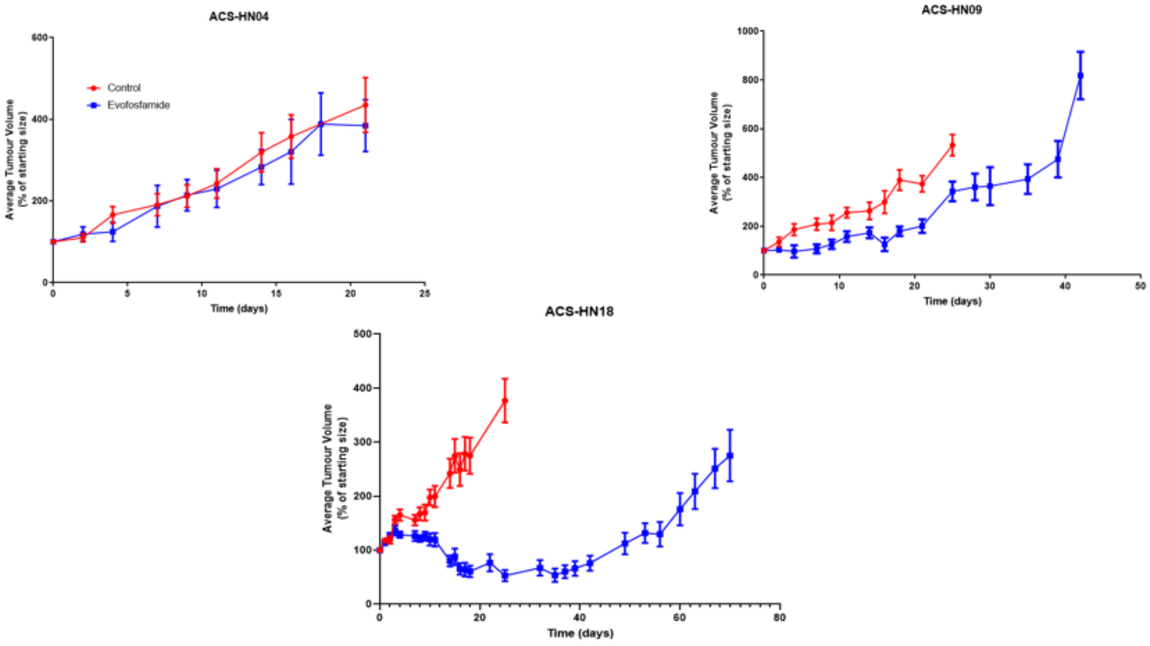

Figure A1 Average tumour growth in three different HNSCC PDX tumour models (ACS-HN04, ACS-HN09 and ACS-HN18) in mice treated 5 times daily for 3 weeks with evofosfamide at 50 mg/kg or control vehicle. Data points are mean ± S.E.M of n = 7-12 tumours. The graphs for the ACS-HN04 and ACS-HN09 PDX models are reproduced with permission from Harms et al (2019), while the graph for ACS-HN18 is unpublished data from the ACSRC.

Appendix 2 - Evofosfamide Sensitivity of HNSCC Cell Lines

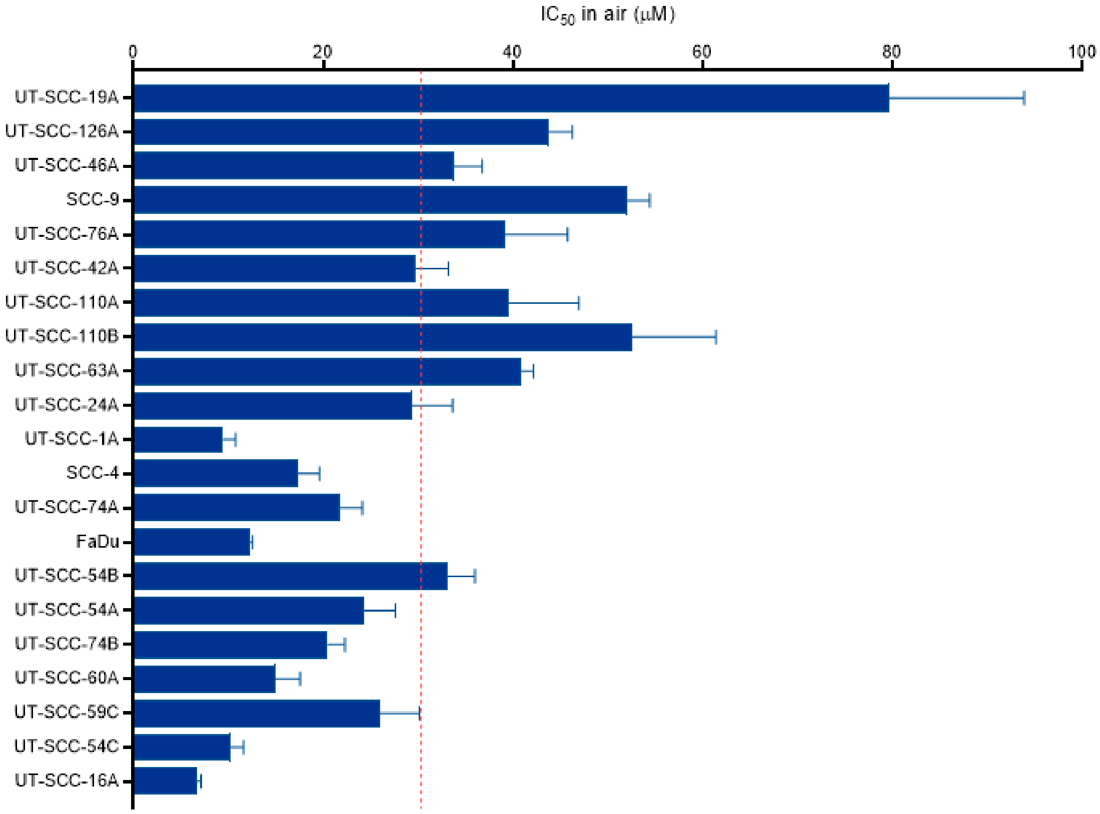

Figure A2 Antiproliferative activity of Evofosfamide, as measured by concentration required for 50% cell growth inhibition (IC_{50}). Cells were exposed to evofosfamide in for 4 hours under ambient air, prior to being subjected to Sulforhodamine B (SRB) colorimetry. Values are means ± S.E.M. for triplicate points, while the dotted red line indicates the mean IC_{50} across the entire cell line panel. Data reproduced with permission from Jamieson et al (2018).

References

Abhinand, C. S., Raju, R., Soumya, S. J., Arya, P. S., & Sudhakaran, P. R. (2016). VEGF-A/VEGFR2 signaling network in endothelial cells relevant to angiogenesis. *Journal of Cell Communication and Signaling, 10*(4), 347-354.

Abraham, J., Salama, N. N., & Azab, A. K. (2015). The role of P-glycoprotein in drug resistance in multiple myeloma. *Leukemia & Lymphoma*, *56*(1), 26-33.

Adam, M. F., Dorie, M. J., & Brown, J. M. (1999). Oxygen tension measurements of tumors growing in mice. *International Journal of Radiation Oncology* Biology* Physics, 45*(1), 171-180.

Aizawa, Y., Takada, K., Aoyama, J., Sano, D., Yamanaka, S., Seki, M., Kuze, Y., Ramilowski, J., Okuda, R., & Ueno, Y. (2022). *Experimental models of salivary gland cancer established using organoid culture and patient-derived xenografting*. Research Square. https://assets.researchsquare.com/files/rs-1621957/v1/087a388f-567c-43dd-a6cc-281ecad03420.pdf?c=1652288078

Ang, K. K., Harris, J., Wheeler, R., Weber, R., Rosenthal, D. I., Nguyen-Tân, P. F., Westra, W. H., Chung, C. H., Jordan, R. C., Lu, C., Kim, H., Axelrod, R., Silverman, C. C., Redmond, K. P., & Gillison, M. L. (2010). Human Papillomavirus and Survival of Patients with Oropharyngeal Cancer. *N Engl J Med, 363*(1), 24-35. 10.1056/NEJMoa0912217

Aparicio, S., Hidalgo, M., & Kung, A. L. (2015). Examining the utility of patient-derived xenograft mouse models. *Nature Reviews Cancer*, *15*(5), 311-316.

Argiris, A., Karamouzis, M. V., Raben, D., & Ferris, R. L. (2008). Head and neck cancer. *The Lancet, 371*(9625), 1695-1709.

Ayuso, J. M., Truttschel, R., Gong, M. M., Humayun, M., Virumbrales-Munoz, M., Vitek, R., Felder, M., Gillies, S. D., Sondel, P., & Wisinski, K. B. (2019). Evaluating natural killer cell cytotoxicity against solid tumors using a microfluidic model. *Oncoimmunology, 8*(3), 1553477.

Azuma, C., Raleigh, J. A., & Thrall, D. E. (1997). Longevity of pimonidazole adducts in spontaneous canine tumors as an estimate of hypoxic cell lifetime. *Radiation Research, 148*(1), 35-42.

Barati, T., Haddadi, M., Sadeghi, F., Muhammadnejad, S., Muhammadnejad, A., Heidarian, R., Arjomandnejad, M., & Amanpour, S. (2018). AGS cell line xenograft tumor as a suitable gastric adenocarcinoma model: growth kinetic characterization and immunohistochemistry analysis. *Iranian Journal of Basic Medical Sciences, 21*(7), 678.

Beckham, T. H., Barney, C., Healy, E., Wolfe, A. R., Branstetter, A., Yaney, A., Riaz, N., McBride, S. M., Tsai, C. J., & Kang, J. (2020). Platinum-based regimens versus cetuximab in definitive chemoradiation for human papillomavirus-unrelated head and neck cancer. *International Journal of Cancer, 147*(1), 107-115.

Bedford, J. S., & Mitchell, J. B. (1974). The effect of hypoxia on the growth and radiation response of mammalian cells in culture. *The British Journal of Radiology, 47*(562), 687-696.

Beghin, A., Grenci, G., Sahni, G., Guo, S., Rajendiran, H., Delaire, T., Mohamad Raffi, S. B., Blanc, D., de Mets, R., & Ong, H. T. (2022). Automated high-speed 3D imaging of organoid cultures with multi-scale phenotypic quantification. *Nature Methods, 19*(7), 881-892.

Ben-David, U., Ha, G., Tseng, Y., Greenwald, N. F., Oh, C., Shih, J., McFarland, J. M., Wong, B., Boehm, J. S., & Beroukhim, R. (2017). Patient-derived xenografts undergo mouse-specific tumor evolution. *Nature Genetics, 49*(11), 1567-1575.

Bentley-Hewitt, K. L., Hedderley, D. I., Monro, J., Martell, S., Smith, H., & Mishra, S. (2016). Comparison of quantitative real-time polymerase chain reaction with NanoString® methodology using adipose and liver tissues from rats fed seaweed. *New Biotechnology, 33*(3), 380-386.

Betof, A. S., Lascola, C. D., Weitzel, D., Landon, C., Scarbrough, P. M., Devi, G. R., Palmer, G., Jones, L. W., & Dewhirst, M. W. (2015). Modulation of murine breast tumor vascularity, hypoxia, and chemotherapeutic response by exercise. *JNCI: Journal of the National Cancer Institute, 107*(5)

Bhadury, J., Einarsdottir, B. O., Podraza, A., Bagge, R. O., Stierner, U., Ny, L., López, M. D., & Nilsson, J. A. (2016). Hypoxia-regulated gene expression explains differences between melanoma cell line-derived xenografts and patient-derived xenografts. *Oncotarget, 7*(17), 23801.

Bhandari, V., Hoey, C., Liu, L. Y., Lalonde, E., Ray, J., Livingstone, J., Lesurf, R., Shiah, Y., Vujcic, T., & Huang, X. (2019). Molecular landmarks of tumor hypoxia across cancer types. *Nature Genetics, 51*(2), 308-318.

Blot, W. J., McLaughlin, J. K., Winn, D. M., Austin, D. F., Greenberg, R. S., Preston-Martin, S., Bernstein, L., Schoenberg, J. B., Stemhagen, A., & Fraumeni, J. F. (1988). Smoking and drinking in relation to oral and pharyngeal cancer. *Cancer Research, 48*(11), 3282-3287.

Bodnar, B., Zhang, Y., Liu, J., Lin, Y., Wang, P., Wei, Z., Saribas, S., Zhu, Y., Li, F., & Wang, X. (2021). Novel scalable and simplified system to generate microglia-containing cerebral organoids from human induced pluripotent stem cells. *Frontiers in Cellular Neuroscience,* , 206.

Bogdanova, E. A., Shagin, D. A., & Lukyanov, S. A. (2008). Normalization of full-length enriched cDNA. *Molecular BioSystems, 4*(3), 205-212.

Boj, S. F., Hwang, C., Baker, L. A., Chio, I. I. C., Engle, D. D., Corbo, V., Jager, M., Ponz-Sarvise, M., Tiriac, H., Spector, M. S., Gracanin, A., Oni, T., Yu, K. H., van Boxtel, R., Huch, M., Rivera, K. D., Wilson, J. P., Feigin, M. E., Öhlund, D., . . . Tuveson, D. A. (2015). Organoid Models of Human and Mouse Ductal Pancreatic Cancer. *Cell, 160*(1), 324-338. https://doi.org/10.1016/j.cell.2014.12.021

Borad, M. J., Reddy, S. G., Bahary, N., Uronis, H. E., Sigal, D., Cohn, A. L., Schelman, W. R., Stephenson Jr, J., Chiorean, E. G., & Rosen, P. J. (2015). Randomized phase II trial of gemcitabine plus TH-302 versus gemcitabine in patients with advanced pancreatic cancer. *Journal of Clinical Oncology, 33*(13), 1475.

Bornstein, S., White, R., Malkoski, S., Oka, M., Han, G., Cleaver, T., Reh, D., Andersen, P., Gross, N., & Olson, S. (2009). Smad4 loss in mice causes spontaneous head and neck cancer with increased genomic instability and inflammation. *The Journal of Clinical Investigation, 119*(11), 3408-3419.

Bosco, M. C., Puppo, M., Santangelo, C., Anfosso, L., Pfeffer, U., Fardin, P., Battaglia, F., & Varesio, L. (2006). Hypoxia Modifies the Transcriptome of Primary Human Monocytes:

Modulation of Novel Immune-Related Genes and Identification Of CC-Chemokine Ligand 20 as a New Hypoxia-Inducible Gene. *The Journal of Immunology, 177*(3), 1941. 10.4049/jimmunol.177.3.1941

Brands, R. C., Knierim, L. M., De Donno, F., Steinacker, V., Hartmann, S., Seher, A., Kübler, A. C., & Müller-Richter, U. D. (2017). Targeting VEGFR and FGFR in head and neck squamous cell carcinoma in vitro. *Oncology Reports, 38*(3), 1877-1885.

Bredell, M. G., Ernst, J., El-Kochairi, I., Dahlem, Y., Ikenberg, K., & Schumann, D. M. (2016). Current relevance of hypoxia in head and neck cancer. *Oncotarget, 7*(31), 50781.

Brizel, D. M., Sibley, G. S., Prosnitz, L. R., Scher, R. L., & Dewhirst, M. W. (1997). Tumor hypoxia adversely affects the prognosis of carcinoma of the head and neck. *International Journal of Radiation Oncology, Biology, Physics, 38*(2), 285-289.

Brooks, J. M., Menezes, A. N., Ibrahim, M., Archer, L., Lal, N., Bagnall, C. J., Von Zeidler, S. V., Valentine, H. R., Spruce, R. J., & Batis, N. (2019). Development and Validation of a Combined Hypoxia and Immune Prognostic Classifier for Head and Neck CancerHypoxia-Immune Prognostic Classifier for HNC. *Clinical Cancer Research, 25*(17), 5315-5328.

Broutier, L., Mastrogiovanni, G., Verstegen, M. M., Francies, H. E., Gavarró, L. M., Bradshaw, C. R., Allen, G. E., Arnes-Benito, R., Sidorova, O., & Gaspersz, M. P. (2017). Human primary liver cancer–derived organoid cultures for disease modeling and drug screening. *Nature Medicine, 23*(12), 1424.

Brown, J. M., & Wilson, W. R. (2004). Exploiting tumour hypoxia in cancer treatment. *Nature Reviews Cancer, 4*(6), 437-447.

Buffa, F. M., Harris, A. L., West, C. M., & Miller, C. J. (2010). Large meta-analysis of multiple cancers reveals a common, compact and highly prognostic hypoxia metagene. *British Journal of Cancer, 102*(2), 428-435.

Burtness, B., Harrington, K. J., Greil, R., Soulières, D., Tahara, M., de Castro Jr, G., Psyrri, A., Basté, N., Neupane, P., & Bratland, Å. (2019). Pembrolizumab alone or with chemotherapy versus cetuximab with chemotherapy for recurrent or metastatic squamous cell carcinoma of the head and neck (KEYNOTE-048): a randomised, open-label, phase 3 study. *The Lancet, 394*(10212), 1915-1928.

Cai, E. Y., Garcia, J., Liu, Y., Vakar-Lopez, F., Arora, S., Nguyen, H. M., Lakely, B., Brown, L., Wong, A., & Montgomery, B. (2021). A bladder cancer patient-derived xenograft displays aggressive growth dynamics in vivo and in organoid culture. *Scientific Reports, 11*(1), 1-11.

Cancer Genome Atlas Network. (2015). Comprehensive genomic characterization of head and neck squamous cell carcinomas. *Nature, 517*(7536), 576.

Capeling, M. M., Huang, S., Childs, C. J., Wu, J. H., Tsai, Y., Wu, A., Garg, N., Holloway, E. M., Sundaram, N., & Bouffi, C. (2022). Suspension culture promotes serosal mesothelial development in human intestinal organoids. *Cell Reports, 38*(7), 110379.

Carmeliet, P., Dor, Y., Herbert, J., Fukumura, D., Brusselmans, K., Dewerchin, M., Neeman, M., Bono, F., Abramovitch, R., & Maxwell, P. (1998). Role of HIF-1α in hypoxia-mediated apoptosis, cell proliferation and tumour angiogenesis. *Nature, 394*(6692), 485-490.

Carreau, A., Hafny-Rahbi, B. E., Matejuk, A., Grillon, C., & Kieda, C. (2011). Why is the partial oxygen pressure of human tissues a crucial parameter? Small molecules and hypoxia. *Journal of Cellular and Molecular Medicine, 15*(6), 1239-1253.

Cassidy, J. W., Caldas, C., & Bruna, A. (2015). Maintaining tumor heterogeneity in patient-derived tumor xenografts. *Cancer Research, 75*(15), 2963-2968.

Chapman, J. D., Franko, A. J., & Sharplin, J. (1981). A marker for hypoxic cells in tumours with potential clinical applicability. *British Journal of Cancer, 43*(4), 546.

Chen, Z., Cheng, K., Walton, Z., Wang, Y., Ebi, H., Shimamura, T., Liu, Y., Tupper, T., Ouyang, J., & Li, J. (2012). A murine lung cancer co-clinical trial identifies genetic modifiers of therapeutic response. *Nature, 483*(7391), 613-617.

Chitneni, S. K., Palmer, G. M., Zalutsky, M. R., & Dewhirst, M. W. (2011). Molecular imaging of hypoxia. *Journal of Nuclear Medicine, 52*(2), 165-168.

Choi, H. G., Kim, J., Kim, K. H., Kim, K. H., Sung, M., Choe, J., Kim, J. E., & Jung, Y. H. (2015). Expression of hypoxic signaling markers in head and neck squamous cell carcinoma and its clinical significance. *European Archives of Oto-Rhino-Laryngology, 272*(1), 219-228.

Choi, S. Y. C., Lin, D., Gout, P. W., Collins, C. C., Xu, Y., & Wang, Y. (2014). Lessons from patient-derived xenografts for better in vitro modeling of human cancer. *Advanced Drug Delivery Reviews, 79*, 222-237.

Clohessy, J. G., & Pandolfi, P. P. (2015). Mouse hospital and co-clinical trial project—from bench to bedside. *Nature Reviews Clinical Oncology, 12*(8), 491-498.

Close, D. A., & Johnston, P. A. (2022). Detection and impact of hypoxic regions in multicellular tumor spheroid cultures formed by head and neck squamous cell carcinoma cells lines. *SLAS Discovery, 27*(1), 39-54.

Colevas, A. D., Yom, S. S., Pfister, D. G., Spencer, S., Adelstein, D., Adkins, D., Brizel, D. M., Burtness, B., Busse, P. M., & Caudell, J. J. (2018a). NCCN guidelines insights: head and neck cancers, version 1.2018. *Journal of the National Comprehensive Cancer Network, 16*(5), 479-490.

Collingridge, D. R., Young, W. K., Vojnovic, B., Wardman, P., Lynch, E. M., Hill, S. A., & Chaplin, D. J. (1997). Measurement of tumor oxygenation: a comparison between polarographic needle electrodes and a time-resolved luminescence-based optical sensor. *Radiation Research, 147*(3), 329-334.

Crowley, L. C., Marfell, B. J., & Waterhouse, N. J. (2016). Analyzing cell death by nuclear staining with Hoechst 33342. *Cold Spring Harbor Protocols, 2016*(9), pdb. prot087205.

Daniel, V. C., Marchionni, L., Hierman, J. S., Rhodes, J. T., Devereux, W. L., Rudin, C. M., Yung, R., Parmigiani, G., Dorsch, M., & Peacock, C. D. (2009). A primary xenograft model of small-cell lung cancer reveals irreversible changes in gene expression imposed by culture in vitro. *Cancer Research, 69*(8), 3364-3373.

Das, B., Tsuchida, R., Malkin, D., Koren, G., Baruchel, S., & Yeger, H. (2008). Hypoxia Enhances Tumor Stemness by Increasing the Invasive and Tumorigenic Side Population Fraction. *Stem Cells, 26*(7), 1818-1830.

Davidson, M. A., & Shanks, E. J. (2017). 3q26-29 Amplification in head and neck squamous cell carcinoma: a review of established and prospective oncogenes. *The FEBS Journal, 284*(17), 2705-2731.

De Jaeger, K., Kavanagh, M. C., & Hill, R. P. (2001). Relationship of hypoxia to metastatic ability in rodent tumours. *British Journal of Cancer, 84*(9), 1280-1285.

DeRose, Y. S., Wang, G., Lin, Y., Bernard, P. S., Buys, S. S., Ebbert, M. T., Factor, R., Matsen, C., Milash, B. A., & Nelson, E. (2011). Tumor grafts derived from women with breast cancer authentically reflect tumor pathology, growth, metastasis and disease outcomes. *Nature Medicine, 17*(11), 1514-1520.

Dewhirst, M. W., & Birer, S. R. (2016). Oxygen-Enhanced MRI Is a Major Advance in Tumor Hypoxia ImagingMajor Advance in Hypoxia Imaging. *Cancer Research, 76*(4), 769-772.

Dominijanni, A. J., Devarasetty, M., Forsythe, S. D., Votanopoulos, K. I., & Soker, S. (2021). Cell viability assays in three-dimensional hydrogels: a comparative study of accuracy. *Tissue Engineering Part C: Methods, 27*(7), 401-410.

Driehuis, E., Kolders, S., Spelier, S., Lõhmussaar, K., Willems, S. M., Devriese, L. A., de Bree, R., de Ruiter, E. J., Korving, J., & Begthel, H. (2019). Oral mucosal organoids as a potential platform for personalized cancer therapy. *Cancer Discovery, 9*(7), 852-871.

Driehuis, E., Kretzschmar, K., & Clevers, H. (2020). Establishment of patient-derived cancer organoids for drug-screening applications. *Nature Protocols, 15*(10), 3380-3409.

Duarte, S., Loubat, A., Momier, D., Topi, M., Faneca, H., Pedroso de Lima, Maria C, Carle, G. F., & Pierrefite-Carle, V. (2012). Isolation of head and neck squamous carcinoma cancer stem-like cells in a syngeneic mouse model and analysis of hypoxia effect. *Oncology Reports, 28*(3), 1057-1062.

Durand, R. E. (1994). The influence of microenvironmental factors during cancer therapy. *In Vivo (Athens, Greece), 8*(5), 691-702.

Ellinghaus, P., Ocker, M., Bender, S., Kneip, C., Ince, S., Joerger, M., & Schuler, M. (2017). Use of tumor mRNA expression for patient selection in a Phase I study of the pan-fibroblast growth factor receptor inhibitor BAY 1163877. *Cancer Research, 77*(13_Supplement), 3738.

Elrod, N. D., Jaworski, E. A., Ji, P., Wagner, E. J., & Routh, A. (2019). Development of Poly (A)-ClickSeq as a tool enabling simultaneous genome-wide poly (A)-site identification and differential expression analysis. *Methods, 155,* 20-29.

Eswaraka, J., & Giddabasappa, A. (2017). Humanized mice and PDX models. *Patient Derived Tumor Xenograft Models* (pp. 75-89). Elsevier.

Eustace, A., Mani, N., Span, P. N., Irlam, J. J., Taylor, J., Betts, G. N., Denley, H., Miller, C. J., Homer, J. J., & Rojas, A. M. (2013). A 26-Gene Hypoxia Signature Predicts Benefit from Hypoxia-Modifying Therapy in Laryngeal Cancer but Not Bladder CancerGene Signature Predicts Benefit from Antihypoxia Therapy. *Clinical Cancer Research, 19*(17), 4879-4888.

Facompre, N. D., Rajagopalan, P., Sahu, V., Pearson, A. T., Montone, K. T., James, C. D., Gleber-Netto, F., Weinstein, G. S., Jalaly, J., Lin, A., Rustgi, A. K., Nakagawa, H., Califano, J. A., Pickering, C. R., White, E. A., Windle, B. E., Morgan, I. M., Cohen, R. B., Gimotty, P. A., & Basu, D. (2020). Identifying predictors of HPV-related head and neck squamous cell carcinoma progression and survival through patient-derived models. *International Journal of Cancer, 147*(11), 3236-3249. https://doi.org/10.1002/ijc.33125

Fanchon, L. M., Russell, J., Pillarsetty, N., O'Donoghue, I., Gangangari, K., Yu, K. H., & Humm, J. L. (2020). Comparing the intra-tumoral distribution of Gemcitabine, 5-Fluorouracil, and Capecitabine in a murine model of pancreatic ductal adenocarcinoma. *PloS One, 15*(4), e0231745.

Farnebo, L., Shahangian, A., Lee, Y., Shin, J. H., Scheeren, F. A., & Sunwoo, J. B. (2015). Targeting Toll-like receptor 2 inhibits growth of head and neck squamous cell carcinoma. *Oncotarget*, *6*(12), 9897.

Favaro, E., Lord, S., Harris, A. L., & Buffa, F. M. (2011). Gene expression and hypoxia in breast cancer. *Genome Medicine, 3*(8), 1-12.

Fey, S. J., & Wrzesinski, K. (2012). Determination of drug toxicity using 3D spheroids constructed from an immortal human hepatocyte cell line. *Toxicological Sciences*, *127*(2), 403-411.

Fischer, A. H., Jacobson, K. A., Rose, J., & Zeller, R. (2008). Paraffin embedding tissue samples for sectioning. *CSH protocols*, *2008*, pdb-prot4989.

Fitzmaurice, C., Allen, C., Barber, R. M., Barregard, L., Bhutta, Z. A., Brenner, H., Dicker, D. J., Chimed-Orchir, O., Dandona, R., & Dandona, L. (2017). Global, regional, and national cancer incidence, mortality, years of life lost, years lived with disability, and disability-adjusted life-years for 32 cancer groups, 1990 to 2015: a systematic analysis for the global burden of disease study. *JAMA Oncology, 3*(4), 524-548.

Folaron, M., Merzianu, M., Duvvuri, U., Ferris, R. L., & Seshadri, M. (2019). Profiling the stromal and vascular heterogeneity in patient-derived xenograft models of head and neck cancer: Impact on therapeutic response. *Cancers, 11*(7), 951.

Forster, M. D., & Devlin, M. (2018). Immune checkpoint inhibition in head and neck cancer. *Frontiers in Oncology, 8*, 310.

Forsythe, S. D., Devarasetty, M., Shupe, T., Bishop, C., Atala, A., Soker, S., & Skardal, A. (2018). Environmental toxin screening using human-derived 3D bioengineered liver and cardiac organoids. *Frontiers in Public Health, 6*, 103.

Francies, H. E., Barthorpe, A., McLaren-Douglas, A., Barendt, W. J., & Garnett, M. J. (2016). Drug sensitivity assays of human cancer organoid cultures. *Organoids* (pp. 339-351). Springer.

Fu, Y., Nagy, J. A., Brown, L. F., Shih, S., Johnson, P. Y., Chan, C. K., Dvorak, H. F., & Wight, T. N. (2011). Proteolytic cleavage of versican and involvement of ADAMTS-1 in VEGF-A/VPF-induced pathological angiogenesis. *Journal of Histochemistry & Cytochemistry, 59*(5), 463-473.

Gabriel, J. A., Shams, M., & Orchard, G. E. (2021). Evaluation of different haematoxylin stain subtypes for the optimal microscopic interpretation of cutaneous malignancy in Mohs frozen section histological procedure. *British Journal of Biomedical Science, 78*(2), 78-86.

Ganjoo, K. N., Cranmer, L. D., Butrynski, J. E., Rushing, D., Adkins, D., Okuno, S. H., Lorente, G., Kroll, S., Langmuir, V. K., & Chawla, S. P. (2011). A phase I study of the safety and pharmacokinetics of the hypoxia-activated prodrug TH-302 in combination with doxorubicin in patients with advanced soft tissue sarcoma. *Oncology, 80*(1-2), 50-56.

Gantenbein-Ritter, B., Potier, E., Zeiter, S., van der Werf, M., Sprecher, C. M., & Ito, K. (2008). Accuracy of three techniques to determine cell viability in 3D tissues or scaffolds. *Tissue Engineering Part C: Methods, 14*(4), 353-358.

Gao, D., Vela, I., Sboner, A., Iaquinta, P. J., Karthaus, W. R., Gopalan, A., Dowling, C., Wanjala, J. N., Undvall, E. A., & Arora, V. K. (2014). Organoid cultures derived from patients with advanced prostate cancer. *Cell, 159*(1), 176-187.

Gómez, V., Mustapha, R., Ng, K., & Ng, T. (2020). Radiation therapy and the innate immune response: Clinical implications for immunotherapy approaches. *British Journal of Clinical Pharmacology, 86*(9), 1726-1735.

Graham, K., & Unger, E. (2018). Overcoming tumor hypoxia as a barrier to radiotherapy, chemotherapy and immunotherapy in cancer treatment. *International Journal of Nanomedicine, 13,* 6049.

Gray, L. H., Conger, A., Ebert, M., Hornsey, S., & Scott, O. (1953). The concentration of oxygen dissolved in tissues at the time of irradiation as a factor in radiotherapy. *The British Journal of Radiology, 26*(312), 638-648.

Grentzinger, T., Oberlin, S., Schott, G., Handler, D., Svozil, J., Barragan-Borrero, V., Humbert, A., Duharcourt, S., Brennecke, J., & Voinnet, O. (2020). A universal method for the rapid isolation of all known classes of functional silencing small RNAs. *Nucleic Acids Research, 48*(14), e79.

Griffiths, J. R., & Robinson, S. P. (1999). The OxyLite: a fibre-optic oxygen sensor. *The British Journal of Radiology, 72*(859), 627-630.

Guillen, K. P., Fujita, M., Butterfield, A. J., Scherer, S. D., Bailey, M. H., Chu, Z., DeRose, Y. S., Zhao, L., Cortes-Sanchez, E., & Yang, C. (2022). A human breast cancer-derived xenograft and organoid platform for drug discovery and precision oncology. *Nature Cancer, 3*(2), 232-250.

Guise, C. P., Abbattista, M. R., Singleton, R. S., Holford, S. D., Connolly, J., Dachs, G. U., ... & Patterson, A. V. (2010). The Bioreductive Prodrug PR-104A Is Activated under Aerobic Conditions by Human Aldo-Keto Reductase 1C3Aerobic Activation of PR-104A by AKR1C3. *Cancer Research*, *70*(4), 1573-1584.

Guo, W., Chen, X., Zhu, L., & Wang, Q. (2017). A six-mRNA signature model for the prognosis of head and neck squamous cell carcinoma. *Oncotarget, 8*(55), 94528.

Guttmann, D. M., Hart, L., Du, K., Seletsky, A., & Koumenis, C. (2013). Inhibition of Hsp27 radiosensitizes head-and-neck cancer by modulating deoxyribonucleic acid repair. *International Journal of Radiation Oncology* Biology* Physics, 87*(1), 168-175.

Hammond, E. M., Asselin, M., Forster, D., O'Connor, J. P., Senra, J. M., & Williams, K. J. (2014). The meaning, measurement and modification of hypoxia in the laboratory and the clinic. *Clinical Oncology, 26*(5), 277-288.

Hara, E., Smith, R., Parry, D., Tahara, H., Stone, S., & Peters, G. (1996). Regulation of p16CDKN2 expression and its implications for cell immortalization and senescence. *Molecular and Cellular Biology, 16*(3), 859-867.

Harms, J. K., Lee, T., Wang, T., Lai, A., Kee, D., Chaplin, J. M., McIvor, N. P., Hunter, F. W., Macann, A. M., & Wilson, W. R. (2019). Impact of tumour hypoxia on evofosfamide sensitivity in head and neck squamous cell carcinoma patient-derived xenograft models. *Cells, 8*(7), 717.

Harrington, K. J., Rischin, D., Greil, R., Soulieres, D., Tahara, M., Castro, G., Psyrri, A., Baste, N., Neupane, P. C., Bratland, Å, Fuereder, T., Hughes, B. G. M., Mesia, R., Ngamphaiboon, N., Rordorf, T., Wan Ishak, W. Z., Zhang, Y., Gumuscu, B., Swaby, R. F., & Burtness, B. (2020). KEYNOTE-048: Progression after the next line of therapy following pembrolizumab (P) or P plus chemotherapy (P+C) vs EXTREME (E) as first-line (1L) therapy for recurrent/metastatic (R/M) head and neck squamous cell carcinoma (HNSCC). *Jco, 38*(15), 6505. https://10.1200/JCO.2020.38.15_suppl.6505

Harris, B. H., Barberis, A., West, C. M., & Buffa, F. M. (2015). Gene expression signatures as biomarkers of tumour hypoxia. *Clinical Oncology, 27*(10), 547-560.

Hashibe, M., Brennan, P., Benhamou, S., Castellsague, X., Chen, C., Curado, M. P., Maso, L. D., Daudt, A. W., Fabianova, E., & Wünsch-Filho, V. (2007). Alcohol drinking in never users of tobacco, cigarette smoking in never drinkers, and the risk of head and neck cancer: pooled analysis in the International Head and Neck Cancer Epidemiology Consortium. *Journal of the National Cancer Institute, 99*(10), 777-789.

Henk, J. M., Bishop, K., & Shepherd, S. F. (2003). Treatment of head and neck cancer with CHART and nimorazole: phase II study. *Radiotherapy and Oncology, 66*(1), 65-70.

Hidalgo, M., Amant, F., Biankin, A. V., Budinská, E., Byrne, A. T., Caldas, C., Clarke, R. B., de Jong, S., Jonkers, J., & Mælandsmo, G. M. (2014). Patient-derived xenograft models: an emerging platform for translational cancer research. *Cancer Discovery, 4*(9), 998-1013.

Hill, S. J., Decker, B., Roberts, E. A., Horowitz, N. S., Muto, M. G., Worley, M. J., Feltmate, C. M., Nucci, M. R., Swisher, E. M., & Nguyen, H. (2018). Prediction of DNA repair inhibitor response in short-term patient-derived ovarian cancer organoids. *Cancer Discovery, 8*(11), 1404-1421.

Hill, R. M., Rocha, S., & Parsons, J. L. (2022). Overcoming the impact of hypoxia in driving radiotherapy resistance in head and neck squamous cell carcinoma. *Cancers, 14*(17), 4130.

Höckel, M., Schlenger, K., Knoop, C., & Vaupel, P. (1991). Oxygenation of carcinomas of the uterine cervix: evaluation by computerized O2 tension measurements. *Cancer Research, 51*(22), 6098-6102.

Hockel, M., & Vaupel, P. (2001). Tumor hypoxia: definitions and current clinical, biologic, and molecular aspects. *Journal of the National Cancer Institute, 93*(4), 266-276.

Hodgkiss, R. J., Webster, L., & Wilson, G. D. (1997). Measurement of Hypoxia in Vivo Using A 2-Nitromidazole (NITP). *Oxygen Transport to Tissue XIX* (pp. 61-67). Springer.

Hong, C. R., Dickson, B. D., Jaiswal, J. K., Pruijn, F. B., Hunter, F. W., Hay, M. P., Hicks, K. O., & Wilson, W. R. (2018). Cellular pharmacology of evofosfamide (TH-302): A critical reevaluation of its bystander effects. *Biochemical Pharmacology, 156*, 265-280. https://doi.org/10.1016/j.bcp.2018.08.027

Hou, S., Tiriac, H., Sridharan, B. P., Scampavia, L., Madoux, F., Seldin, J., Souza, G. R., Watson, D., Tuveson, D., & Spicer, T. P. (2018). Advanced development of primary pancreatic organoid tumor models for high-throughput phenotypic drug screening. *SLAS DISCOVERY: Advancing Life Sciences R&D, 23*(6), 574-584.

Huang, L., Bockorny, B., Paul, I., Akshinthala, D., Frappart, P., Gandarilla, O., Bose, A., Sanchez-Gonzalez, V., Rouse, E. E., & Lehoux, S. D. (2020). PDX-derived organoids model in vivo drug response and secrete biomarkers. *JCI Insight, 5*(21)

Hubert, C. G., Rivera, M., Spangler, L. C., Wu, Q., Mack, S. C., Prager, B. C., Couce, M., McLendon, R. E., Sloan, A. E., & Rich, J. N. (2016). A three-dimensional organoid culture system derived from human glioblastomas recapitulates the hypoxic gradients and cancer stem cell heterogeneity of tumors found in vivo. *Cancer Research*, *76*(8), 2465-2477.

Itoh, K., Wakabayashi, N., Katoh, Y., Ishii, T., Igarashi, K., Engel, J. D., & Yamamoto, M. (1999). Keap1 represses nuclear activation of antioxidant responsive elements by Nrf2 through binding to the amino-terminal Neh2 domain. *Genes & Development, 13*(1), 76-86.

Izumchenko, E., Paz, K., Ciznadija, D., Sloma, I., Katz, A., Vasquez-Dunddel, D., Ben-Zvi, I., Stebbing, J., McGuire, W., & Harris, W. (2017). Patient-derived xenografts effectively capture responses to oncology therapy in a heterogeneous cohort of patients with solid tumors. *Annals of Oncology, 28*(10), 2595-2605.

Jackson, R. K., Liew, L. P., & Hay, M. P. (2019). Overcoming radioresistance: small molecule radiosensitisers and hypoxia-activated prodrugs. *Clinical Oncology*, *31*(5), 290-302.

Jacob, F., Salinas, R. D., Zhang, D. Y., Nguyen, P. T., Schnoll, J. G., Wong, S. Z. H., Thokala, R., Sheikh, S., Saxena, D., & Prokop, S. (2020). A patient-derived glioblastoma organoid model and biobank recapitulates inter-and intra-tumoral heterogeneity. *Cell, 180*(1), 188-204. e22.

Jacquemin, G., Wurmser, A., Huyghe, M., Sun, W., Homayed, Z., Merle, C., Perkins, M., Qasrawi, F., Richon, S., & Dingli, F. (2022). Paracrine signalling between intestinal epithelial and tumour cells induces a regenerative programme. *Elife, 11*, e76541.

Jamieson, S. M., Tsai, P., Kondratyev, M. K., Budhani, P., Liu, A., Senzer, N. N., Chiorean, E. G., Jalal, S. I., Nemunaitis, J. J., & Kee, D. (2018). Evofosfamide for the treatment of human papillomavirus-negative head and neck squamous cell carcinoma. *JCI Insight, 3*(16)

Jayaprakash, P., Ai, M., Liu, A., Budhani, P., Bartkowiak, T., Sheng, J., Ager, C., Nicholas, C., Jaiswal, A. R., & Sun, Y. (2018). Targeted hypoxia reduction restores T cell infiltration and sensitizes prostate cancer to immunotherapy. *The Journal of Clinical Investigation, 128*(11), 5137-5149.

Jenkins, W. T., Evans, S. M., & Koch, C. J. (2000). Hypoxia and necrosis in rat 9L glioma and Morris 7777 hepatoma tumors: comparative measurements using EF5 binding and the

Eppendorf needle electrode. *International Journal of Radiation Oncology* Biology* Physics*, *46*(4), 1005-1017.

Jin, C., Bai, L., Wu, H., Tian, F., & Guo, G. (2007). Radiosensitization of paclitaxel, etanidazole and paclitaxel etanidazole nanoparticles on hypoxic human tumor cells in vitro. *Biomaterials, 28*(25), 3724-3730.

Job, S., de Reyniès, A., Heller, B., Weiss, A., Guérin, E., Macabre, C., Ledrappier, S., Bour, C., Wasylyk, C., & Etienne-Selloum, N. (2019). Preferential response of basal-like head and neck squamous cell carcinoma cell lines to EGFR-targeted therapy depending on EREG-driven oncogenic addiction. *Cancers, 11*(6), 795.

Jögi, A., Vallon-Christersson, J., Holmquist, L., Axelson, H., Borg, Å, & Påhlman, S. (2004). Human neuroblastoma cells exposed to hypoxia: induction of genes associated with growth, survival, and aggressive behavior. *Experimental Cell Research*, *295*(2), 469-487.

Johnson, J. I., Decker, S., Zaharevitz, D., Rubinstein, L. V., Venditti, J. M., Schepartz, S., ... & Sausville, E. A. (2001). Relationships between drug activity in NCI preclinical in vitro and in vivo models and early clinical trials. *British Journal of Cancer*, *84*(10), 1424-1431.

Joshua, B., Kaplan, M. J., Doweck, I., Pai, R., Weissman, I. L., Prince, M. E., & Ailles, L. E. (2012). Frequency of cells expressing CD44, a Head and Neck cancer stem cell marker: Correlation with tumor aggressiveness. *Head & Neck*, *34*(1), 42-49. https://doi.org/10.1002/hed.21699

Jung, K., Kang, H., & Mehra, R. (2018). Targeting phosphoinositide 3-kinase (PI3K) in head and neck squamous cell carcinoma (HNSCC). *Cancers of the Head & Neck*, *3*(1), 1-13.

Kaanders, J. H., Wijffels, K. I., Marres, H. A., Ljungkvist, A. S., Pop, L. A., van den Hoogen, Franciscus JA, de Wilde, P. C., Bussink, J., Raleigh, J. A., & van der Kogel, Albert J. (2002). Pimonidazole binding and tumor vascularity predict for treatment outcome in head and neck cancer. *Cancer Research, 62*(23), 7066-7074.

Kang, H. N., Kim, J., Park, A., Choi, J. W., Lim, S. M., Kim, J., Shin, E. J., Hong, M. H., Pyo, K., & Yun, M. R. (2020). Establishment and characterization of patient-derived xenografts as paraclinical models for head and neck cancer. *BMC Cancer*, *20*, 1-12.

Karabajakian, A., Gau, M., Reverdy, T., Neidhardt, E., & Fayette, J. (2019). Induction chemotherapy in head and neck squamous cell carcinoma: a question of belief. *Cancers, 11*(1), 15.

Karakasheva, T. A., Kijima, T., Shimonosono, M., Maekawa, H., Sahu, V., Gabre, J. T., Cruz-Acuña, R., Giroux, V., Sangwan, V., & Whelan, K. A. (2020). Generation and characterization of patient-derived head and neck, oral, and esophageal cancer organoids. *Current Protocols in Stem Cell Biology, 53*(1), e109.

Karamboulas, C., Bruce, J. P., Hope, A. J., Meens, J., Huang, S. H., Erdmann, N., Hyatt, E., Pereira, K., Goldstein, D. P., & Weinreb, I. (2018). Patient-derived xenografts for prognostication and personalized treatment for head and neck squamous cell carcinoma. *Cell Reports, 25*(5), 1318-1331. e4.

Kaushik, G., Kamineny, P., & Wesa, A. (2021). Unique 3D organoids autologous TIL coculture platform enables high throughput immune-oncology drug response studies. *Cancer Research, 81*(13_Supplement), 2978.

Kennedy, A. S., Raleigh, J. A., Perez, G. M., Calkins, D. P., Thrall, D. E., Novotny, D. B., & Varia, M. A. (1997). Proliferation and hypoxia in human squamous cell carcinoma of the cervix: first report of combined immunohistochemical assays. *International Journal of Radiation Oncology, Biology, Physics, 37*(4), 897-905.

Kersten, K., de Visser, K. E., van Miltenburg, M. H., & Jonkers, J. (2017). Genetically engineered mouse models in oncology research and cancer medicine. *EMBO Molecular Medicine, 9*(2), 137-153.

Kiernan, J. A. (2018). Does progressive nuclear staining with hemalum (alum hematoxylin) involve DNA, and what is the nature of the dye-chromatin complex? *Biotechnic & Histochemistry, 93*(2), 133-148.

Kim, Y., Nam, H. J., Lee, J., Kim, C., Yu, Y. S., Kim, D., Park, S. W., Bhin, J., Hwang, D., & Lee, H. (2016). Methylation-dependent regulation of HIF-1α stability restricts retinal and tumour angiogenesis. *Nature Communications, 7*(1), 1-14.

Kishimoto, S., Brender, J. R., Chandramouli, G. V., Saida, Y., Yamamoto, K., Mitchell, J. B., & Krishna, M. C. (2021). Hypoxia-activated prodrug evofosfamide treatment in pancreatic ductal adenocarcinoma xenografts alters the tumor redox status to potentiate radiotherapy. *Antioxidants & Redox Signaling, 35*(11), 904-915.

Klein, J. D., & Grandis, J. R. (2010). The molecular pathogenesis of head and neck cancer. *Cancer biology & therapy*, *9*(1), 1-7.

Kobayashi, A., Kang, M., Okawa, H., Ohtsuji, M., Zenke, Y., Chiba, T., Igarashi, K., & Yamamoto, M. (2004). Oxidative stress sensor Keap1 functions as an adaptor for Cul3-based E3 ligase to regulate proteasomal degradation of Nrf2. *Molecular and Cellular Biology, 24*(16), 7130-7139.

Konopleva, M., Thall, P. F., Yi, C. A., Borthakur, G., Coveler, A., Bueso-Ramos, C., Benito, J., Konoplev, S., Gu, Y., & Ravandi, F. (2015). Phase I/II study of the hypoxia-activated prodrug PR104 in refractory/relapsed acute myeloid leukemia and acute lymphoblastic leukemia. *Haematologica, 100*(7), 927.

Koong, A. C., Denko, N. C., Hudson, K. M., Schindler, C., Swiersz, L., Koch, C., Evans, S., Ibrahim, H., Le, Q. T., & Terris, D. J. (2000). Candidate genes for the hypoxic tumor phenotype. *Cancer Research, 60*(4), 883-887.

Köpf-Maier, P., & Mühlhausen, S. K. (1992). Changes in the cytoskeleton pattern of tumor cells by cisplatin in vitro. *Chemico-Biological Interactions, 82*(3), 295-316.

Kopper, O., de Witte, C. J., Lõhmussaar, K., Valle-Inclan, J. E., Hami, N., Kester, L., Balgobind, A. V., Korving, J., Proost, N., & Begthel, H. (2019). An organoid platform for ovarian cancer captures intra-and interpatient heterogeneity. *Nature Medicine, 25*(5), 838-849.

Kreso, A., O'Brien, C. A., Van Galen, P., Gan, O. I., Notta, F., Brown, A. M., Ng, K., Ma, J., Wienholds, E., & Dunant, C. (2013). Variable clonal repopulation dynamics influence chemotherapy response in colorectal cancer. *Science, 339*(6119), 543-548.

Lahin, A., Emily, B., Matthew, S., Joshua, S., & Chad, B. (2019). Expression of P53 and Prognosis in Patients with Head and Neck Squamous Cell Carcinoma (HNSCC). *Int J Cancer Clin Res, 6*, 122.

Lee, B. E., Lee, B. J., Lee, K. J., Lee, M., Lim, Y. J., Choi, J. K., & Keum, B. (2022). A simple and efficient cryopreservation method for mouse small intestinal and colon organoids for regenerative medicine. *Biochemical and Biophysical Research Communications*, *595*, 14-21.

Lee, S. H., Hu, W., Matulay, J. T., Silva, M. V., Owczarek, T. B., Kim, K., Chua, C. W., Barlow, L. J., Kandoth, C., & Williams, A. B. (2018). Tumor evolution and drug response in patient-derived organoid models of bladder cancer. *Cell*, *173*(2), 515-528. e17.

Lee, T. W., Lai, A., Harms, J. K., Singleton, D. C., Dickson, B. D., Macann, A. M., Hay, M. P., & Jamieson, S. M. (2020). Patient-Derived Xenograft and Organoid Models for Precision Medicine Targeting of the Tumour Microenvironment in Head and Neck Cancer. *Cancers*, *12*(12), 3743.

Leemans, C. R., Snijders, P. J., & Brakenhoff, R. H. (2018). The molecular landscape of head and neck cancer. *Nature Reviews Cancer*, *18*(5), 269.

Levine, A. J. (2019). The many faces of p53: something for everyone. *Journal of Molecular Cell Biology*, *11*(7), 524-530.

Li, W., & Shen, M. M. (2021). Prostate cancer cell heterogeneity and plasticity: insights from studies of genetically-engineered mouse models. Paper presented at the *Seminars in Cancer Biology*.

Li, Y., Zhao, L., & Li, X. F. (2021a). Targeting hypoxia: hypoxia-activated prodrugs in cancer therapy. *Frontiers in Oncology*, 2920.

Li, Z., Yu, L., Chen, D., Meng, Z., Chen, W., & Huang, W. (2021b). Protocol for generation of lung adenocarcinoma organoids from clinical samples. *STAR Protocols*, *2*(1), 100239. https://doi.org/10.1016/j.xpro.2020.100239

Lin, D., Wyatt, A. W., Xue, H., Wang, Y., Dong, X., Haegert, A., Wu, R., Brahmbhatt, S., Mo, F., & Jong, L. (2014). High Fidelity Patient-Derived Xenografts for Accelerating Prostate Cancer Discovery and Drug DevelopmentNext-Generation Models of Prostate Cancer. *Cancer Research*, *74*(4), 1272-1283.

Liu, H., Zhang, Y., Zhang, Y., Li, Y., Hua, Z., Zhang, C., Wu, K., Yu, F., Zhang, Y., & Su, J. (2020). Human embryonic stem cell-derived organoid retinoblastoma reveals a cancerous origin. *Proceedings of the National Academy of Sciences, 117*(52), 33628-33638.

Ljungkvist, A. S., Bussink, J., Rijken, P. F., Kaanders, J. H., van der Kogel, Albert J, & Denekamp, J. (2002). Vascular architecture, hypoxia, and proliferation in first-generation xenografts of human head-and-neck squamous cell carcinomas. *International Journal of Radiation Oncology, Biology, Physics, 54*(1), 215-228.

Lo, Y., Karlsson, K., & Kuo, C. J. (2020). Applications of organoids for cancer biology and precision medicine. *Nature Cancer, 1*(8), 761-773. 10.1038/s43018-020-0102-y

Lohse, I., Rasowski, J., Cao, P., Pintilie, M., Do, T., Tsao, M., Hill, R. P., & Hedley, D. W. (2016). Targeting hypoxic microenvironment of pancreatic xenografts with the hypoxia-activated prodrug TH-302. *Oncotarget, 7*(23), 33571.

Lunardi, A., Ala, U., Epping, M. T., Salmena, L., Clohessy, J. G., Webster, K. A., Wang, G., Mazzucchelli, R., Bianconi, M., & Stack, E. C. (2013). A co-clinical approach identifies mechanisms and potential therapies for androgen deprivation resistance in prostate cancer. *Nature Genetics, 45*(7), 747-755.

Lynggaard, C. D., Therkildsen, M. H., Kristensen, C. A., & Specht, L. (2015). The EXTREME regimen for recurrent/metastatic head and neck squamous cell carcinoma (R/M HNSCC): Treatment outcome in a single institution cohort. *Null, 54*(7), 1071-1075.

Mahiddine, K., Blaisdell, A., Ma, S., Créquer-Grandhomme, A., Lowell, C. A., & Erlebacher, A. (2020). Relief of tumor hypoxia unleashes the tumoricidal potential of neutrophils. *The Journal of Clinical Investigation, 130*(1), 389-403.

Marur, S., & Forastiere, A. A. (2016). Head and neck squamous cell carcinoma: update on epidemiology, diagnosis, and treatment. Paper presented at the *Mayo Clinic Proceedings, 91*(3) 386-396.

Mason, R. P., Antich, P. P., Babcock, E. E., Constantinescu, A., Peschke, P., & Hahn, E. W. (1994). Non-invasive determination of tumor oxygen tension and local variation with growth. *International Journal of Radiation Oncology, Biology, Physics, 29*(1), 95-103.

Matsuzawa-Ishimoto, Y. U., Hine, A., Shono, Y., Rudensky, E., Lazrak, A., Yeung, F., Neil, J. A., Yao, X., Chen, Y., & Heaney, T. (2020). An intestinal organoid–based platform that recreates susceptibility to T-cell–mediated tissue injury. *Blood, 135*(26), 2388-2401.

McCoy, C. L., McIntyre, D. J., Robinson, S. P., Aboagye, E. O., & Griffiths, J. R. (1996). Magnetic resonance spectroscopy and imaging methods for measuring tumour and tissue oxygenation. *The British Journal of Cancer.Supplement, 27*, S226.

McDermott, J. D., & Bowles, D. W. (2019). Epidemiology of head and neck squamous cell carcinomas: impact on staging and prevention strategies. *Current Treatment Options in Oncology, 20*(5), 1-13.

McDougall, S. R., Anderson, A. R., & Chaplain, M. A. (2006). Mathematical modelling of dynamic adaptive tumour-induced angiogenesis: clinical implications and therapeutic targeting strategies. *Journal of Theoretical Biology, 241*(3), 564-589.

McKeown, S. R. (2014). Defining normoxia, physoxia and hypoxia in tumours—implications for treatment response. *The British Journal of Radiology, 87*(1035), 20130676.

Mehra, R., Seiwert, T. Y., Gupta, S., Weiss, J., Gluck, I., Eder, J. P., Burtness, B., Tahara, M., Keam, B., & Kang, H. (2018). Efficacy and safety of pembrolizumab in recurrent/metastatic head and neck squamous cell carcinoma: pooled analyses after long-term follow-up in KEYNOTE-012. *British Journal of Cancer, 119*(2), 153-159.

Melissaridou, S., Wiechec, E., Magan, M., Jain, M. V., Chung, M. K., Farnebo, L., & Roberg, K. (2019). The effect of 2D and 3D cell cultures on treatment response, EMT profile and stem cell features in head and neck cancer. *Cancer Cell International, 19*(1), 1-10.

Melsens, E., De Vlieghere, E., Descamps, B., Vanhove, C., Kersemans, K., De Vos, F., Goethals, I., Brans, B., De Wever, O., & Ceelen, W. (2018). Hypoxia imaging with 18F-FAZA PET/CT predicts radiotherapy response in esophageal adenocarcinoma xenografts. *Radiation Oncology, 13*(1), 1-8.

Metwally, M. A. H., Frederiksen, K. D., & Overgaard, J. (2014). Compliance and toxicity of the hypoxic radiosensitizer nimorazole in the treatment of patients with head and neck squamous cell carcinoma (HNSCC). *Null, 53*(5), 654-661. 10.3109/0284186X.2013.864050

Minhinnick, A., Aye, P. S., Elwood, J. M., & McKeage, M. J. (2022). Cancer of the nasopharynx in Aotearoa New Zealand from 1994 to 2018: Incidence and survival in a population-based, national registry cohort study. *The Lancet Regional Health-Western Pacific*, *24*, 100522.

Mirabello, V., Cortezon-Tamarit, F., & Pascu, S. I. (2018). Oxygen sensing, hypoxia tracing and in vivo imaging with functional metalloprobes for the early detection of non-communicable diseases. *Frontiers in Chemistry, 6*, 27.

Mistry, I. N., Thomas, M., Calder, E. D., Conway, S. J., & Hammond, E. M. (2017). Clinical advances of hypoxia-activated prodrugs in combination with radiation therapy. *International Journal of Radiation Oncology, Biology, Physics, 98*(5), 1183-1196.

Morgan, R. A. (2012). Human tumor xenografts: the good, the bad, and the ugly. *Molecular Therapy, 20*(5), 882-884.

Mosely, S. I., Prime, J. E., Sainson, R. C., Koopmann, J., Wang, D. Y., Greenawalt, D. M., Ahdesmaki, M. J., Leyland, R., Mullins, S., & Pacelli, L. (2017). Rational Selection of Syngeneic Preclinical Tumor Models for Immunotherapeutic Drug DiscoveryCharacterization of Murine Syngeneic Tumor Models. *Cancer Immunology Research, 5*(1), 29-41.

Mueller, A., Odze, R., Jenkins, T. D., Shahsesfaei, A., Nakagawa, H., Inomoto, T., & Rustgi, A. K. (1997). A transgenic mouse model with cyclin D1 overexpression results in cell cycle, epidermal growth factor receptor, and p53 abnormalities. *Cancer Research, 57*(24), 5542-5549.

Muz, B., de la Puente, P., Azab, F., & Azab, A. K. (2015). The role of hypoxia in cancer progression, angiogenesis, metastasis, and resistance to therapy. *Hypoxia, 3*, 83.

Muz, B., Kusdono, H. D., Azab, F., de la Puente, P., Federico, C., Fiala, M., Vij, R., Salama, N. N., & Azab, A. K. (2017). Tariquidar sensitizes multiple myeloma cells to proteasome inhibitors via reduction of hypoxia-induced P-gp-mediated drug resistance. *Leukemia & Lymphoma, 58*(12), 2916-2925.

Nagaya, T., Nakamura, Y., Okuyama, S., Ogata, F., Maruoka, Y., Choyke, P. L., Allen, C., & Kobayashi, H. (2017). Syngeneic Mouse Models of Oral Cancer Are Effectively Targeted by

Anti–CD44-Based NIR-PITCD44 Targeted NIR-PIT in OSCC Models. *Molecular Cancer Research, 15*(12), 1667-1677.

Noman, M. Z., Hasmim, M., Messai, Y., Terry, S., Kieda, C., Janji, B., & Chouaib, S. (2015). Hypoxia: a key player in antitumor immune response. A review in the theme: cellular responses to hypoxia. *American Journal of Physiology-Cell Physiology, 309*(9), C569-C579.

Noman, M. Z., Messai, Y., Carre, T., Akalay, I., Meron, M., Janji, B., Hasmim, M., & Chouaib, S. (2011). Microenvironmental hypoxia orchestrating the cell stroma cross talk, tumor progression and antitumor response. *Critical Reviews™ in Immunology, 31*(5)

Nordsmark, M., Bentzen, S. M., Rudat, V., Brizel, D., Lartigau, E., Stadler, P., Becker, A., Adam, M., Molls, M., & Dunst, J. (2005). Prognostic value of tumor oxygenation in 397 head and neck tumors after primary radiation therapy. An international multi-center study. *Radiotherapy and Oncology, 77*(1), 18-24.

Nunn, A., Linder, K., & Strauss, H. W. (1995). Nitroimidazoles and imaging hypoxia. *European Journal of Nuclear Medicine, 22*(3), 265-280.

O'Connor, J. P., Boult, J. K., Jamin, Y., Babur, M., Finegan, K. G., Williams, K. J., Little, R. A., Jackson, A., Parker, G. J., & Reynolds, A. R. (2016a). Oxygen-Enhanced MRI Accurately Identifies, Quantifies, and Maps Tumor Hypoxia in Preclinical Cancer ModelsImaging Tumor Hypoxia In Vivo with Oxygen-Enhanced MRI. *Cancer Research, 76*(4), 787-795.

O'Connor, J. P., Jackson, A., Parker, G. J., Roberts, C., & Jayson, G. C. (2012). Dynamic contrast-enhanced MRI in clinical trials of antivascular therapies. *Nature Reviews Clinical Oncology, 9*(3), 167-177.

O'Connor, J. P., Robinson, S. P., & Waterton, J. C. (2019). Imaging tumour hypoxia with oxygen-enhanced MRI and BOLD MRI. *The British Journal of Radiology, 92*(1096), 20180642.

O'Connor, L. J., Cazares-Körner, C., Saha, J., Evans, C. N., Stratford, M. R., Hammond, E. M., & Conway, S. J. (2016b). Design, synthesis and evaluation of molecularly targeted hypoxia-activated prodrugs. *Nature Protocols, 11*(4), 781-794.

Okada, S., Vaeteewoottacharn, K., & Kariya, R. (2019). Application of highly immunocompromised mice for the establishment of patient-derived xenograft (PDX) models. *Cells, 8*(8), 889.

Ooft, S. N., Weeber, F., Dijkstra, K. K., McLean, C. M., Kaing, S., van Werkhoven, E., Schipper, L., Hoes, L., Vis, D. J., & van de Haar, J. (2019). Patient-derived organoids can predict response to chemotherapy in metastatic colorectal cancer patients. *Science Translational Medicine, 11*(513)

Ouchi, R., Togo, S., Kimura, M., Shinozawa, T., Koido, M., Koike, H., Thompson, W., Karns, R. A., Mayhew, C. N., & McGrath, P. S. (2019). Modeling steatohepatitis in humans with pluripotent stem cell-derived organoids. *Cell Metabolism, 30*(2), 374-384. e6.

Overgaard, J. (2011). Hypoxic modification of radiotherapy in squamous cell carcinoma of the head and neck–a systematic review and meta-analysis. *Radiotherapy and Oncology, 100*(1), 22-32.

Patterson, A. V., Ferry, D. M., Edmunds, S. J., Gu, Y., Singleton, R. S., Patel, K., Pullen, S. M., Hicks, K. O., Syddall, S. P., & Atwell, G. J. (2007). Mechanism of action and preclinical antitumor activity of the novel hypoxia-activated DNA cross-linking agent PR-104. *Clinical Cancer Research, 13*(13), 3922-3932.

Peerlings, J., Van De Voorde, L., Mitea, C., Larue, R., Yaromina, A., Sandeleanu, S., Spiegelberg, L., Dubois, L., Lambin, P., & Mottaghy, F. M. (2017). Hypoxia and hypoxia response-associated molecular markers in esophageal cancer: A systematic review. *Methods, 130*, 51-62.

Peeters, S. G., Zegers, C. M., Yaromina, A., Van Elmpt, W., Dubois, L., & Lambin, P. (2015). Current preclinical and clinical applications of hypoxia PET imaging using 2-nitroimidazoles. *QJ Nucl Med Mol Imaging, 59*(1), 39-57.

Peng, S., Creighton, C. J., Zhang, Y., Sen, B., Mazumdar, T., Myers, J. N., Woolfson, A., Lorenzi, M. V., Bell, D., Williams, M. D., & Johnson, F. M. (2013). Tumor grafts derived from patients with head and neck squamous carcinoma authentically maintain the molecular and histologic characteristics of human cancers. *Journal of Translational Medicine, 11*(1), 198.

Peters, D. G., Ning, W., Chu, T. J., Li, C. J., & Choi, A. M. (2006). Comparative SAGE analysis of the response to hypoxia in human pulmonary and aortic endothelial cells. *Physiological Genomics, 26*(2), 99-108.

Platt, R. J., Chen, S., Zhou, Y., Yim, M. J., Swiech, L., Kempton, H. R., Dahlman, J. E., Parnas, O., Eisenhaure, T. M., & Jovanovic, M. (2014). CRISPR-Cas9 knockin mice for genome editing and cancer modeling. *Cell, 159*(2), 440-455.

Prahallad, A., Sun, C., Huang, S., Di Nicolantonio, F., Salazar, R., Zecchin, D., Beijersbergen, R. L., Bardelli, A., & Bernards, R. (2012). Unresponsiveness of colon cancer to BRAF (V600E) inhibition through feedback activation of EGFR. *Nature, 483*(7387), 100-103.

Premsrirut, P. K., Dow, L. E., Kim, S. Y., Camiolo, M., Malone, C. D., Miething, C., Scuoppo, C., Zuber, J., Dickins, R. A., & Kogan, S. C. (2011). A rapid and scalable system for studying gene function in mice using conditional RNA interference. *Cell, 145*(1), 145-158.

Price, S., Bhosle, S., Gonçalves, E., Li, X., McClurg, D. P., Barthorpe, S., Beck, A., Hall, C., Lightfoot, H., & Farrow, L. (2022). A suspension technique for efficient large-scale cancer organoid culturing and perturbation screens. *Scientific Reports, 12*(1), 1-11.

Ragnum, H. B., Vlatkovic, L., Lie, A. K., Axcrona, K., Julin, C. H., Frikstad, K. M., Hole, K. H., Seierstad, T., & Lyng, H. (2015). The tumour hypoxia marker pimonidazole reflects a transcriptional programme associated with aggressive prostate cancer. *British Journal of Cancer, 112*(2), 382-390.

Raikwar, S. P., Kim, E., Sivitz, W. I., Allamargot, C., Thedens, D. R., & Zavazava, N. (2015). Human iPS cell-derived insulin producing cells form vascularized organoids under the kidney capsules of diabetic mice. *PloS One, 10*(1), e0116582.

Raleigh, J. A., Calkins-Adams, D. P., Rinker, L. H., Ballenger, C. A., Weissler, M. C., Fowler Jr, W. C., Novotny, D. B., & Varia, M. A. (1998). Hypoxia and vascular endothelial growth factor expression in human squamous cell carcinomas using pimonidazole as a hypoxia marker. *Cancer Research, 58*(17), 3765-3768.

Ramamoorthy, P., Thomas, S. M., Kaushik, G., Subramaniam, D., Chastain, K. M., Dhar, A., Tawfik, O., Kasi, A., Sun, W., & Ramalingam, S. (2019). Metastatic tumor-in-a-dish, a novel multicellular organoid to study lung colonization and predict therapeutic response. *Cancer Research, 79*(7), 1681-1695.

Risbridger, G. P., Taylor, R. A., Clouston, D., Sliwinski, A., Thorne, H., Hunter, S., Li, J., Mitchell, G., Murphy, D., & Frydenberg, M. (2015). Patient-derived xenografts reveal that intraductal carcinoma of the prostate is a prominent pathology in BRCA2 mutation carriers with prostate cancer and correlates with poor prognosis. *European Urology, 67*(3), 496-503.

Robinson, S. P., Collingridge, D. R., Howe, F. A., Rodrigues, L. M., Chaplin, D. J., & Griffiths, J. R. (1999). Tumour response to hypercapnia and hyperoxia monitored by FLOOD magnetic resonance imaging. *NMR in Biomedicine, 12*(2), 98-106.

Rongvaux, A., Willinger, T., Takizawa, H., Rathinam, C., Auerbach, W., Murphy, A. J., Valenzuela, D. M., Yancopoulos, G. D., Eynon, E. E., & Stevens, S. (2011). Human thrombopoietin knockin mice efficiently support human hematopoiesis in vivo. *Proceedings of the National Academy of Sciences, 108*(6), 2378-2383.

Routh, A., Ji, P., Jaworski, E., Xia, Z., Li, W., & Wagner, E. J. (2017). Poly (A)-ClickSeq: click-chemistry for next-generation 3´-end sequencing without RNA enrichment or fragmentation. *Nucleic Acids Research, 45*(12), e112.

Ruicci, K. M., Meens, J., Sun, R. X., Rizzo, G., Pinto, N., Yoo, J., Fung, K., MacNeil, D., Mymryk, J. S., & Barrett, J. W. (2019). A controlled trial of HNSCC patient-derived xenografts reveals broad efficacy of PI3Kα inhibition in controlling tumor growth. *International Journal of Cancer, 145*(8), 2100-2106.

Ruscetti, M., Morris IV, J. P., Mezzadra, R., Russell, J., Leibold, J., Romesser, P. B., Simon, J., Kulick, A., Ho, Y., & Fennell, M. (2020). Senescence-induced vascular remodeling creates therapeutic vulnerabilities in pancreas cancer. *Cell, 181*(2), 424-441. e21.

Sachs, N., & Clevers, H. (2014). Organoid cultures for the analysis of cancer phenotypes. *Current Opinion in Genetics & Development, 24*, 68-73.

Sachs, N., de Ligt, J., Kopper, O., Gogola, E., Bounova, G., Weeber, F., Balgobind, A. V., Wind, K., Gracanin, A., & Begthel, H. (2018). A living biobank of breast cancer organoids captures disease heterogeneity. *Cell, 172*(1-2), 373-386. e10.

Saleh, K., Eid, R., Haddad, F. G., Khalife-Saleh, N., & Kourie, H. R. (2018). New developments in the management of head and neck cancer–impact of pembrolizumab. *Therapeutics and Clinical Risk Management, 14,* 295.

Salem, A., Little, R. A., Latif, A., Featherstone, A. K., Babur, M., Peset, I., Cheung, S., Watson, Y., Tessyman, V., & Mistry, H. (2019). Oxygen-enhanced MRI is feasible, repeatable, and detects radiotherapy-induced change in hypoxia in Xenograft models and in patients with non–small cell lung Cancer. *Clinical Cancer Research, 25*(13), 3818-3829.

Sanduleanu, S., Hamming-Vrieze, O., Wesseling, F. W., Even, A. J., Hoebers, F. J., Hoeben, A., Vogel, W. V., Tesselaar, M. E., Parvin, D., & Bartelink, H. (2020). [18F]-HX4 PET/CT hypoxia in patients with squamous cell carcinoma of the head and neck treated with chemoradiotherapy: Prognostic results from two prospective trials. *Clinical and Translational Radiation Oncology, 23,* 9-15.

Sano, D., & Myers, J. N. (2009). Xenograft models of head and neck cancers. *Head & Neck Oncology, 1*(1), 1-6.

Schreiber, K., Cannon, R. E., Karrison, T., Beck-Engeser, G., Huo, D., Tennant, R. W., Jensen, H., Kast, W. M., Krausz, T., & Meredith, S. C. (2004). Strong synergy between mutant ras and HPV16 E6/E7 in the development of primary tumors. *Oncogene, 23*(22), 3972-3979.

Seddon, B. M., Maxwell, R. J., Honess, D. J., Grimshaw, R., Raynaud, F., Tozer, G. M., & Workman, P. (2002). Validation of the fluorinated 2-nitroimidazole SR-4554 as a noninvasive hypoxia marker detected by magnetic resonance spectroscopy. *Clinical Cancer Research, 8*(7), 2323-2335.

Seiwert, T. Y., Zuo, Z., Keck, M. K., Khattri, A., Pedamallu, C. S., Stricker, T., Brown, C., Pugh, T. J., Stojanov, P., & Cho, J. (2015). Integrative and comparative genomic analysis of HPV-positive and HPV-negative head and neck squamous cell carcinomas. *Clinical Cancer Research, 21*(3), 632-641.

Shi, R., Radulovich, N., Ng, C., Liu, N., Notsuda, H., Cabanero, M., Martins-Filho, S. N., Raghavan, V., Li, Q., & Mer, A. S. (2020). Organoid Cultures as Preclinical Models of Non–Small Cell Lung CancerNon–Small Cell Lung Cancer Organoids. *Clinical Cancer Research, 26*(5), 1162-1174.

Simoes-Sousa, S., Granja, S., Pinheiro, C., Fernandes, D., Longatto-Filho, A., Laus, A. C., Alves, C. D. C., Suárez-Peñaranda, J. M., Pérez-Sayáns, M., & Lopes Carvalho, A. (2016). Prognostic significance of monocarboxylate transporter expression in oral cavity tumors. *Cell Cycle, 15*(14), 1865-1873.

Singh, S., Rao, A., Mishra, P., Yadav, A. K., Maurya, R., Kaur, S., & Tandon, G. (2018). Bioinformatics in Next-Generation Genome Sequencing. In G. Wadhwa, P. Shanmughavel, A. K. Singh & J. R. Bellare (Eds.), *Current trends in Bioinformatics: An Insight* (pp. 27-38). Springer Singapore. 10.1007/978-981-10-7483-7_2

Singleton, D. C., Macann, A., & Wilson, W. R. (2021). Therapeutic targeting of the hypoxic tumour microenvironment. *Nature Reviews Clinical Oncology, 18*(12), 751-772.

Smith, L. P., & Thomas, G. R. (2006). Animal models for the study of squamous cell carcinoma of the upper aerodigestive tract: A historical perspective with review of their utility and limitations. Part A. Chemically-induced de novo cancer, syngeneic animal models of HNSCC, animal models of transplanted xenogeneic human tumors. *International Journal of Cancer, 118*(9), 2111-2122.

Song, W., Tang, Z., Shen, N., Yu, H., Jia, Y., Zhang, D., Jiang, J., He, C., Tian, H., & Chen, X. (2016). Combining disulfiram and poly (l-glutamic acid)-cisplatin conjugates for combating cisplatin resistance. *Journal of Controlled Release, 231*, 94-102.

Sonveaux, P., Végran, F., Schroeder, T., Wergin, M. C., Verrax, J., Rabbani, Z. N., De Saedeleer, C. J., Kennedy, K. M., Diepart, C., & Jordan, B. F. (2008). Targeting lactate-fueled respiration selectively kills hypoxic tumor cells in mice. *The Journal of Clinical Investigation, 118*(12), 3930-3942.

Souvatzoglou, M., Grosu, A. L., Röper, B., Krause, B. J., Beck, R., Reischl, G., Picchio, M., Machulla, H., Wester, H., & Piert, M. (2007). Tumour hypoxia imaging with [18F] FAZA PET in head and neck cancer patients: a pilot study. *European Journal of Nuclear Medicine and Molecular Imaging, 34*(10), 1566-1575.

Spiegelberg, L., Houben, R., Niemans, R., de Ruysscher, D., Yaromina, A., Theys, J., Guise, C. P., Smaill, J. B., Patterson, A. V., Lambin, P., & Dubois, L. J. (2019). Hypoxia-activated prodrugs and (lack of) clinical progress: The need for hypoxia-based biomarker patient selection in phase III clinical trials. *Clinical and Translational Radiation Oncology, 15*, 62-69. https://doi.org/10.1016/j.ctro.2019.01.005

Stegeman, H., Span, P. N., Cockx, S. C., Peters, J. P. W., Rijken, P. F. J. W., van der Kogel, A. J., Kaanders, J. H. A. M., & Bussink, J. (2013). EGFR-Inhibition Enhances Apoptosis in Irradiated Human Head and Neck Xenograft Tumors Independent of Effects on DNA Repair. *Radiation Research, 180*(4), 414-421. 10.1667/RR3349.2

Stratford, I. J., Adams, G. E., Godden, J., Nolan, J., Howells, N., & Timpson, N. (1988). Potentiation of the anti-tumour effect of melphalan by the vasoactive agent, hydralazine. *British Journal of Cancer, 58*(2), 122-127.

Sun, L., Wang, H., Wang, Z., He, S., Chen, S., Liao, D., Wang, L., Yan, J., Liu, W., & Lei, X. (2012). Mixed lineage kinase domain-like protein mediates necrosis signaling downstream of RIP3 kinase. *Cell, 148*(1-2), 213-227.

Swartz, J. E., Smits, H. J., Philippens, M. E., de Bree, R., Kaanders, J. H., & Willems, S. M. (2022). Correlation and colocalization of HIF-1α and pimonidazole staining for hypoxia in laryngeal squamous cell carcinomas: A digital, single-cell-based analysis. *Oral Oncology, 128*, 105862.

Takada, K., Aizawa, Y., Sano, D., Okuda, R., Sekine, K., Ueno, Y., Yamanaka, S., Aoyama, J., Sato, K., & Kuwahara, T. (2021). Establishment of PDX-derived salivary adenoid cystic carcinoma cell lines using organoid culture method. *International Journal of Cancer, 148*(1), 193-202.

Tamura, R., Yoshihara, K., Saito, T., Ishimura, R., Martínez-Ledesma, J. E., Xin, H., Ishiguro, T., Mori, Y., Yamawaki, K., & Suda, K. (2018). Novel therapeutic strategy for cervical cancer harboring FGFR3-TACC3 fusions. *Oncogenesis, 7*(1), 1-12.

Tanaka, N., Osman, A. A., Takahashi, Y., Lindemann, A., Patel, A. A., Zhao, M., Takahashi, H., & Myers, J. N. (2018). Head and neck cancer organoids established by modification of the CTOS method can be used to predict in vivo drug sensitivity. *Oral Oncology, 87*, 49-57.

Tang, C., Chan, C., Jiang, W., Murphy, J. D., Von Eyben, R., Colevas, A. D., Pinto, H., Lee–Enriquez, N., Kong, C., & Le, Q. (2015). Concurrent cetuximab versus platinum-based chemoradiation for the definitive treatment of locoregionally advanced head and neck cancer. *Head & Neck, 37*(3), 386-392.

Tap, W. D., Papai, Z., Van Tine, B. A., Attia, S., Ganjoo, K. N., Jones, R. L., Schuetze, S., Reed, D., Chawla, S. P., & Riedel, R. F. (2017). Doxorubicin plus evofosfamide versus doxorubicin alone in locally advanced, unresectable or metastatic soft-tissue sarcoma (TH CR-406/SARC021): an international, multicentre, open-label, randomised phase 3 trial. *The Lancet Oncology, 18*(8), 1089-1103.

Teicher, B. A., Holden, S. A., Al-Achi, A., & Herman, T. S. (1990). Classification of antineoplastic treatments by their differential toxicity toward putative oxygenated and hypoxic tumor subpopulations in vivo in the FSaIIC murine fibrosarcoma. *Cancer Research, 50*(11), 3339-3344.

Teicher, B. A., Lazo, J. S., & Sartorelli, A. C. (1981). Classification of antineoplastic agents by their selective toxicities toward oxygenated and hypoxic tumor cells. *Cancer Research, 41*(1), 73-81.

Thomas, G. R., & Shnayder, Y. (2010). Genomic Evaluation of Head and Neck Cancer. *Essentials of Genomic and Personalized Medicine* (pp. 511-521). Elsevier.

Tinhofer, I., Braunholz, D., & Klinghammer, K. (2020). Preclinical models of head and neck squamous cell carcinoma for a basic understanding of cancer biology and its translation into efficient therapies. *Cancers of the Head & Neck, 5*(1), 1-10.

Toustrup, K., Sørensen, B. S., Alsner, J., & Overgaard, J. (2012). Hypoxia gene expression signatures as prognostic and predictive markers in head and neck radiotherapy. Paper presented at the *Seminars in Radiation Oncology, , 22*(2) 119-127.

Toustrup, K., Sørensen, B. S., Metwally, M. A. H., Tramm, T., Mortensen, L. S., Overgaard, J., & Alsner, J. (2016). Validation of a 15-gene hypoxia classifier in head and neck cancer for prospective use in clinical trials. *Acta Oncologica, 55*(9-10), 1091-1098.

Toustrup, K., Sørensen, B. S., Nordsmark, M., Busk, M., Wiuf, C., Alsner, J., & Overgaard, J. (2011). Development of a hypoxia gene expression classifier with predictive impact for hypoxic modification of radiotherapy in head and neck cancer. *Cancer Research, 71*(17), 5923-5931.

Urbischek, M., Rannikmae, H., Foets, T., Ravn, K., Hyvönen, M., & de la Roche, M. (2019). Organoid culture media formulated with growth factors of defined cellular activity. *Scientific Reports, 9*(1), 6193. 10.1038/s41598-019-42604-0

Van Cutsem, E., Lenz, H., Furuse, J., Tabernero, J., Heinemann, V., Ioka, T., Bazin, I., Ueno, M., Csõszi, T., Wasan, H., Melichar, B., Karasek, P., Macarulla, T. M., Guillen, C., Kalinka-Warzocha, E., Horvath, Z., Prenen, H., Schlichting, M., Ibrahim, A., & Bendell, J. C. (2016). MAESTRO: A randomized, double-blind phase III study of evofosfamide (Evo) in combination with gemcitabine (Gem) in previously untreated patients (pts) with metastatic or locally advanced unresectable pancreatic ductal adenocarcinoma (PDAC). *Jco, 34*(15), 4007. https://10.1200/JCO.2016.34.15_suppl.4007

VanDussen, K. L., Sonnek, N. M., & Stappenbeck, T. S. (2019). L-WRN conditioned medium for gastrointestinal epithelial stem cell culture shows replicable batch-to-batch activity levels across multiple research teams. *Stem Cell Research, 37*, 101430.

van de Schootbrugge, C., Schults, E. M., Bussink, J., Span, P. N., Grénman, R., Pruijn, G. J., Kaanders, J. H., & Boelens, W. C. (2014). Effect of hypoxia on the expression of αB-crystallin in head and neck squamous cell carcinoma. *BMC Cancer, 14*(1), 1-9.

Varzideh, F., Pahlavan, S., Ansari, H., Halvaei, M., Kostin, S., Feiz, M., Latifi, H., Aghdami, N., Braun, T., & Baharvand, H. (2019). Human cardiomyocytes undergo enhanced maturation in embryonic stem cell-derived organoid transplants. *Biomaterials, 192*, 537-550.

Veeman, M. T., Slusarski, D. C., Kaykas, A., Louie, S. H., & Moon, R. T. (2003). Zebrafish prickle, a modulator of noncanonical Wnt/Fz signaling, regulates gastrulation movements. *Current biology*, *13*(8), 680-685.

Vlachogiannis, G., Hedayat, S., Vatsiou, A., Jamin, Y., Fernández-Mateos, J., Khan, K., Lampis, A., Eason, K., Huntingford, I., & Burke, R. (2018). Patient-derived organoids model treatment response of metastatic gastrointestinal cancers. *Science, 359*(6378), 920-926.

Volpe, D. A., Tomaszewski, J. E., Parchment, R. E., Garg, A., Flora, K. P., Murphy, M. J., & Grieshaber, C. K. (1996). Myelotoxic effects of the bifunctional alkylating agent bizelesin on human, canine and murine myeloid progenitor cells. *Cancer Chemotherapy and Pharmacology, 39*(1), 143-149.

Voltzke, K. J., Lee, Y. A., Zhang, Z., Zevallos, J. P., Yu, G., Winn, D. M., Vaughan, T. L., Sturgis, E. M., Smith, E., & Schwartz, S. M. (2018). Racial differences in the relationship between tobacco, alcohol, and the risk of head and neck cancer: pooled analysis of US studies in the INHANCE Consortium. *Cancer Causes & Control, 29*(7), 619-630.

Voskoglou-Nomikos, T., Pater, J. L., & Seymour, L. (2003). Clinical predictive value of the in vitro cell line, human xenograft, and mouse allograft preclinical cancer models. *Clinical Cancer Research, 9*(11), 4227-4239.

Wang, H., Jiang, H., Van De Gucht, M., & De Ridder, M. (2019). Hypoxic radioresistance: can ROS be the key to overcome it? *Cancers, 11*(1), 112.

Wang, R., Mao, Y., Wang, W., Zhou, X., Wang, W., Gao, S., Li, J., Wen, L., Fu, W., & Tang, F. (2022). Systematic evaluation of colorectal cancer organoid system by single-cell RNA-Seq analysis. *Genome Biology, 23*(1), 1-22.

Watson, M. J., Vignali, P. D., Mullett, S. J., Overacre-Delgoffe, A. E., Peralta, R. M., Grebinoski, S., Menk, A. V., Rittenhouse, N. L., DePeaux, K., & Whetstone, R. D. (2021). Metabolic support of tumour-infiltrating regulatory T cells by lactic acid. *Nature, 591*(7851), 645-651.

Weeber, F., van de Wetering, M., Hoogstraat, M., Dijkstra, K. K., Krijgsman, O., Kuilman, T., Gadellaa-van Hooijdonk, C. G., van der Velden, Daphne L, Peeper, D. S., & Cuppen, E. P. (2015). Preserved genetic diversity in organoids cultured from biopsies of human colorectal cancer metastases. *Proceedings of the National Academy of Sciences, 112*(43), 13308-13311.

Weidner, C., Steinfath, M., Opitz, E., Oelgeschläger, M., & Schönfelder, G. (2016). Defining the optimal animal model for translational research using gene set enrichment analysis. *EMBO Molecular Medicine, 8*(8), 831-838.

Weiss, G. J., Infante, J. R., Chiorean, E. G., Borad, M. J., Bendell, J. C., Molina, J. R., Tibes, R., Ramanathan, R. K., Lewandowski, K., & Jones, S. F. (2011). Phase 1 study of the safety, tolerability, and pharmacokinetics of TH-302, a hypoxia-activated prodrug, in patients with advanced solid malignancies. *Clinical Cancer Research, 17*(9), 2997-3004.

Westbury, C. B., Pearson, A., Nerurkar, A., Reis-Filho, J. S., Steele, D., Peckitt, C., Sharp, G., & Yarnold, J. R. (2007). Hypoxia can be detected in irradiated normal human tissue: a study using the hypoxic marker pimonidazole hydrochloride. *The British Journal of Radiology, 80*(959), 934-938.

Whyard, T., Liu, J., Darras, F. S., Waltzer, W. C., & Romanov, V. (2020). Organoid model of urothelial cancer: Establishment and applications for bladder cancer research. *BioTechniques, 69*(3), 193-199.

Wike-Hooley, J. L., Haveman, J., & Reinhold, H. S. (1984). The relevance of tumour pH to the treatment of malignant disease. *Radiotherapy and Oncology, 2*(4), 343-366.

Williams, K. J., Telfer, B. A., Shannon, A. M., Babur, M., Stratford, I. J., & Wedge, S. R. (2007). Combining radiotherapy with AZD2171, a potent inhibitor of vascular endothelial growth factor signaling: pathophysiologic effects and therapeutic benefit. *Molecular Cancer Therapeutics, 6*(2), 599-606.

Wilson, R. L., Hewes, S. A., Rajan, A., Lin, S., Bomidi, C., Iida, T., Estes, M. K., Maresso, A. W., & Grande-Allen, K. J. (2021). A Millifluidic Perfusion Cassette for Studying the Pathogenesis of Enteric Infections Using Ex-Vivo Organoids. *Annals of Biomedical Engineering, 49*(4), 1233-1244.

Winter, S. C., Buffa, F. M., Silva, P., Miller, C., Valentine, H. R., Turley, H., Shah, K. A., Cox, G. J., Corbridge, R. J., & Homer, J. J. (2007). Relation of a hypoxia metagene derived from head and neck cancer to prognosis of multiple cancers. *Cancer Research, 67*(7), 3441-3449.

Xie, B., & Wu, A. (2016). Organoid culture of isolated cells from patient-derived tissues with colorectal cancer. *Chinese Medical Journal, 129*(20), 2469-2475.

Yamasaki, J., Hirata, Y., Otsuki, Y., Suina, K., Saito, Y., Masuda, K., Okazaki, S., Ishimoto, T., Saya, H., & Nagano, O. (2022). MEK inhibition suppresses metastatic progression of KRAS-mutated gastric cancer. *Cancer Science, 113*(3), 916.

Yan, H. H., Siu, H. C., Law, S., Ho, S. L., Yue, S. S., Tsui, W. Y., Chan, D., Chan, A. S., Ma, S., & Lam, K. O. (2018). A comprehensive human gastric cancer organoid biobank captures tumor subtype heterogeneity and enables therapeutic screening. *Cell Stem Cell, 23*(6), 882-897.

Yoon, C., Kim, D., Lim, J. H., & Lee, G. M. (2020). Forskolin Increases cAMP Levels and Enhances Recombinant Antibody Production in CHO Cell Cultures. *Biotechnology Journal*, *15*(10), 2000264. https://doi.org/10.1002/biot.202000264

Yoshida, G. J. (2020). Applications of patient-derived tumor xenograft models and tumor organoids. *Journal of Hematology & Oncology, 13*(1), 1-16.

Yu, L., Yao, Y., Wang, Y., Zhou, S., Lai, Q., Lu, Y., Liu, Y., Zhang, R., Wang, R., & Liu, C. (2018). Preparation and anti-cancer evaluation of promiximab-MMAE, an anti-CD56 antibody drug conjugate, in small cell lung cancer cell line xenograft models. *Journal of Drug Targeting, 26*(10), 905-912.

Zandberg, D. P., Menk, A. V., Velez, M., Normolle, D., DePeaux, K., Liu, A., Ferris, R. L., & Delgoffe, G. M. (2021). Tumor hypoxia is associated with resistance to PD-1 blockade in squamous cell carcinoma of the head and neck. *Journal for Immunotherapy of Cancer, 9*(5)

Zegers, C. M., Hoebers, F. J., van Elmpt, W., Bons, J. A., Öllers, M. C., Troost, E. G., Eekers, D., Balmaekers, L., Arts-Pechtold, M., & Mottaghy, F. M. (2016). Evaluation of tumour hypoxia during radiotherapy using [18F] HX4 PET imaging and blood biomarkers in patients with head and neck cancer. *European Journal of Nuclear Medicine and Molecular Imaging, 43*(12), 2139-2146.

Zegers, C. M., Van Elmpt, W., Hoebers, F. J., Troost, E. G., Öllers, M. C., Mottaghy, F. M., & Lambin, P. (2015). Imaging of tumour hypoxia and metabolism in patients with head and neck squamous cell carcinoma. *Acta Oncologica, 54*(9), 1378-1384.

Zegers, C. M., van Elmpt, W., Szardenings, K., Kolb, H., Waxman, A., Subramaniam, R. M., Moon, D. H., Brunetti, J. C., Srinivas, S. M., & Lambin, P. (2015). Repeatability of hypoxia PET imaging using [18F] HX4 in lung and head and neck cancer patients: a prospective multicenter trial. *European Journal of Nuclear Medicine and Molecular Imaging, 42*(12), 1840-1849.

Zhang, J., Cheng, Q., Zhou, Y., Wang, Y., & Chen, X. (2013). Slug is a key mediator of hypoxia induced cadherin switch in HNSCC: correlations with poor prognosis. *Oral Oncology*, *49*(11), 1043-1050.

Zhang, L., Yang, N., Garcia, J. C., Mohamed, A., Benencia, F., Rubin, S. C., Allman, D., & Coukos, G. (2002). Generation of a syngeneic mouse model to study the effects of vascular endothelial growth factor in ovarian carcinoma. *The American Journal of Pathology, 161*(6), 2295-2309.

Zhang, Z., Liu, G., Peng, L., Zhang, C., Jia, Y., Yang, W., & Mao, L. (2018). Effect of PAK1 gene silencing on proliferation and apoptosis in hepatocellular carcinoma cell lines MHCC97-H and HepG2 and cells in xenograft tumor. *Gene Therapy, 25*(4), 284-296.

Zhao, G., Li, W., Chen, D., Henry, J. R., Li, H., Chen, Z., Zia-Ebrahimi, M., Bloem, L., Zhai, Y., & Huss, K. (2011). A Novel, Selective Inhibitor of Fibroblast Growth Factor Receptors That Shows a Potent Broad Spectrum of Antitumor Activity in Several Tumor Xenograft ModelsSmall-Molecule Inhibitor of FGFR. *Molecular Cancer Therapeutics, 10*(11), 2200-2210.

Zhao, W., He, X., Hoadley, K. A., Parker, J. S., Hayes, D. N., & Perou, C. M. (2014). Comparison of RNA-Seq by poly (A) capture, ribosomal RNA depletion, and DNA microarray for expression profiling. *BMC Genomics, 15*(1), 1-11.

Zheng, B., Ko, K. P., Fang, X., Wang, X., Zhang, J., Jun, S., ... & Park, J. I. (2021). A new murine esophageal organoid culture method and organoid-based model of esophageal squamous cell neoplasia. *Iscience*, *24*(12), 103440.